Michael Buchner, BSc

Simulation of Carrier Transport in Pentacene Thin Film Transistors with Finite Element Methods

MASTER THESIS

For obtaining the academic degree

Diplom-Ingenieur

Master Programm of
Technical Physics

Graz University of Technology

Supervisor:
Ao.Univ.-Prof. Dipl.-Ing. Dr.techn. Ferdinand Schürrer

Co-Supervisor:
Dipl.-Phys. Dr.techn. Karin Zojer

Institute of Theoretical and Computational Physics

Graz, June 2012

Deutsche Fassung:
Beschluss der Curricula-Kommission für Bachelor-, Master- und Diplomstudien vom 10.11.2008
Genehmigung des Senates am 1.12.2008

EIDESSTATTLICHE ERKLÄRUNG

Ich erkläre an Eides statt, dass ich die vorliegende Arbeit selbstständig verfasst, andere als die angegebenen Quellen/Hilfsmittel nicht benutzt, und die den benutzten Quellen wörtlich und inhaltlich entnommenen Stellen als solche kenntlich gemacht habe.

Graz, am …… ……
(Unterschrift)

Englische Fassung:

STATUTORY DECLARATION

I declare that I have authored this thesis independently, that I have not used other than the declared sources / resources, and that I have explicitly marked all material which has been quoted either literally or by content from the used sources.

…… ……
date (signature)

Abstract

The diploma thesis deals with a two dimensional simulation of the carrier transport in thin film transistors made of pentacene. The simulation solves, based on a finite element method, the drift diffusion equations for holes and ions self consistently with the Poisson equation. With this modelling it is possible to calculate the I-V (current-voltage) characteristics of pentacene thin film transistors by considering an additional space charge layer at the front of the gate interface. The different effects of a layer with a positive or a negative charge carrier density is simulated. Especially the underlying effects of a ion drift and neutralization are studied. Also the influence of an NH_3 gas on the device is analyzed.

Zusammenfassung

Diese Diplomarbeit befasst sich mit zweidimensionalen Simulationen von organischen Dünnschichttransistoren aus Pentacen. In den Simulationen werden Drift- Diffusionsgleichungen für Löcher und Ionen selbstkonsistent mit der Poissongleichung gelöst. Mit Hilfe dieses Modells ist es möglich, I-V (Strom-Spannung) Kennlinien von Dünnschichttransistoren aus Pentacen, mit zusätzlicher Flächenladungsschicht am Gatekontakt, zu simulieren. Die unterschiedlichen Effekte einer positiv bzw. negativ geladener Ladungsschicht werden simuliert. Insbesonders wurden die Effekte des Ionendrifts und der Ionenneutralisation untersucht. Es wurde außerdem der Einfluss von NH_3 auf die erwähnten Transistoren analysiert.

Table of Contents

List of Figures

List of Tables

1 Introduction

The field-effect transistor (FET), is the basic component in modern electronics. Today's micro-chips are using hundreds of millions of such transistors. Many everyday devices such as laptop, mobile phone or digital camera last unthinkable without these components. Even in modern sensors, field-effect transistors are important nowadays. Using a variety of such FETs can detect different gases and their concentrations can be measured. Field-effect transistors which are sensitive to different gases can be combined in one chip, which makes it possible to fulfill in a small space with only one device many different tasks.

It make any difference, whether FETs measure the methane gas for early detection of broken gas lines, or operate as a component in intelligent clothes, both have one in common: they should be simple and inexpensive for manufacturing. These properties are to be expected by the so-called organic thin-film transistors (OTFTs). Unlike traditional transistors, the active layer is not composed of a semiconductor material such as silicon or germanium, it is made of a polymer. This can, for example, be achieved by vapor deposition or spin coating to a support structure, which enables easy and cost-efficient production. Because of the manufacturing process, it is also easy to install intermediate layers, which change the properties of the OTFTs fundamentally. This makes it possible to produce OTFTs optimized for a specific task. As active layer, pentacene is often used in such OTFTs. For a better understanding of the internal processes of such OTFTs a lot of research has been already done. For example, the use of the MOSFET theory was proven by Alam et al. [1]. General top-contact pentacene thin film transistors were simulated in [2]. The behavior of charge carriers in OTFTs was studied by Demeyu et al. [3]. Especially for pentacene-based OTFTs, modifications of the drift-diffusion equations were investigated [4]. Diffusion processes at the surface of pentacene were studied [5]. Fast and stable simulation methods for the special OTFTs geometry were presented by Yiming Li [6]. Pentacene-based OTFTs show a hysteresis. This effect were studied by Ucurum et al. [7]. There exist also modifications of pentacene as active material such as tris-isopropylsilylethynyl (TIPS)-pentacene. The resulting device characteristics were studied by Gupta et al. [8]. The dependence of the thickness of OTFTs was simulated by Gupta et al. [9]. This is only a small excerpt from the existing work on organic semiconductors that exist.

The aim of this thesis is to examine theoretically the effect of a special interface layer consisting of a mixture of two trichlorosilanes, namely 4-(2-(trichlorosilyl)ethyl)benzene-1-sulfonyl chloride (T-SC, 70 %) and a sulfonic acid derivate 4-(2-(trichlorosilyl)ethyl)benzenesulfonic acid (T-SA, 30 %). Through this

layer, the OTFT characteristics exhibit a shift of the threshold voltage by several ten volts. As active material in the OTFT pentacene is adopted. The effects of building a space charge layer are modeled and their influence on the shape of the I-V characteristic is studied in detail. The effects which appear by exposing the devices to ammonia (NH3) gas are also simulated. The time development of the spread of ions from the interface layer and the exposing of the devices with ammonia is studied in order to gain a better understanding of the various processes. By varying the input parameters, the current-voltage characteristics are simulated. Due to the time-resolved simulation, information about the electric field and the particle densities in the device are available. The simulations in combination with the existing measurements can be used to estimate the speed of the various processes that take place in the device. Furthermore, it is also possible to estimate the ion concentration in the space charge layer. This is done by solving the continuity equations and the Poisson equation selfconsistently. The devise geometry is discretized on a two-dimensional mesh under periodic and Dirichlet boundary conditions. The differential equations are solved with the finite element approach.

The thesis consists of six main chapters. We start by introducing the basic properties about organic thin-film transistors. The second chapter is devoted to the theoretical aspects relevant for modeling the device. Chapter three gives a brief insight into the fundamentals of the finite element method. The fourth chapter verifies with the help of a simple model of a FET, the accuracy and stability of the finite element simulations. Then, the available measurements are shown briefly. Finally, simulation results are presented and discussed in detail.

2 Pentacene based Organic Thin-Film Transistors

This chapter provides a brief overview of the basics of a field-effect transistor. For more detailed information the reader is referred to the bibliography.

A field effect transistor (FET) is a voltage-controlled switching element. It usually consists of three contacts, source drain and gate. The current flow in the semiconducting layer between source and drain is controlled by the electric field caused by the gate electrode. This active layer is separated from the gate by an insulating layer as shown in Fig. 5.2.

This structure is very similar to a plate capacitor. Source and drain form a plate and the gate the other one. In the off state, source and gate are at the same electric potential. Even if source and drain are at different potentials, only a few charge carriers are located in the active layer. The current flow is negligible. By applying a voltage between source and gate, an electric field between the plates is created. Charge carriers (electrons or holes, depending on the material) are pushed into the active layer. This forms a channel at the interface between insulator and active material, which compensate the electric field. Due to the high density of charge carriers in the channel, the flow of current between source and drain increases. The achievable output currents depend inter alia on the mobility of charge carriers. The higher the mobility, the larger the resulting current flow. The maximum switching frequency from the transistor also depends on the mobility. In conventional field effect transistors the active material often consists of crystalline silicon. The reason is that with silicon high mobility rates can be achieved.

The production of such FET's is very complicated and expensive. For many applications, organic materials, which are cheapen to be produced, offer an interesting alternative.

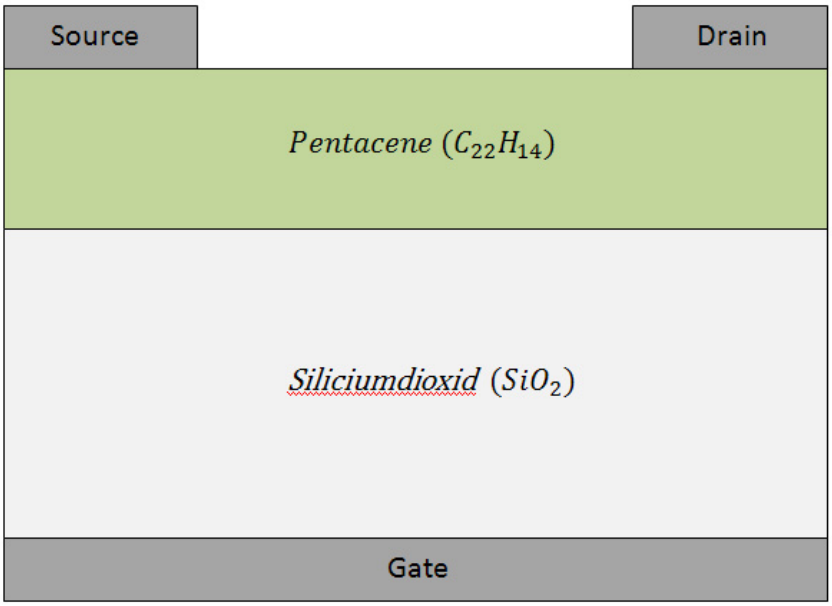

Fig. 2.1: Schematic structure of a field-effect transistors.

2.1 Organic Thin-Film Transistors

Organic materials offer many advantages. They can be flexible or transparent. Moreover, their production is much less challenging and affordable. Such a material is, e.g., pentacene. In a pentacene FET the hole conduction plays a major role. Therefore, the device is a so-called p-channel transistor. The mobility of holes in pentacene FETs can vary greatly depending on the manufacturing process. The mobility in pentacene transistors is normally in the range of 10^{-3} $\mathrm{cm^2V^{-1}s^{-1}}$ to 10^{-2} $\mathrm{cm^2V^{-1}s^{-1}}$. Using special methods, the mobility in pentacene has been increased up to 58 $\mathrm{cm^2V^{-1}s^{-1}}$ [10] in the last few years. Normal silicon transistors usually have in all three spatial directions similar dimensions in the nm range. In contrast, pentacene transistors usually have very different dimensions. The characteristic channel length (distance between source and drain) can be up to 100 μm, whereas the source-drain distance can be just a few nm. Such a transistor can be thought as a thin film. Because of these properties of organic transistors, there are special demands on the device modeling and the simulation methods. For treating the band structure in silicon based FETs a common simulation model used is the Boltzmann transport equation. Since the molecular structure of OTFTs is highly complex it is not possible to determine the necessary microscopic simulation parameters. For this reason, it seems reasonable to use a simulation model which does not depend directly on these parameters. In the subsequent chapter, a suitable device model derived from the Boltzmann equation, is presented.

3 Device Model

This chapter deals with necessary equations for the simulation of the charge carrier transport in organic semiconductors. For the simulation we need the drift-diffusion equations for electrons and holes and the Poisson equation. The Poisson equation determines the electrical potential due to the charge distribution and the external applied voltages. The drift-diffusion equation and the Poisson equation are coupled by the charge distribution and the electric field strength. Processes in which particle species transform into each other are described by rate equations. The distribution of non-charged particles can be described by the diffusion equation. This chapter gives a brief introduction to the necessary equations and shows how these equations are obtained. It consists of five sections. The first section describes the derivation of the carrier continuity equation. In the second section the drift-diffusion current equation and the diffusion equation are derived. In the third section the recombination term is described. The fourth section deals with the derivation of the Poisson equation and in the fifth section a short summary of all equations is given. We begin with the carrier continuity equation.

3.1 Carrier Continuity Equation

For describing the motion of all involved particles we could use the Newtonian equations. For a huge amount of particles this seems to be a bad idea. Since it does not matter which of the involved particles have the momentum $\mathbf{p}$ at position $\mathbf{r}$, one could also define a probability density $f(\mathbf{r}, \mathbf{p}, t)$ which describes the probability that a particle with momentum $\mathbf{p}$ at position $\mathbf{r}$ exists at time t. If we neglect quantum mechanical influences we can assume that the particles move on trajectories. Then the probability that a particle exists at position $\mathbf{r}$ with momentum $\mathbf{p}$ at time t is equal to the probability that the particle was at position $\mathbf{r}'$ with momentum $\mathbf{p}'$ at time $t - dt$. The position $\mathbf{r}'$ is expressed by

$$\mathbf{r}' = \mathbf{r} - d\mathbf{r} = \mathbf{r} - \frac{d\mathbf{r}}{dt}\, dt = \mathbf{r} - \dot{\mathbf{r}}\, dt, \tag{3.1}$$

while the momentum $\mathbf{p}'$ is given by

$$\mathbf{p}' = \mathbf{p} - d\mathbf{p} = \mathbf{p} - \frac{d\mathbf{p}}{dt}\, dt = \mathbf{p} - \dot{\mathbf{p}}\, dt. \tag{3.2}$$

Now we can write for the probability density

$$f(\mathbf{r}, \mathbf{p}, t) = f(\mathbf{r} - \dot{\mathbf{r}}\, dt, \mathbf{p} - \dot{\mathbf{p}}\, dt, t - dt). \tag{3.3}$$

As next step, we expand $f(\mathbf{r}-\dot{\mathbf{r}}\ dt, \mathbf{p}-\dot{\mathbf{p}}\ dt, t-dt)$ in a Taylor series in powers of dt around the position $\mathbf{r}$, the momentum $\mathbf{p}$ and time t. Additionally, we make the assumption that we can truncate the Taylor series after the first-order term and obtain

$$f(\mathbf{r},\mathbf{p},t) = f(\mathbf{r},\mathbf{p},t) + \dot{\mathbf{r}} \cdot \frac{\partial f(\mathbf{r},\mathbf{p},t)}{\partial \mathbf{r}} dt + \dot{\mathbf{p}} \cdot \frac{\partial f(\mathbf{r},\mathbf{p},t)}{\partial \mathbf{k}} dt + \frac{\partial f(\mathbf{r},\mathbf{p},t)}{\partial t} dt, \tag{3.4}$$

or by rearranging the terms

$$\frac{\partial f(\mathbf{r},\mathbf{p},t)}{\partial t} + \dot{\mathbf{r}} \cdot \frac{\partial f(\mathbf{r},\mathbf{p},t)}{\partial \mathbf{r}} + \dot{\mathbf{p}} \cdot \frac{\partial f(\mathbf{r},\mathbf{p},t)}{\partial \mathbf{p}} = 0. \tag{3.5}$$

If we follow a particle along its trajectory, Eq. (3.5) predicts that the occupation probability does not change. This is accurately the case if we do not have a source or sink that can generate or destroy particles and if we neglect the possibility of particle scattering. To include this effects we have to extend Eq. (3.5) to

$$\frac{\partial f(\mathbf{r},\mathbf{p},t)}{\partial t} + \dot{\mathbf{r}} \cdot \frac{\partial f(\mathbf{r},\mathbf{p},t)}{\partial \mathbf{r}} + \dot{\mathbf{p}} \cdot \frac{\partial f(\mathbf{r},\mathbf{p},t)}{\partial \mathbf{p}} = \left.\frac{\partial f(\mathbf{r},\mathbf{p},t)}{\partial t}\right|_{col} + G(\mathbf{r},\mathbf{p},t). \tag{3.6}$$

In Eq. (3.6) the particle scattering is included by a collision term $\left.\frac{\partial f(\mathbf{r},\mathbf{p},t)}{\partial t}\right|_{col}$, the influence of a source or sink is considered by $G(\mathbf{r},\mathbf{p},t)$. The equation (3.6) is named Boltzmann equation [11][12]. In this thesis we consider charged particles in a solid. The assumption that charged particles like electrons can move freely in the solid leads to the "free electron model"[13]. We further assume that the relation between the kinetic energy of a particle and the wave vector $\mathbf{k}$ is given by

$$W(\mathbf{k}) = \frac{\hbar^2 \mathbf{k}^2}{2m}. \tag{3.7}$$

In Eq. (3.7) $\hbar$ is the reduced Planck constant and m denotes the effective mass of the particle. The kinetic energy W_{kin} of a particle could also be expressed by the momentum $\mathbf{p}$ of the particle:

$$W(\mathbf{p}) = \frac{\mathbf{p}^2}{2m} \tag{3.8}$$

based on the relation

$$\mathbf{p} = \hbar \mathbf{k}. \tag{3.9}$$

Now we can transform Eq. (3.6) into a more common form:

$$\frac{\partial f(\mathbf{r},\mathbf{k},t)}{\partial t} + \dot{\mathbf{r}} \cdot \frac{\partial f(\mathbf{r},\mathbf{k},t)}{\partial \mathbf{r}} + \dot{\mathbf{k}} \cdot \frac{\partial f(\mathbf{r},\mathbf{k},t)}{\partial \mathbf{k}} = \left.\frac{\partial f(\mathbf{r},\mathbf{k},t)}{\partial t}\right|_{col} + G(\mathbf{r},\mathbf{k},t). \tag{3.10}$$

The next step is to define the collision term $\left.\frac{\partial f(\mathbf{r},\mathbf{p},t)}{\partial t}\right|_{col}$. The determination of the collision term of the Bolzmann equation is in general very complicated, for a more detailed

description, the reader is referred to [11]. If one assumes the semiclassical Bolzmann collision operator for fermions, the Fermi-Dirac function

$$f_0(\mathbf{r},\mathbf{k}) = \frac{1}{1+e^{\frac{W_C(\mathbf{r},\mathbf{k})-W_F}{k_B T}}} \tag{3.11}$$

results as the solution in the case of equilibrium. In Eq. (3.11), W_F is the Fermi level, T the temperature, k_B the Boltzmann constant and $W_C(\mathbf{r},\mathbf{k}) = W_0(\mathbf{r}) + W(\mathbf{k})$, the carrier potential $W_0(\mathbf{r})$ plus the kinetic energy $W(\mathbf{k})$.

We split the non-equilibrium probability density function

$$f(\mathbf{r},\mathbf{k},t) = f_S(\mathbf{r},\mathbf{k},t) + f_A(\mathbf{r},\mathbf{k},t), \tag{3.12}$$

in an symmetric part $f_S(\mathbf{r},\mathbf{k},t) = f_S(\mathbf{r},-\mathbf{k},t)$ and an anti-symmetric part $f_A(\mathbf{r},\mathbf{k},t) = -f_A(\mathbf{r},-\mathbf{k},t)$. In a non-equilibrium state we additionally assume that the symmetric density function differs only slightly from a Fermi-Dirac distribution and we can fit it with

$$f_S(\mathbf{r},\mathbf{k},t) = \frac{1}{1+e^{\frac{W_C(\mathbf{r},\mathbf{k})-W_n(t)}{k_B T}}}. \tag{3.13}$$

In Eq. (3.13), the fit parameter $W_n(t)$ is often named quasi Fermi level. Next we have to specify the collision term more precisely:

$$\left.\frac{\partial f(\mathbf{r},\mathbf{k},t)}{\partial t}\right|_{col} = \int \left[S(\mathbf{k}',\mathbf{k}) f(\mathbf{r},\mathbf{k}',t) - S(\mathbf{k},\mathbf{k}') f(\mathbf{r},\mathbf{k},t)\right]\, d^3k' \tag{3.14}$$

In Eq. (3.14) we assumed nondegenerate conditions for the collision term. The function $S(\mathbf{k}',\mathbf{k})$ defines the probability that a particle with wave vector $\mathbf{k}'$ transforms into a particle with wave vector $\mathbf{k}$ during a collision. Inserting this collision term into Eq. (3.10) yields the Boltzmann equation for nondegenerate conditions:

$$\frac{\partial f(\mathbf{r},\mathbf{k},t)}{\partial t} + \dot{\mathbf{r}}\cdot\frac{\partial f(\mathbf{r},\mathbf{k},t)}{\partial \mathbf{r}} + \dot{\mathbf{k}}\cdot\frac{\partial f(\mathbf{r},\mathbf{k},t)}{\partial \mathbf{k}} = \int \left[S(\mathbf{k}',\mathbf{k}) f(\mathbf{r},\mathbf{k}',t) - S(\mathbf{k},\mathbf{k}') f(\mathbf{r},\mathbf{k},t)\right]\, d^3k' + G(\mathbf{r},\mathbf{k},t). \tag{3.15}$$

The Boltzmann equation is far too complicated for a simulation of the carrier transport in organic semiconductors. In organic semiconductors many input parameters of the Boltzmann equation are unknown or not definable. We need macroscopic parameters depending on the microscopic molecular structure. One way to derive a balance equation for macroscopic variables from the very complex Boltzmann equation is the method of moments. For this purpose, the whole equation is multiplied by a wave vector-dependent

function $\xi(\mathbf{k})$. Subsequently, the resulting equation has to be integrated over the whole k-space:

$$\begin{aligned}\int \xi(\mathbf{k})\frac{\partial f(\mathbf{r},\mathbf{k},t)}{\partial t}\,d^3k + \int \xi(\mathbf{k})\dot{\mathbf{r}}\cdot\frac{\partial f(\mathbf{r},\mathbf{k},t)}{\partial \mathbf{r}}\,d^3k + \int \xi(\mathbf{k})\dot{\mathbf{k}}\cdot\frac{\partial f(\mathbf{r},\mathbf{k},t)}{\partial \mathbf{k}}\,d^3k \\ = \int\int \xi(\mathbf{k})S(\mathbf{k}',\mathbf{k})f(\mathbf{r},\mathbf{k}',t)\,d^3k'\,d^3k \\ - \int\int \xi(\mathbf{k})S(\mathbf{k},\mathbf{k}')f(\mathbf{r},\mathbf{k},t)\,d^3k'\,d^3k + \int \xi(\mathbf{k})G(\mathbf{r},\mathbf{k},t)\,d^3k.\end{aligned} \tag{3.16}$$

If we now interchange the dummy variables $\mathbf{k}$ and $\mathbf{k}'$ in the first integral of the right side in Eq. (3.16) we get

$$\begin{aligned}\int \xi(\mathbf{k})\frac{\partial f(\mathbf{r},\mathbf{k},t)}{\partial t}\,d^3k + \int \xi(\mathbf{k})\dot{\mathbf{r}}\cdot\frac{\partial f(\mathbf{r},\mathbf{k},t)}{\partial \mathbf{r}}\,d^3k + \int \xi(\mathbf{k})\dot{\mathbf{k}}\cdot\frac{\partial f(\mathbf{r},\mathbf{k},t)}{\partial \mathbf{k}}\,d^3k \\ = \int\int \xi(\mathbf{k}')S(\mathbf{k},\mathbf{k}')f(\mathbf{r},\mathbf{k},t)\,d^3k\,d^3k' \\ - \int\int \xi(\mathbf{k})S(\mathbf{k},\mathbf{k}')f(\mathbf{r},\mathbf{k},t)\,d^3k'\,d^3k + \int \xi(\mathbf{k})G(\mathbf{r},\mathbf{k},t)\,d^3k.\end{aligned} \tag{3.17}$$

The collision terms can also be written in following form:

$$\begin{aligned}\int \xi(\mathbf{k})\frac{\partial f(\mathbf{r},\mathbf{k},t)}{\partial t}\,d^3k + \int \xi(\mathbf{k})\dot{\mathbf{r}}\cdot\frac{\partial f(\mathbf{r},\mathbf{k},t)}{\partial \mathbf{r}}\,d^3k + \int \xi(\mathbf{k})\dot{\mathbf{k}}\cdot\frac{\partial f(\mathbf{r},\mathbf{k},t)}{\partial \mathbf{k}}\,d^3k \\ = \int \xi(\mathbf{k})f(\mathbf{r},\mathbf{k},t)\int S(\mathbf{k},\mathbf{k}')\left[\frac{\xi(\mathbf{k}')}{\xi(\mathbf{k})}-1\right]\,d^3k'\,d^3k \\ + \int \xi(\mathbf{k})G(\mathbf{r},\mathbf{k},t)\,d^3k.\end{aligned} \tag{3.18}$$

If we choose $\xi(\mathbf{k}) := \mathbf{k}^0 = 1$ we obtain the carrier continuity equation. Integrating the Boltzmann equation (3.18) over the entire k-space yields

$$\begin{aligned}\underbrace{\int \frac{\partial f(\mathbf{r},\mathbf{k},t)}{\partial t}\,d^3k}_{Term\ 1} + \underbrace{\int \dot{\mathbf{r}}\cdot\frac{\partial f(\mathbf{r},\mathbf{k},t)}{\partial \mathbf{r}}\,d^3k}_{Term\ 2} + \underbrace{\int \dot{\mathbf{k}}\cdot\frac{\partial f(\mathbf{r},\mathbf{k},t)}{\partial \mathbf{k}}\,d^3k}_{Term\ 3} \\ = \underbrace{\int G(\mathbf{r},\mathbf{k},t)\,d^3k}_{Term\ 4},\end{aligned} \tag{3.19}$$

since the collision term vanishes. For reasons of clarity, the individual terms are simplified separately. An exchange of integration and differentiation yields

$$\int \frac{\partial f(\mathbf{r},\mathbf{k},t)}{\partial t}\,d^3k = \frac{\partial}{\partial t}\int f(\mathbf{r},\mathbf{k},t)\,d^3k, \tag{3.20}$$

for the first term. To proceed we need the occupied volume of a single state $\triangle V_k$ in the k-space. Out of the "free electron model"[13] we get

$$\triangle V_k = \frac{(2\pi)^3}{V}. \tag{3.21}$$

Now we are able to calculate the total amount of particles

$$N = 2\frac{1}{\triangle V_k}\int f(\mathbf{r},\mathbf{k},t)\; d^3k. \tag{3.22}$$

The factor two in Eq. (3.22) is due to the spin of fermions. If we consider that the particle density is defined by

$$n(\mathbf{r},t) = \frac{1}{V}N = \frac{1}{V}2\frac{V}{(2\pi)^3}\int f(\mathbf{r},\mathbf{k},t)\; d^3k = \frac{1}{4\pi^3}\int f(\mathbf{r},\mathbf{k},t)\; d^3k, \tag{3.23}$$

we get

$$\int \frac{\partial f(\mathbf{r},\mathbf{k},t)}{\partial t}\; d^3k = 4\pi^3\frac{\partial}{\partial t}n(\mathbf{r},t). \tag{3.24}$$

In order to simplify the second term we make use of the fact that the velocity $\dot{\mathbf{r}}$ does not depend on $\mathbf{r}$, which leads to

$$\int \dot{\mathbf{r}}\cdot\frac{\partial f(\mathbf{r},\mathbf{k},t)}{\partial \mathbf{r}}\; d^3k = \frac{\partial}{\partial \mathbf{r}}\cdot\int f(\mathbf{r},\mathbf{k},t)\dot{\mathbf{r}}\; d^3k \tag{3.25}$$

for the second term. To continue we use the definition of the average velocity

$$\overline{\mathbf{v}} = \frac{\int f(\mathbf{r},\mathbf{k},t)\dot{\mathbf{r}}\; d^3k}{\int f(\mathbf{r},\mathbf{k},t)\; d^3k}, \tag{3.26}$$

to simplify the second term. Now we are able to express

$$\int f(\mathbf{r},\mathbf{k},t)\dot{\mathbf{r}}\; d^3k = 4\pi^3 n(\mathbf{r},t)\overline{\mathbf{v}} \tag{3.27}$$

with the carrier concentration $n(\mathbf{r},t)$, Eq. (3.23), and the average velocity $\overline{\mathbf{v}}$. This leads to

$$\int \dot{\mathbf{r}}\cdot\frac{\partial f(\mathbf{r},\mathbf{k},t)}{\partial \mathbf{r}}\; d^3k = 4\pi^3\frac{\partial}{\partial \mathbf{r}}\cdot\left[n(\mathbf{r},t)\overline{\mathbf{v}}\right], \tag{3.28}$$

for the second term. Now we proceed with the third term. Due to the relation

$$\mathbf{F}(\mathbf{r},\mathbf{p},t) = \frac{d\mathbf{p}}{dt} \tag{3.29}$$

the expression $\frac{\partial \mathbf{p}}{\partial t}$ can be interpreted as an acting force $\mathbf{F}(\mathbf{r}, \mathbf{p}, t)$. In combination with Eq. (3.9) we obtain

$$\dot{\mathbf{k}} = \frac{1}{\hbar}\mathbf{F}(\mathbf{r}, \mathbf{k}, t). \tag{3.30}$$

We use Eq. (3.30) in term three, which results in

$$\int \dot{\mathbf{k}} \cdot \frac{\partial f(\mathbf{r}, \mathbf{k}, t)}{\partial \mathbf{k}}\, d^3k = \int \frac{1}{\hbar}\mathbf{F}(\mathbf{r}, \mathbf{k}, t) \cdot \frac{\partial f(\mathbf{r}, \mathbf{k}, t)}{\partial \mathbf{k}}\, d^3k. \tag{3.31}$$

In general, the force depends on the wave vector, therefore, we need the identity [14]:

$$\mathbf{A} \cdot \nabla B = \nabla \cdot (B\mathbf{A}) - B\nabla \mathbf{A} \tag{3.32}$$

and get

$$\begin{aligned}\int \dot{\mathbf{k}} \cdot \frac{\partial f(\mathbf{r}, \mathbf{k}, t)}{\partial \mathbf{k}}\, d^3k =& \frac{1}{\hbar}\int \frac{\partial}{\partial \mathbf{k}} \cdot [f(\mathbf{r}, \mathbf{k}, t)\mathbf{F}(\mathbf{r}, \mathbf{k}, t)]\; d^3k \\ &- \frac{1}{\hbar}\int f(\mathbf{r}, \mathbf{k}, t)\frac{\partial}{\partial \mathbf{k}} \cdot \mathbf{F}(\mathbf{r}, \mathbf{k}, t)\; d^3k.\end{aligned} \tag{3.33}$$

With Gauss' theorem we can transform the first part of Eq. (3.33) into a surface integral. This surface integral vanishes, because $f(\mathbf{r}, \mathbf{k}, t)$ is always finite and vanishes for $|\mathbf{k}| \to \infty$. It follows

$$\int \dot{\mathbf{k}} \cdot \frac{\partial f(\mathbf{r}, \mathbf{k}, t)}{\partial \mathbf{k}}\, d^3k = -\frac{1}{\hbar}\int f(\mathbf{r}, \mathbf{k}, t)\frac{\partial}{\partial \mathbf{k}} \cdot \mathbf{F}(\mathbf{r}, \mathbf{k}, t)\; d^3k. \tag{3.34}$$

To continue we assume that the force $\mathbf{F}(\mathbf{r}, \mathbf{k}, t)$ is given by

$$\mathbf{F}(\mathbf{r}, \mathbf{k}, t) = e\; \mathbf{E}(\mathbf{r}, t). \tag{3.35}$$

In Eq. (3.35), the charge of a particle is denoted by e and $\mathbf{E}(\mathbf{r}, t)$ is the electric field. Taking advantage of Eq. (3.35) yields for term three

$$\int \dot{\mathbf{k}} \cdot \frac{\partial f(\mathbf{r}, \mathbf{k}, t)}{\partial \mathbf{k}}\, d^3k = -\frac{e}{\hbar}\int f(\mathbf{r}, \mathbf{k}, t)\frac{\partial}{\partial \mathbf{k}} \cdot\; \mathbf{E}(\mathbf{r}, t)\; d^3k = 0. \tag{3.36}$$

Last but not least we have to consider term four. The total number of particles generated per unit volume and unit time is given by

$$R(\mathbf{r}, t) = \frac{1}{V}2\frac{V}{(2\pi)^3}\int G(\mathbf{r}, \mathbf{k}, t)\; d^3k = \frac{1}{4\pi^3}\int G(\mathbf{r}, \mathbf{k}, t)\; d^3k. \tag{3.37}$$

From this result we get

$$\int G(\mathbf{r}, \mathbf{k}, t)\; d^3k = 4\pi^3 R(\mathbf{r}, t). \tag{3.38}$$

If we put the terms Eq. (3.24), Eq. (3.28), Eq. (3.36) and Eq. (3.38) together, we obtain

$$\frac{\partial}{\partial t} n(\mathbf{r},t) + \frac{\partial}{\partial \mathbf{r}} \cdot [\overline{\mathbf{v}} n(\mathbf{r},t)] = R(\mathbf{r},t). \tag{3.39}$$

The expression $\overline{\mathbf{v}} n(\mathbf{r},t)$ defines the particle flow so that the current is given by

$$\mathbf{J}(\mathbf{r},t) = e\, \overline{\mathbf{v}} n(\mathbf{r},t), \tag{3.40}$$

where the charge of a particle is denoted by e. For electrons the charge $e = -q = -1.602176 \cdot 10^{-19} C$, for holes the charge $e = q$. Inserting Eq. (3.40) into Eq. (3.39) yields the carrier continuity equation:

$$\frac{\partial}{\partial t} n(\mathbf{r},t) + \frac{1}{e} \frac{\partial}{\partial \mathbf{r}} \cdot \mathbf{J}(\mathbf{r},t) = R(\mathbf{r},t). \tag{3.41}$$

This equation has three unknown functions $R(\mathbf{r},t)$, $n(\mathbf{r},t)$ and $\mathbf{J}(\mathbf{r},t)$ so that we need further equations to get a unique solvable system of equations. One of the equations we are looking for is named drift-diffusion current equation and will be derived in the next section.

3.2 Drift-Diffusion Current Equation

To derive an equation for the current $J(\mathbf{r},t)$ we start again from the Boltzmann equation. For this purpose it is not necessary to consider a generation term. Multiplying the Boltzmann equation (3.15) with an arbitrary function $\xi(\mathbf{k})$ and integrating it over the entire k-space results in

$$\underbrace{\int \xi(\mathbf{k}) \frac{\partial f(\mathbf{r},\mathbf{k},t)}{\partial t}\, d^3k}_{Term1} + \underbrace{\int \xi(\mathbf{k}) \mathbf{v}(\mathbf{k}) \cdot \frac{\partial f(\mathbf{r},\mathbf{k},t)}{\partial \mathbf{r}}\, d^3k}_{Term2} + \underbrace{\int \xi(\mathbf{k}) \dot{\mathbf{k}} \cdot \frac{\partial f(\mathbf{r},\mathbf{k},t)}{\partial \mathbf{k}}\, d^3k}_{Term3}$$
$$= \underbrace{\int \xi(\mathbf{k}) f(\mathbf{r},\mathbf{k},t) \int S(\mathbf{k},\mathbf{k}') \left[\frac{\xi(\mathbf{k}')}{\xi(\mathbf{k})} - 1 \right] d^3k'\, d^3k}_{Term4}. \tag{3.42}$$

To obtain Eq. (3.42) we additionally made use of the relation

$$\dot{\mathbf{r}} = \frac{\mathbf{p}}{m} = \mathbf{v}, \tag{3.43}$$

between the momentum $\mathbf{p}$, the mass m and the velocity $\mathbf{v}$. For reasons of clarity, the individual terms are simplified separately. It is possible to exchange integration and differentiation which leads to

$$\int \xi(\mathbf{k}) \frac{\partial f(\mathbf{r},\mathbf{k},t)}{\partial t}\, d^3k = \frac{\partial}{\partial t} \int \xi(\mathbf{k}) f(\mathbf{r},\mathbf{k},t)\, d^3k. \tag{3.44}$$

In the second term it is also possible to exchange integration and differentiation which yields

$$\int \xi(\mathbf{k})\mathbf{v}(\mathbf{k}) \cdot \frac{\partial}{\partial \mathbf{r}} f(\mathbf{r},\mathbf{k},t)\ d^3k = \frac{\partial}{\partial \mathbf{r}} \cdot \int \xi(\mathbf{k})\mathbf{v}(\mathbf{k}) f(\mathbf{r},\mathbf{k},t)\ d^3k. \tag{3.45}$$

At this point it is useful to express the product

$$\xi(\mathbf{k})\mathbf{v}(\mathbf{k}) = \mathbf{g}(\mathbf{k}) \tag{3.46}$$

by a new vector which yields

$$\int \xi(\mathbf{k})\mathbf{v}(\mathbf{k}) \cdot \frac{\partial}{\partial \mathbf{r}} f(\mathbf{r},\mathbf{k},t)\ d^3k = \frac{\partial}{\partial \mathbf{r}} \cdot \int \mathbf{g}(\mathbf{k}) f(\mathbf{r},\mathbf{k},t)\ d^3k. \tag{3.47}$$

By taking advantage of Eq. (3.23) we get

$$\int \xi(\mathbf{k})\mathbf{v}(\mathbf{k}) \cdot \frac{\partial}{\partial \mathbf{r}} f(\mathbf{r},\mathbf{k},t)\ d^3k = 4\pi^3 \frac{\partial}{\partial \mathbf{r}} \left[\overline{\mathbf{g}} n(\mathbf{r},t)\right] \tag{3.48}$$

with

$$\overline{\mathbf{g}} = \frac{\int \mathbf{g}(\mathbf{k}) f(\mathbf{r},\mathbf{k},t)\ d^3k}{\int f(\mathbf{r},\mathbf{k},t)\ d^3k}. \tag{3.49}$$

This term can also be written as

$$\int \xi(\mathbf{k})\mathbf{v}(\mathbf{k}) \cdot \frac{\partial}{\partial \mathbf{r}} f(\mathbf{r},\mathbf{k},t)\ d^3k = 4\pi^3 \left\{ \frac{\partial}{\partial r_x} \left[\overline{g}_x n(\mathbf{r},t)\right] + \frac{\partial}{\partial r_y} \left[\overline{g}_y n(\mathbf{r},t)\right] + \frac{\partial}{\partial r_z} \left[\overline{g}_z n(\mathbf{r},t)\right] \right\} \tag{3.50}$$

with

$$\mathbf{r} = (r_x, r_y, r_z). \tag{3.51}$$

Now, we proceed with the third term. Using Eq. (3.30) yields

$$\int \xi(\mathbf{k})\dot{\mathbf{k}} \cdot \frac{\partial f(\mathbf{r},\mathbf{k},t)}{\partial \mathbf{k}}\ d^3k = \int \xi(\mathbf{k}) \frac{1}{\hbar} \mathbf{F}(\mathbf{r},\mathbf{k},t) \cdot \frac{\partial f(\mathbf{r},\mathbf{k},t)}{\partial \mathbf{k}}\ d^3k. \tag{3.52}$$

In order to further simplify the term we need Eq. (3.35) and obtain

$$\int \xi(\mathbf{k})\dot{\mathbf{k}} \cdot \frac{\partial f(\mathbf{r},\mathbf{k},t)}{\partial \mathbf{k}}\ d^3k = \frac{e}{\hbar} \int \xi(\mathbf{k}) \mathbf{E}(\mathbf{r},t) \cdot \frac{\partial f(\mathbf{r},\mathbf{k},t)}{\partial \mathbf{k}}\ d^3k. \tag{3.53}$$

Taking advantage of the vector identity (3.32) yields for term three

$$\begin{aligned} \int \xi(\mathbf{k})\dot{\mathbf{k}} \cdot \frac{\partial f(\mathbf{r},\mathbf{k},t)}{\partial \mathbf{k}}\ d^3k = & \frac{e}{\hbar} \int \frac{\partial}{\partial \mathbf{k}} \cdot \left[\xi(\mathbf{k}) \mathbf{E}(\mathbf{r},t) f(\mathbf{r},\mathbf{k},t)\right]\ d^3k \\ & - \frac{e}{\hbar} \int f(\mathbf{r},\mathbf{k},t) \mathbf{E}(\mathbf{r},t) \cdot \frac{\partial}{\partial \mathbf{k}} \xi(\mathbf{k})\ d^3k. \end{aligned} \tag{3.54}$$

With Gauss' theorem we can transform the first part of Eq. (3.54) into a surface integral. This surface integral vanishes, because $f(\mathbf{r},\mathbf{k},t)$ is always finite and goes to zero for $|\mathbf{k}| \to \infty$. It follows

$$\int \xi(\mathbf{k})\dot{\mathbf{k}} \cdot \frac{\partial f(\mathbf{r},\mathbf{k},t)}{\partial \mathbf{k}}\, d^3k = -\frac{e}{\hbar}\int f(\mathbf{r},\mathbf{k},t)\mathbf{E}(\mathbf{r},t) \cdot \frac{\partial}{\partial \mathbf{k}}\xi(\mathbf{k})\, d^3k. \tag{3.55}$$

Next we proceed with term four

$$\int \xi(\mathbf{k}) f(\mathbf{r},\mathbf{k},t) \int S(\mathbf{k},\mathbf{k}') \left[\frac{\xi(\mathbf{k}')}{\xi(\mathbf{k})} - 1\right]\, d^3k'\, d^3k = -\int \xi(\mathbf{k}) f(\mathbf{r},\mathbf{k},t)\frac{1}{\tau(\mathbf{k})}\, d^3k \tag{3.56}$$

by defining

$$\frac{1}{\tau(\mathbf{k})} := \int S(\mathbf{k},\mathbf{k}') \left[1 - \frac{\xi(\mathbf{k}')}{\xi(\mathbf{k})}\right]\, d^3k', \tag{3.57}$$

we obtain

$$\int \xi(\mathbf{k}) f(\mathbf{r},\mathbf{k},t) \int S(\mathbf{k},\mathbf{k}') \left[\frac{\xi(\mathbf{k}')}{\xi(\mathbf{k})} - 1\right]\, d^3k'\, d^3k = -\frac{1}{\overline{\tau}(\mathbf{r},t)}\int \xi(\mathbf{k}) f(\mathbf{r},\mathbf{k},t)\, d^3k \tag{3.58}$$

with

$$\frac{1}{\overline{\tau}(\mathbf{r},t)} = \frac{\int \xi(\mathbf{k}) f(\mathbf{r},\mathbf{k},t)\frac{1}{\tau(\mathbf{k})}}{\int \xi(\mathbf{k}) f(\mathbf{r},\mathbf{k},t)}. \tag{3.59}$$

Now, we make use of Eq. (3.27) and get

$$\int \xi(\mathbf{k}) f(\mathbf{r},\mathbf{k},t) \int S(\mathbf{k},\mathbf{k}') \left[\frac{\xi(\mathbf{k}')}{\xi(\mathbf{k})} - 1\right]\, d^3k'\, d^3k = -\frac{4\pi^3}{\overline{\tau}(\mathbf{r},t)} n(\mathbf{r},t)\overline{\xi} \tag{3.60}$$

with

$$\overline{\xi} = \frac{\int \xi(\mathbf{k}) f(\mathbf{r},\mathbf{k},t)\, d^3k}{\int f(\mathbf{r},\mathbf{k},t)\, d^3k}. \tag{3.61}$$

To continue, we now assume for the arbitrary function

$$\xi(\mathbf{k}) = \frac{\hbar}{m}k_i, \tag{3.62}$$

for $i = x, y, z$. If we further consider the relation (3.43) and Eq. (3.9), we can write

$$\overline{v}_i = \frac{\hbar}{m}\frac{\int k_i f(\mathbf{r},\mathbf{k},t)\, d^3k}{\int f(\mathbf{r},\mathbf{k},t)\, d^3k}. \tag{3.63}$$

for $i = x, y, z$. Using this result for term four yields

$$\int \xi(\mathbf{k}) f(\mathbf{r},\mathbf{k},t) \int S(\mathbf{k},\mathbf{k}') \left[\frac{\xi(\mathbf{k}')}{\xi(\mathbf{k})} - 1\right] \, d^3k' \, d^3k = -\frac{4\pi^3}{\overline{\tau}(\mathbf{r},t)} n(\mathbf{r},t)\overline{v}_i, \tag{3.64}$$

for $i = x, y, z$. The ansatz, Eq. (3.62), in combination with Eq. (3.23) yields

$$\int \xi(\mathbf{k}) \frac{\partial f(\mathbf{r},\mathbf{k},t)}{\partial t} \, d^3k = 4\pi^3 \frac{\partial}{\partial t} \left[\overline{v}_i n(\mathbf{r},t)\right], \; i = x, y, z \tag{3.65}$$

for the first term.

In the next step we use Eq. (3.46) to obtain

$$\begin{aligned}\int \xi(\mathbf{k}) \mathbf{v}(\mathbf{k}) \cdot \frac{\partial}{\partial \mathbf{r}} f(\mathbf{r},\mathbf{k},t) \, d^3k =& 4\pi^3 \frac{\partial}{\partial r_x} \left[\overline{v_i v_x} n(\mathbf{r},t)\right] + 4\pi^3 \frac{\partial}{\partial r_y} \left[\overline{v_i v_y} n(\mathbf{r},t)\right] \\ &+ 4\pi^3 \frac{\partial}{\partial r_z} \left[\overline{v_i v_z} n(\mathbf{r},t)\right], \; i = x, y, z \end{aligned} \tag{3.66}$$

for the second term (3.50), where

$$\overline{v_i v_j} = \frac{\hbar^2}{m^2} \frac{\int k_i k_j f(\mathbf{r},\mathbf{k},t) \, d^3k}{\int f(\mathbf{r},\mathbf{k},t) \, d^3k}. \tag{3.67}$$

Now we split the non-equilibrium probability density function $f(\mathbf{r},\mathbf{k},t)$ into a symmetric part $f_S(\mathbf{r},\mathbf{k},t)$ and an anti-symmetric part $f_A(\mathbf{r},\mathbf{k},t)$ as described in Eq. (3.12) and get

$$\overline{v_i v_j} = \frac{\hbar^2}{m^2} \frac{\int k_i k_j f_S(\mathbf{r},\mathbf{k},t) \, d^3k + \int k_i k_j f_A(\mathbf{r},\mathbf{k},t) \, d^3k}{\int f_S(\mathbf{r},\mathbf{k},t) \, d^3k + \int f_A(\mathbf{r},\mathbf{k},t) \, d^3k}. \tag{3.68}$$

This equation can be simplified due to the fact that the integral over an anti-symmetric function is always zero which leads to

$$\overline{v_i v_j} = \frac{\hbar^2}{m^2} \frac{\int k_i k_j f_S(\mathbf{r},\mathbf{k},t) \, d^3k + \int k_i k_j f_A(\mathbf{r},\mathbf{k},t) \, d^3k}{\int f_S(\mathbf{r},\mathbf{k},t) \, d^3k}. \tag{3.69}$$

Now we have to distinguish between $i = j$ and $i \neq j$ for $i = x, y, z$ and $j = x, y, z$.

For $\overline{v_i v_j}$ with $i \neq j$ we obtain

$$\begin{aligned}\overline{v_i v_j} = \frac{\hbar^2}{m^2} \frac{1}{\int f_S(\mathbf{r},\mathbf{k},t) \, d^3k} \Bigg[&\int \int k_y \int k_x \, f_S(\mathbf{r},k_x,k_y,k_z,t) \, dk_x \, dk_y \, dk_z \\ &+ \int k_x \int k_y \int f_A(\mathbf{r},k_x,k_y,k_z,t) \, dk_z \, dk_y \, dk_x \Bigg], \end{aligned} \tag{3.70}$$

for instance for $i = x$ and $j = y$. Since k_x is anti-symmetric the product $k_x f_S(\mathbf{r},k_x,k_y,k_z,t)$ is always anti-symmetric and, therefore, the integral

$\int k_x f_S(\mathbf{r}, k_x, k_y, k_z, t)\, dk_x$ is zero. The integral $\int f_A(\mathbf{r}, k_x, k_y, k_z, t) dk_z$ in the second part is still anti-symmetric and, therefore, zero which leads to

$$\overline{v_i v_j} = 0, \tag{3.71}$$

for $i = x, y, z$ and $j = x, y, z$ and $i \neq j$.

For $\overline{v_i v_i}$ we obtain

$$\overline{v_i v_i} = \frac{\hbar^2}{m^2} \frac{1}{\int f_S(\mathbf{r}, \mathbf{k}, t)\, d^3k} \left[\int\int\int k_x^2\, f_S(\mathbf{r}, k_x, k_y, k_z, t)\, dk_x\, dk_y\, dk_z \right. \\ \left. + \int k_x^2 \int\int f_A(\mathbf{r}, k_x, k_y, k_z, t)\, dk_z\, dk_y\, dk_x \right], \tag{3.72}$$

for instance for $i = x$. Again the integral $\int f_A(\mathbf{r}, k_x, k_y, k_z, t) dk_z$ in the second part is anti-symmetric and, therefore, zero which leads to

$$\overline{v_i v_i} = \frac{\hbar^2}{m^2} \frac{\int k_i^2 f_S(\mathbf{r}, \mathbf{k}, t)\, d^3k}{\int f_S(\mathbf{r}, \mathbf{k}, t)\, d^3k}, \tag{3.73}$$

for i=x, y, z. Next we fit the symmetric density function $f_S(\mathbf{r}, \mathbf{k}, t)$ with a Fermi-Dirac function, Eq. (3.13), which yields

$$\overline{v_i v_i} = \frac{\hbar^2}{m^2} \frac{\int k_i^2 \frac{1}{1+e^{\frac{W_C(\mathbf{r},\mathbf{k}) - W_n(t)}{k_B T}}}\, d^3k}{\int \frac{1}{1+e^{\frac{W_C(\mathbf{r},\mathbf{k}) - W_n(t)}{k_B T}}}\, d^3k}, \tag{3.74}$$

for $i = x, y, z$. In addition to the assumption of a parabolic energy dispersion, Eq. (3.7), we must assume that the Fermi-Dirac function can be approximated by a Maxwell-Boltzmann distribution. Due to this simplification we get

$$\overline{v_i v_i} = \frac{\hbar^2}{m^2} \frac{\int k_i^2 exp\left[-\frac{W_0(\mathbf{r}) + \frac{\mathbf{k}^2\hbar^2}{2m} - W_n(t)}{k_B T} \right] d^3k}{\int exp\left[-\frac{W_0(\mathbf{r}) + \frac{\mathbf{k}^2\hbar^2}{2m} - W_n(t)}{k_B T} \right] d^3k}, \tag{3.75}$$

for $i = x, y, z$. Instead of Eq. (3.75) we can also write

$$\overline{v_i v_i} = \frac{\hbar^2}{m^2} \frac{\int k_i^2 exp\left[-\frac{W_0(\mathbf{r}) + \frac{(k_x^2 + k_y^2 + k_z^2)\hbar^2}{2m} - W_n(t)}{k_B T} \right] d^3k}{\int exp\left[-\frac{W_0(\mathbf{r}) + \frac{(k_x^2 + k_y^2 + k_z^2)\hbar^2}{2m} - W_n(t)}{k_B T} \right] d^3k}, \tag{3.76}$$

for $i = x, y, z$. Reducing Eq. (3.76) yields

$$\overline{v_i v_i} = \frac{\hbar^2}{m^2} \frac{\int k_i^2 exp\left[-\frac{\frac{k_i^2\hbar^2}{2m}}{k_B T} \right] dk_i}{\int exp\left[-\frac{\frac{k_i^2\hbar^2}{2m}}{k_B T} \right] dk_i}, \tag{3.77}$$

for $i = x, y, z$. To proceed we will first calculate the integral in the denominator. For a better overview we summarize the constants in the exponential function

$$a = \frac{\hbar^2}{2mk_BT} \tag{3.78}$$

and obtain

$$\int_{-\infty}^{\infty} exp\left[-\frac{\frac{k_i^2\hbar^2}{2m}}{k_BT}\right]\, dk_i = \int_{-\infty}^{\infty} e^{-ak_i^2}\, dk_i = \frac{1}{\sqrt{a}}\int_{-\infty}^{\infty} e^{-y^2}\, dy = \frac{\sqrt{\pi}}{\sqrt{a}}, \tag{3.79}$$

with

$$ak_i^2 = y^2, \tag{3.80}$$

$$k_i = \frac{1}{\sqrt{a}}y, \tag{3.81}$$

$$dk_i = \frac{1}{\sqrt{a}}dy, \tag{3.82}$$

for $i = x, y, z$. Now we proceed with the nominator in Eq. (3.77) and obtain

$$\int_{-\infty}^{\infty} k_i^2 e^{-ak_i^2}\, dk_i = a^{-\frac{3}{2}}\int_{-\infty}^{\infty} y^2 e^{-y^2}\, dy = a^{-\frac{3}{2}}\frac{1}{2}\sqrt{\pi} \tag{3.83}$$

for $i = x, y, z$. Now we can insert Eq.(3.79) and Eq. (3.83) into Eq. (3.77) and get

$$\overline{v_iv_i} = \frac{\hbar^2}{m^2}\frac{\frac{1}{2}\sqrt{\pi}a^{-\frac{3}{2}}}{\sqrt{\pi}a^{-\frac{1}{2}}} = \frac{\hbar^2}{2m^2}\frac{1}{a}, \tag{3.84}$$

for $i = x, y, z$. Finally, we insert Eq. (3.78) into this result and get

$$\overline{v_iv_i} = \frac{k_BT}{m}, \tag{3.85}$$

for $i = x, y, z$. Inserting this result in combination with Eq. (3.71) into Eq. (3.66) yields

$$\begin{aligned}\int \xi(\mathbf{k})\mathbf{v}(\mathbf{k}) \cdot \frac{\partial}{\partial \mathbf{r}} f(\mathbf{r}, \mathbf{k}, t)\, d^3k =& 4\pi^3 \frac{\partial}{\partial r_i}\left[\overline{v_iv_i} n(\mathbf{r}, t)\right] \\ =& 4\pi^3 \frac{k_BT}{m}\frac{\partial}{\partial r_i} n(\mathbf{r}, t),\end{aligned} \tag{3.86}$$

for $i = x, y, z$.

If we now continue to simplify Eq. (3.55), we have to consider Eq. (3.62) and

get

$$\begin{aligned}\int \xi(\mathbf{k})\dot{\mathbf{k}}\cdot\frac{\partial f(\mathbf{r},\mathbf{k},t)}{\partial\mathbf{k}}\,d^3k &= -\frac{e}{m}\int f(\mathbf{r},\mathbf{k},t)\mathbf{E}(\mathbf{r},t)\cdot\begin{pmatrix}\frac{\partial}{\partial k_x}k_i\\ \frac{\partial}{\partial k_y}k_i\\ \frac{\partial}{\partial k_z}k_i\end{pmatrix}\,d^3k\\ &= -\frac{e}{m}\int f(\mathbf{r},\mathbf{k},t)\left[E_x(\mathbf{r},t)\frac{\partial}{\partial k_x}k_i + E_y(\mathbf{r},t)\frac{\partial}{\partial k_y}k_i + E_z(\mathbf{r},t)\frac{\partial}{\partial k_z}k_i\right]\,d^3k\\ &= -\frac{e}{m}E_i(\mathbf{r},t)\int f(\mathbf{r},\mathbf{k},t)\,d^3k,\quad i=x,y,z \end{aligned} \tag{3.87}$$

for the third term. Finally we use Eq. (3.23) to obtain

$$\int \xi(\mathbf{k})\dot{\mathbf{k}}\cdot\frac{\partial f(\mathbf{r},\mathbf{k},t)}{\partial\mathbf{k}}\,d^3k = -4\pi^3\frac{e}{m}E_i(\mathbf{r},t)n(\mathbf{r},t). \tag{3.88}$$

for $i=x,y,z$.

Summarizing the terms Eq. (3.64), Eq. (3.65), Eq. (3.86) and Eq. (3.88) according to Eq. (3.42) yields

$$\frac{\partial}{\partial t}\left[\overline{v}_i n(\mathbf{r},t)\right] + \frac{k_B T}{m}\frac{\partial}{\partial r_i}n(\mathbf{r},t) - \frac{e}{m}E_i(\mathbf{r},t)n(\mathbf{r},t) = -\frac{1}{\overline{\tau}(\mathbf{r},t)}n(\mathbf{r},t)\overline{v}_i, \tag{3.89}$$

for $i=x,y,z$. These three equations are equivalent to

$$\frac{\partial}{\partial t}\left[\overline{\mathbf{v}} n(\mathbf{r},t)\right] + \frac{k_B T}{m}\frac{\partial}{\partial \mathbf{r}}n(\mathbf{r},t) - \frac{e}{m}\mathbf{E}(\mathbf{r},t)n(\mathbf{r},t) = -\frac{1}{\overline{\tau}(\mathbf{r},t)}n(\mathbf{r},t)\overline{\mathbf{v}}. \tag{3.90}$$

Multiplying it with $e\overline{\tau}(\mathbf{r},t)$ results in

$$\overline{\tau}(\mathbf{r},t)\frac{\partial}{\partial t}\left[e\overline{\mathbf{v}} n(\mathbf{r},t)\right] + \frac{e\overline{\tau}(\mathbf{r},t)}{m}k_B T\frac{\partial}{\partial \mathbf{r}}n(\mathbf{r},t) - \frac{e\overline{\tau}(\mathbf{r},t)}{m}e\mathbf{E}(\mathbf{r},t)n(\mathbf{r},t) = -en(\mathbf{r},t)\overline{\mathbf{v}}. \tag{3.91}$$

Now we use (3.40) and get

$$\overline{\tau}(\mathbf{r},t)\frac{\partial}{\partial t}\mathbf{J}(\mathbf{r},t) + \frac{e\overline{\tau}(\mathbf{r},t)}{m}k_B T\frac{\partial}{\partial \mathbf{r}}n(\mathbf{r},t) - \frac{e\overline{\tau}(\mathbf{r},t)}{m}e\mathbf{E}(\mathbf{r},t)n(\mathbf{r},t) = -\mathbf{J}(\mathbf{r},t). \tag{3.92}$$

We assume that in semiconductors the relaxation time $\overline{\tau}(\mathbf{r},t)$ is small compared to characteristic time constants in the drift-diffusion approximation. Hence, we can neglect the first term in Eq. (3.92) [15]:

$$\frac{e\overline{\tau}(\mathbf{r},t)}{m}k_B T\frac{\partial}{\partial \mathbf{r}}n(\mathbf{r},t) - \frac{e\overline{\tau}(\mathbf{r},t)}{m}e\mathbf{E}(\mathbf{r},t)n(\mathbf{r},t) = -\mathbf{J}(\mathbf{r},t). \tag{3.93}$$

To proceed we have to define the charge of the particles. Let us assume electrons which have negative elementary charge $e=-q=-1.602176\cdot10^{-19}C$ which leads to

$$-\frac{q\overline{\tau}(\mathbf{r},t)}{m}k_B T\frac{\partial}{\partial \mathbf{r}}n(\mathbf{r},t) - \frac{q\overline{\tau}(\mathbf{r},t)}{m}q\mathbf{E}(\mathbf{r},t)n(\mathbf{r},t) = -\mathbf{J}(\mathbf{r},t). \tag{3.94}$$

To bring the resulting equations in a well-known form we need the Einstein relation [13]

$$D(\mathbf{r},t) = \mu(\mathbf{r},t)\frac{k_B T}{q}, \tag{3.95}$$

and the definition of the mobility [13]

$$\mu(\mathbf{r},t) = \frac{q\overline{\tau}(\mathbf{r},t)}{m}. \tag{3.96}$$

Taking advantage of this relations yields the drift-diffusion current equation for electrons:

$$\mathbf{J}_n(\mathbf{r},t) = \mu_n(\mathbf{r},t)q\mathbf{E}(\mathbf{r},t)n_n(\mathbf{r},t) + q\ D_n(\mathbf{r},t)\frac{\partial}{\partial\mathbf{r}}n_n(\mathbf{r},t). \tag{3.97}$$

In Eq. (3.95), $D(\mathbf{r},t)$ is the diffusion constant. In general, different particle types have different mobilities $\mu(\mathbf{r},t)$ or diffusions constants $D(\mathbf{r},t)$ so that the variables are normally provided with an index for the particle species. As index for electrons in Eq. (3.97) we used the subscript n.

For holes we obtain from Eq. (3.91) due to their charge of $e = q = 1.602176 \cdot 10^{-19}C$:

$$\mathbf{J}_p(\mathbf{r},t) = \mu_p(\mathbf{r},t)q\mathbf{E}(\mathbf{r},t)n_p(\mathbf{r},t) - q\ D_p(\mathbf{r},t)\frac{\partial}{\partial\mathbf{r}}n_p(\mathbf{r},t). \tag{3.98}$$

As index for this particle species we used the subscript p. To obtain the drift-diffusion equation for electrons we insert Eq. (3.97) into Eq. (3.41) and get

$$\frac{\partial}{\partial t}n_n(\mathbf{r},t) - \frac{1}{q}\frac{\partial}{\partial\mathbf{r}}\cdot\left[\mu_n(\mathbf{r},t)q\mathbf{E}(\mathbf{r},t)n_n(\mathbf{r},t) + q\ D_n(\mathbf{r},t)\frac{\partial}{\partial\mathbf{r}}n_n(\mathbf{r},t)\right] = R(\mathbf{r},t). \tag{3.99}$$

Inserting Eq. (3.98) into Eq. (3.41) yields the drift-diffusion equation for holes:

$$\frac{\partial}{\partial t}n_p(\mathbf{r},t) + \frac{1}{q}\frac{\partial}{\partial\mathbf{r}}\cdot\left[\mu_p(\mathbf{r},t)q\mathbf{E}(\mathbf{r},t)n_p(\mathbf{r},t) - q\ D_p(\mathbf{r},t)\frac{\partial}{\partial\mathbf{r}}n_p(\mathbf{r},t)\right] = R(\mathbf{r},t). \tag{3.100}$$

For uncharged particles, which are not influenced by the electric field, the drift-diffusion equation (3.99) or (3.100) can be simplified to the normal diffusion equation

$$\frac{\partial}{\partial t}n(\mathbf{r},t) - \frac{\partial}{\partial\mathbf{r}}\cdot\left[D(\mathbf{r},t)\frac{\partial}{\partial\mathbf{r}}n(\mathbf{r},t)\right] = R(\mathbf{r},t). \tag{3.101}$$

Now we have to determine the source or sink term $R(\mathbf{r},t)$, which is still unknown.

3.3 Source or Sink Term $R(\mathbf{r},t)$

The source or the sink term $R(\mathbf{r},t)$ is still undefined. So we have to use additional information to determine the function $R(\mathbf{r},t)$. Under normal circumstances particles

transform into each other, they do not simply disappear. For those conversion processes, normally approximations exists depending on the involved particles. One possible approach is that particles can only transform during collisions with each other. For example, we have three different particle types A, B and C. Each particle type is described by its own drift-diffusion equation. Now we assume that a particle from type A and B transforms into a single particle of type C if they collide. Based on this assumption the sink term from particle type A, $R(\mathbf{r},t)_A$, and particle type B, $R(\mathbf{r},t)_B$, has to be equal. As a consequence the source term of particle type C must be $R(\mathbf{r},t)_C = -R(\mathbf{r},t)_A$. It is assumed that the probability that two particles of different type collide with each other depend on the concentration of the different particle types. In this simplified view, the sink term of the particle type A and B depend on the number of collisions between this particle types and, therefore, on the concentration $n_A(\mathbf{r},t)$ of the particles A and the concentration $n_B(\mathbf{r},t)$ of the particles B:

$$\begin{aligned} R(\mathbf{r},t)_A &= R(\mathbf{r},t)_B \sim n_A(\mathbf{r},t) \\ R(\mathbf{r},t)_A &= R(\mathbf{r},t)_B \sim n_B(\mathbf{r},t) \\ R(\mathbf{r},t)_C &= -R(\mathbf{r},t)_A. \end{aligned} \tag{3.102}$$

This approach [16][17] leads to the equation

$$R(\mathbf{r},t)_A = R(\mathbf{r},t)_B = -R(\mathbf{r},t)_C = -k\, n_A(\mathbf{r},t)^\alpha\, n_B(\mathbf{r},t)^\beta, \tag{3.103}$$

which describes this conversion process and couples the different particle species. Under these circumstances the source and sink terms are also called reaction rates. In Eq. (3.103) k is the rate coefficient. In general, the rate coefficient k can vary in space and time because it can depend on a lot of conditions such as temperature, particle concentration, light incident, electric or magnetic fields. As a simplification, we assumed that the rate coefficient k is regarded as constant. The coefficients α and β characterize the order of the equation. Using these parameters, the reaction can be divided into fundamental groups. Zeroth-order reaction are the first group. With a zeroth-order reactions one means that the coefficients α and β are approximately zero. This leads to constant reaction rates

$$R_A(\mathbf{r},t) = R_B(\mathbf{r},t) = -R_C(\mathbf{r},t) = -k\, n_A(\mathbf{r},t)^0\, n_B(\mathbf{r},t)^0 = -k. \tag{3.104}$$

In this case the reaction rates are independent of the concentration of the particle types. The second group is the first-order reaction group. A first-order reaction is a reaction in which the reaction rate

$$R_A(\mathbf{r},t) = R_B(\mathbf{r},t) = -R_C(\mathbf{r},t) = -k\, n_A(\mathbf{r},t) \tag{3.105}$$

depends only on the concentration of only one species. ($\alpha = 1$ and $\beta = 0$). The next group is the second-order reaction group. In a second-order reaction the reaction rates depend on the concentration of the species A and B:

$$R_A(\mathbf{r},t) = R_B(\mathbf{r},t) = -R_C(\mathbf{r},t) = -k\, n_A(\mathbf{r},t) n_B(\mathbf{r},t) \tag{3.106}$$

Both coefficients α and β are one. If the same species react with each other a second-order reaction would be

$$R_A(\mathbf{r},t) = -R_C(\mathbf{r},t) = -k\ n_A(\mathbf{r},t)n_A(\mathbf{r},t) = -k\ n_A(\mathbf{r},t)^2. \tag{3.107}$$

All concentration dependencies of higher order are included in the n-order reaction group. A concentration-dependence of higher order as in Eq. (3.107) will lead to the n-order reaction

$$R_A(\mathbf{r},t) = -R_C(\mathbf{r},t) = -k\ n_A^n(\mathbf{r},t). \tag{3.108}$$

Reactions in which more than two particle species are involved also lead to an n-order reaction. For example a third-order reaction that depend on three particles:

$$R_A(\mathbf{r},t) = R_B(\mathbf{r},t) = -R_C(\mathbf{r},t) = -k\ n_A(\mathbf{r},t)n_B(\mathbf{r},t)n_C(\mathbf{r},t). \tag{3.109}$$

In many cases, however, only two components in the reaction play a significant role. Usually the other species can be neglected in the reaction. This again leads to a second-order reaction. As next step, we have to clear what happens if there are reactions in both directions. If there are forward and reverse reactions, we have to think about how this reactions influence each other. The forward reaction rate $R_f(\mathbf{r},t)$ on its own is described by Eq. (3.103):

$$R_f(\mathbf{r},t) = R_f(\mathbf{r},t)_A = R_f(\mathbf{r},t)_B = -R_f(\mathbf{r},t)_C = -k_1\ n_A(\mathbf{r},t)^{\alpha_1}n_B(\mathbf{r},t)^{\beta_1}. \tag{3.110}$$

If we now assume that the additional reverse reaction rate does not depend on the forward reaction process we could also describ the reverse reaction rate $R_r(\mathbf{r},t)$ by

$$R_r(\mathbf{r},t) = R_r(\mathbf{r},t)_C = -R_r(\mathbf{r},t)_A = -R_r(\mathbf{r},t)_B = -k_2\ n_C(\mathbf{r},t)^{\alpha_2}, \tag{3.111}$$

This approach leads to

$$R_A(\mathbf{r},t) = R_B(\mathbf{r},t) = -R_C(\mathbf{r},t) = R_f(\mathbf{r},t) - R_r(\mathbf{r},t), \tag{3.112}$$

for the entire reaction rate. Now we have a rate equation for the source or sink term $R(\mathbf{r},t)$, a carrier continuity equation for the particle density $n(\mathbf{r},t)$ and a drift-diffusion current equation for the current $\mathbf{J}(\mathbf{r},t)$ that occurs in the continuity equation. Since in the drift-diffusion current equation the electric field appears, we need in addition the Poisson equation.

3.4 The Poisson Equation

The Poisson equation is a partial differential equation of second order. It gives the electric potential for a given charge distribution. A simple way to derive the equation is to start from Gauss' law:

$$\operatorname{div} \mathbf{D}(\mathbf{r},t) = \varrho_f(\mathbf{r},t). \tag{3.113}$$

In Eq. (3.113) $\mathbf{D}(\mathbf{r},t)$ denotes the electric displacement field, $\varrho_f(\mathbf{r},t)$ is the free charge density. Now we need the definition of the electric displacement field:

$$\mathbf{D}(\mathbf{r},t) = \varepsilon_0 \mathbf{E}(\mathbf{r},t) + \mathbf{P}(\mathbf{r},t). \tag{3.114}$$

In Eq. (3.114) ε_0 is the permittivity of the free space and $\mathbf{P}(\mathbf{r},t)$ is the polarization of the medium. If we suppose that the medium is linear and instantaneously respond to changes in the electric field $\mathbf{E}(\mathbf{r},t)$, one can express the polarization by

$$\mathbf{P}(\mathbf{r},t) = \varepsilon_0 \chi(\mathbf{r}) \mathbf{E}(\mathbf{r},t), \tag{3.115}$$

where $\chi(\mathbf{r})$ is the electric susceptibility of the medium. Inserting Eq. (3.115) into Eq. (3.114) yields

$$\mathbf{D}(\mathbf{r},t) = \varepsilon_0 \left[1 + \chi(\mathbf{r})\right] \mathbf{E}(\mathbf{r},t). \tag{3.116}$$

The expression $1 + \chi(\mathbf{r}) = \varepsilon_r(\mathbf{r})$ is the relative permittivity of the material. Therefore we can also write

$$\mathbf{D}(\mathbf{r},t) = \varepsilon_0 \varepsilon_r(\mathbf{r}) \mathbf{E}(\mathbf{r},t). \tag{3.117}$$

Substituting this into Eq. (3.113) results in

$$\text{div}\left[\varepsilon_0 \varepsilon_r(\mathbf{r}) \mathbf{E}(\mathbf{r},t)\right] = \varrho_f(\mathbf{r},t). \tag{3.118}$$

Now we consider Faraday's law of induction

$$\text{rot}\ \mathbf{E}(\mathbf{r},t) = -\frac{\partial \mathbf{B}(\mathbf{r},t)}{\partial t}, \tag{3.119}$$

where $\mathbf{B}(\mathbf{r},t)$ denotes the magnetic flux field. By neglecting magnetic effects the curl of the electric field vanishes,

$$\text{rot}\ \mathbf{E}(\mathbf{r},t) = 0, \tag{3.120}$$

and it can be represented by a scalar potential $\phi(\mathbf{r},t)$:

$$\mathbf{E}(\mathbf{r},t) = -\text{grad}\ \phi(\mathbf{r},t). \tag{3.121}$$

Inserting this into Eq. (3.118) delivers the Poisson equation:

$$-\text{div}\left[\varepsilon_0 \varepsilon_r(\mathbf{r}) \text{grad}\ \phi(\mathbf{r},t)\right] = \varrho_f(\mathbf{r},t) \tag{3.122}$$

As a short notation in the literature one often uses the nabla operator

$$\nabla_r = \frac{\partial}{\partial \mathbf{r}} = \left[\frac{\partial}{\partial \mathbf{x}_1}, \frac{\partial}{\partial \mathbf{x}_2}, \frac{\partial}{\partial \mathbf{x}_3}\right] \tag{3.123}$$

with $\mathbf{r} = (x_1, x_2, x_3)$. Based on this compact notation, we get

$$\varepsilon_0 \nabla \cdot [\varepsilon_r(\mathbf{r}) \nabla \phi(\mathbf{r}, t)] = -\varrho_f(\mathbf{r}, t). \tag{3.124}$$

The free charge density $\varrho_f(\mathbf{r}, t)$ can be expressed by

$$\varrho_f(\mathbf{r}, t) = e\, n(\mathbf{r}, t), \tag{3.125}$$

which finally leads to

$$\varepsilon_0 \nabla \cdot [\varepsilon_r(\mathbf{r}) \nabla \phi(\mathbf{r}, t)] = -e\, n(\mathbf{r}, t). \tag{3.126}$$

In Eq. (3.125) $n(\mathbf{r}, t)$ is the particle density and e stands for the electric charge of the particles. For electrons the particle charge is the negative elementary charge $e = -q = -1.602176 \cdot 10^{-19} C$, for holes the particle charge is $e = q$. Now, we have all the necessary equations for the simulation of the charge carrier transport in organic semiconductors. In the following chapter all the equations will be summarized.

3.5 Summary

In this section, a summary of the resulting equations is presented. For a briefer notation we use the nabla operator $\nabla = \frac{\partial}{\partial \mathbf{r}}$. The system consists of the Poisson equation, Sec. 3.4, the carrier continuity equation, Sec. 3.1, with the reaction rate $R(\mathbf{r}, t)$, Sec. 3.3, and the drift-diffusion current equation, Sec. 3.2. If there are uncharged particles involved also the diffusion equation, Sec. 3.2, must be added. However, to set up the system of equations, one must first define which particles are considered. In a semiconductor different kinds of particles can appear. We consider the case, that both electrons and holes play a role in charge transport and that also neutral particles exist, which can decay into electrons and holes. These neutral particles are called excitons [18]. They can arise, for example, due to incident photons. For negatively charged electrons subscript A, for positively charged holes subscript B and for excitons subscript C is used in the following system of equations:

$$\begin{aligned}
\varepsilon_0 \nabla \cdot [\varepsilon_r(\mathbf{r}) \nabla \phi(\mathbf{r}, t)] &= q\,[n_A(\mathbf{r}, t) - n_B(\mathbf{r}, t)] \\
\frac{\partial}{\partial t} n_A(\mathbf{r}, t) - \frac{1}{q} \nabla \cdot \mathbf{J}_A(\mathbf{r}, t) &= R(\mathbf{r}, t)_A \\
\frac{\partial}{\partial t} n_B(\mathbf{r}, t) + \frac{1}{q} \nabla \cdot \mathbf{J}_B(\mathbf{r}, t) &= R(\mathbf{r}, t)_B \\
\frac{\partial}{\partial t} n_C(\mathbf{r}, t) - \nabla \cdot [D_C(\mathbf{r}) \nabla n_C(\mathbf{r}, t)] &= R(\mathbf{r}, t)_C \\
\mathbf{J}_A(\mathbf{r}, t) &= -q \mu_A(\mathbf{r}, t) n_A(\mathbf{r}, t) \nabla \phi(\mathbf{r}, t) + q D_A(\mathbf{r}, t) \nabla n_A(\mathbf{r}, t) \\
\mathbf{J}_B(\mathbf{r}, t) &= -q \mu_B(\mathbf{r}, t) n_B(\mathbf{r}, t) \nabla \phi(\mathbf{r}, t) - q D_B(\mathbf{r}, t) \nabla n_B(\mathbf{r}, t) \\
R(\mathbf{r}, t)_A = R(\mathbf{r}, t)_B = -R(\mathbf{r}, t)_C &= k_2\, n_C(\mathbf{r}, t) - k_1\, n_A(\mathbf{r}, t)\, n_B(\mathbf{r}, t).
\end{aligned} \tag{3.127}$$

In (3.127) we expressed the electric field $\mathbf{E}(\mathbf{r}, t)$ through Eq. (3.121) and assumed that the exciton decay is a first-order reaction. The corresponding rate constant is k_2. For the process of the exciton generation out of electrons and holes a second-order reaction was assumed. The corresponding rate constant is k_1. Furthermore, electron-hole recombination effects have been neglected. To account for these effect the recombination term $R(\mathbf{r}, t)$ in the equations must be supplemented accordingly. An analytical solution of this system of equations is in most cases not possible. This system of partial differential equation must be supplemented by both initial and boundary conditions. Due to the boundary conditions, the problem depends also on the geometry of the semiconductor. The geometry of organic semiconductors, which we study in this thesis, can vary strongly. Hence, we need a numerical method to solve these partial differential equations. An appropriate method is discussed in the next chapter.

4 Finite Element Method

Many problems in physics can be described by differential equations. The explicit solution of these equations is usually not possible. For this reason, we are directed to methods which are able to solve approximately differential equations for a given problem. A widely used method is the method of finite elements. The simulations in this work were carried out based on this method.

This chapter consists of five sections. The first section describes a possible approach to the finite element method. Section two gives a brief insight into the possibilities of the discretization process of the base region. Section three deals with selected basis functions of individual element types used in this thesis. In the fourth section, a widely used numerical method for calculating two-dimensional integrals of polynomial functions is described. The last section deals with the resulting algebraic system of equations. This chapter is inspired by the Book „Methode der Finiten Elemente„ [19]. For a detailed description of the finite element method and an efficient implementation on the PC, the reader is referred to this book.

4.1 Method of Weighted Residuals

Two-dimensional time-dependent field problems, as they occur in this thesis, can in general be described by

$$\frac{\partial u(x,y,t)}{\partial t} = \frac{\partial}{\partial x}\left[k_1(x)\frac{\partial u(x,y,t)}{\partial x}\right] + \frac{\partial}{\partial y}\left[k_2(y)\frac{\partial u(x,y,t)}{\partial y}\right] - f(x,y,t), \tag{4.1}$$

combined with certain initial and boundary conditions. The differential equation is defined on a domain $G \subset \mathbb{R}^2$, see Fig. 4.1. The boundary C of the domain G consists of two parts C_1 and C_2 with $C_1 \cup C_2 = C$ and $C_1 \cap C_2 = 0$.

The idea of the method of weighted residuals is to approximate the unknown function $u(x,y,t)$ by using appropriately chosen basis functions $\varphi_0(x,y,t), \varphi_1(x,y), \ldots, \varphi_m(x,y)$ in the form of

$$u = \varphi_0(x,y,t) + \sum_{k=1}^{m} c_k(t)\varphi_k(x,y). \tag{4.2}$$

The functions φ_i have to be linearly independent. Thereby, $\varphi_0(x,y,t)$ is an arbitarly chosen function, which fulfills the inhomogeneous boundary conditions. With the remaining functions $\varphi_k(x,y)$ $k = 1, 2, \ldots, m$, the homogeneous boundary conditions must be

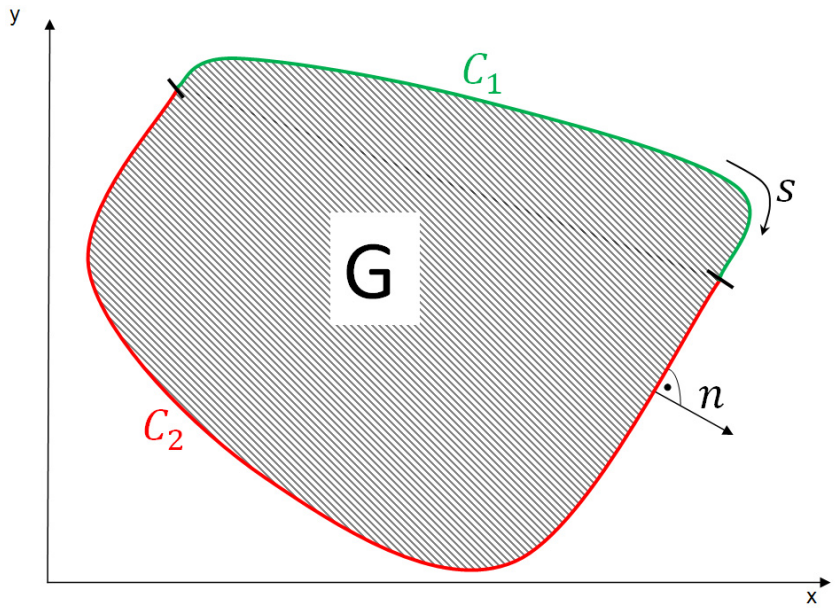

Fig. 4.1: Two-dimensional domain G on which the differential equation is defined.

met. This ensures that the function $u(x, y, t)$ satisfies both the homogeneous and the inhomogeneous boundary conditions throughout the domain G for any $c_k(t)$. At this stage, the coefficients $c_k(t)$ are still not defined. Therefore, we need an additional condition to define them. To achieve such a condition, we think about what would happen if we used random coefficients $c_k(t)$ in the differential equation (4.2). In general the differential equation would be fulfilled only poorly. There remains a so-called residual. The smaller this residual is, the better is the differential equation fulfilled. Therefore, the residual should be as small as possible inside the domain G. This can be achieved by requiring that the integral of the residual weighted with special linearly independent weight functions $W_i(x, y)$, i=1,2,...,m disappears. Based on the ansatz (4.2), this approach leads to m equations from which the coefficients $c_k(t)$ can be determined. In the method of Galerkin, the still undefined weight functions $W_i(x, y)$ are chosen to be equal to the functions $\varphi_k(x, y)$. Since the functions $\varphi_k(x, y)$ are linearly independent, this is always possible. To continue, we must consider a certain differential equation. First, we will explain the solution procedure for a time-independent differential equation. As an example, we choose the Poisson equation.

4.1.1 Application to a Stationary Field Problem

Let us consider the two-dimensional Poisson equation

$$u(x, y)_{xx} + u(x, y)_{yy} = f(x, y) \tag{4.3}$$

and the Dirichlet boundary condition

$$u(\zeta(s)) = \gamma_1(s) \tag{4.4}$$

on a part C_1 of the boundary as well as the Cauchy boundary conditions

$$\frac{\partial u(\zeta(s))}{\partial n(s)} + \alpha(s)u(\zeta(s)) = \gamma_2(s) \tag{4.5}$$

on a second part C_2 of the boundary. The function $\gamma_1(s) : [a, b] \to \mathbb{R}$ in Eq. (4.4) is a given function which prescribe the values of $u(x, y)$ on part C_1 of the boundary. The parameter $s \in [a, b]$ is the path length of the boundary. The variables a and b are constants which describe the beginning and the end of part C_1. The function $\zeta(s) : [a, b] \to \mathbb{R}^2$ in Eq. (4.4) and (4.5) transforms the path length into the spatial coordinates x and y. In Eq. (4.5) $\frac{\partial u(\zeta(s))}{\partial n(s)}$ is the partial derivation of $u(\zeta(s))$ with respect to the outer normal direction:

$$n(s) = \frac{\text{grad } u(\zeta(s))}{|| \text{ grad } u(\zeta(s)) ||}. \tag{4.6}$$

The functions $\alpha(s) : [a, b] \to \mathbb{R}$ and $\gamma_2(s) : [a, b] \to \mathbb{R}$ are given functions. In the special case that

$$\alpha(s) = \gamma_2(s) = 0, \tag{4.7}$$

the boundary condition is also called Neumann boundary condition. Now, the function $\varphi_0(x, y)$ should fulfill the inhomogeneous boundary conditions

$$\varphi_0(\zeta(s)) = \gamma_1(s) \text{ on } C_1 \text{ and } \frac{\partial \varphi_0(\zeta(s))}{\partial n(s)} + \alpha(s)\varphi_0(\zeta(s)) = \gamma_2(s) \text{ on } C_2. \tag{4.8}$$

The functions $\varphi_1(x, y)$,...,$\varphi_m(x, y)$ should satisfy the homogeneous boundary conditions

$$\varphi_k(\zeta(s)) = 0 \text{ on } C_1 \text{ and } \frac{\partial \varphi_k(\zeta(s))}{\partial n(s)} + \alpha(s)\varphi_k(\zeta(s)) = 0 \text{ on } C_2. \tag{4.9}$$

Inserting the ansatz (4.2) into the differential equation (4.3), by considering c_k as constant coefficients, gives the residual

$$\varphi_0(x, y)_{xx} + \varphi_0(x, y)_{yy} + \sum_{k=1}^{m} c_k \left[\varphi_k(x, y)_{xx} + \varphi_k(x, y)_{yy}\right] - f(x, y) = R(x, y). \tag{4.10}$$

According to Galerkin's method, the integrals

$$\iint_G R(x, y)\varphi_j(x, y)\, dxdy = 0, \quad j = 1, 2, \ldots, m \tag{4.11}$$

have to disappear on the domain G. The insertion of Eq. (4.10) into Eq. (4.11) leads to

$$\begin{aligned} &\iint_G \left[\varphi_0(x, y)_{xx} + \varphi_0(x, y)_{yy}\right] \varphi_j(x, y)\, dxdy \\ &+ \iint_G \left\{ \sum_{k=1}^{m} c_k \left[\varphi_k(x, y)_{xx} + \varphi_k(x, y)_{yy}\right] \varphi_j(x, y) \right\} dxdy \\ &- \iint_G f(x, y)\varphi_j(x, y)\, dxdy = 0, \quad j = 1, 2, \ldots, m. \end{aligned} \tag{4.12}$$

The integrands of the first two integrals have partial derivatives. They can be eliminated with the help of Green's formula

$$\iint_G [u(x,y)_{xx} + u(x,y)_{yy}]\, v(x,y)\, dxdy = -\iint_G \text{grad } u(x,y) \text{ grad } v(x,y)\, dxdy + \oint_C \frac{\partial u(\zeta(s))}{\partial n(s)} v(\zeta(s))\, ds, \tag{4.13}$$

which leads after interchanging integration and summation in connection with a multiplication by (-1) to

$$\begin{aligned}\sum_{k=1}^{m} c_k \left\{ \iint_G \text{grad } \varphi_k(x,y) \text{ grad } \varphi_j(x,y)\, dxdy - \oint_C \frac{\partial \varphi_k(\zeta(s))}{\partial n(s)} \varphi_j(\zeta(s))\, ds \right\} \\ + \iint_G \text{grad } \varphi_0(x,y) \text{ grad } \varphi_j(x,y)\, dxdy - \oint_C \frac{\partial \varphi_0(\zeta(s))}{\partial n(s)} \varphi_j(\zeta(s))\, ds \\ + \iint_G f(x,y)\varphi_j(x,y)\, dxdy = 0.\end{aligned} \tag{4.14}$$

At the boundary C_1 we have to consider that $\varphi_j(\zeta(s)) = 0$ for $j = 1, 2, \ldots, m$. Further, at the boundary C_2 the derivatives can be replaced by the boundary conditions, Eq. (4.8) and Eq. (4.9), which ultimately leads to

$$\begin{aligned}\sum_{k=1}^{m} c_k \left\{ \iint_G \text{grad } \varphi_k(x,y) \text{ grad } \varphi_j(x,y)\, dxdy + \int_{C_2} \alpha(s)\varphi_k(\zeta(s))\varphi_j(\zeta(s))\, ds \right\} \\ + \iint_G \text{grad } \varphi_0(x,y) \text{ grad } \varphi_j(x,y)\, dxdy + \int_{C_2} [\alpha(s)\varphi_0(\zeta(s)) - \gamma_2(s)]\, \varphi_j(\zeta(s))\, ds \\ + \iint_G f(x,y)\varphi_j(x,y)\, dxdy = 0,\end{aligned} \tag{4.15}$$

for j=1,2,...,m, which is a system of linear algebraic equations for the coefficients c_k. Now, let us consider a time-dependent problem. As an example, we choose the diffusion equation.

4.1.2 Application to a Time-Dependent Field Problem

Transient diffusion problems can be described by the two-dimensional diffusion or heat equation

$$u(x,y)_{xx} + u(x,y)_{yy} - f(x,y,t) - \frac{\partial u(x,y,t)}{\partial t} = 0 \tag{4.16}$$

with $(x,y) \in G$, $G \subset \mathbb{R}^2$ and $t \geq 0$. Given are the general time-dependent boundary conditions

$$\begin{aligned} u(\zeta(s),t) &= \gamma_1(s,t) \text{ on } C_1 \text{ for } t > 0, \\ \frac{\partial u(\zeta(s),t)}{\partial n(s)} + \alpha(s) u(\zeta(s),t) &= \gamma_2(s,t) \text{ on } C_2 \text{ for } t > 0 \end{aligned} \tag{4.17}$$

and the initial condition

$$u(x, y, 0) = u_0(x, y) \tag{4.18}$$

at time $t = 0$. The procedure for time-dependent problems consists again in representing the function $u(x, y, t)$ by

$$u(x, y, t) = \varphi_0(x, y, t) + \sum_{k=1}^{m} c_k(t)\varphi_k(x, y). \tag{4.19}$$

In contrast to the previous example, the coefficients c_k are now functions of time. The arbitrarily chosen function $\varphi_0(x, y, t)$ must satisfy the inhomogeneous boundary conditions on C_1 and C_2. The function $\varphi_k(x, y)$, however, must fulfill the time-independent homogeneous boundary conditions. Inserting the ansatz (4.19) into equation (4.16), reveals the residual as a function of space and time. This means that the integral over the residual, weighted with the linear-independent functions $\varphi_j(x, y)$, $j = 1, 2, \ldots, m$, must disappear:

$$\begin{aligned}\iint_G \Bigg\{ &\varphi_0(x, y, t)_{xx} + \varphi_0(x, y, t)_{yy} + \sum_{k=1}^{m} c_k(t) \left[\varphi_k(x, y)_{xx} + \varphi_k(x, y)_{yy}\right] - f(x, y, t) \\ &- \left[\frac{\partial \varphi_0(x, y, t)}{\partial t} + \sum_{k=1}^{m} \frac{\partial c_k(t)}{\partial t}\varphi_k(x, y)\right]\Bigg\} \varphi_j(x, y)\, dxdy = 0. \end{aligned} \tag{4.20}$$

By applying Green's formula with a subsequent interchange of integration and summation, the determining equations (4.20) can be transformed into

$$\begin{aligned}\sum_{k=1}^{m} c_k(t) &\left[-\iint_G \operatorname{grad} \varphi_k(x, y) \operatorname{grad} \varphi_j(x, y)\, dxdy + \oint_C \frac{\partial \varphi_k(\zeta(s))}{\partial n(s)} \varphi_j(\zeta(s))\, ds\right] \\ &- \sum_{k=1}^{m} \frac{dc_k(t)}{dt} \iint_G \varphi_k(x, y)\varphi_j(x, y)\, dxdy - \iint_G \operatorname{grad} \varphi_0(x, y, t) \operatorname{grad} \varphi_j(x, y)\, dxdy \\ &+ \oint_C \frac{\partial \varphi_0(\zeta(s), t)}{\partial n(s)} \varphi_j(\zeta(s))\, ds - \iint_G f(x, y, t)\varphi_j(x, y)\, dxdy \\ &- \iint_G \frac{\partial \varphi_0(x, y, t)}{\partial t} \varphi_j(x, y)\, dxdy = 0. \end{aligned} \tag{4.21}$$

If we consider the boundary conditions (4.17) we obtain

$$\begin{aligned}&\sum_{k=1}^{m} \frac{dc_k(t)}{dt} \iint_G \varphi_k(x, y)\varphi_j(x, y)\, dxdy \\ &+ \sum_{k=1}^{m} c_k(t) \left[\iint_G \operatorname{grad} \varphi_k(x, y) \operatorname{grad} \varphi_j(x, y)\, dxdy + \int_{C_2} \alpha(s)\varphi_k(\zeta(s))\varphi_j(\zeta(s))\, ds\right] \\ &+ \iint_G \left\{\operatorname{grad} \varphi_0(x, y, t) \operatorname{grad} \varphi_j(x, y) + \left[f(x, y, t) + \frac{\partial \varphi_0(x, y, t)}{\partial t}\right] \varphi_j(x, y)\right\}\, dxdy \\ &+ \int_{C_2} \left[\alpha(s)\varphi_0(\zeta(s), t) - \gamma_2(s)\right] \varphi_j(\zeta(s))\, ds = 0 \end{aligned} \tag{4.22}$$

for $j = 1, 2, \ldots, m$, which is a system of ordinary differential equations of first order for the coefficient functions $c_k(t)$.

Before we can solve this system of equations, we must define the still unknown basis functions $\varphi_1(x, y), \ldots, \varphi_m(x, y)$. The idea is to define this functions $\varphi_k(x, y)$ piecewise on subdomains G^e, $e = 1, 2, \ldots, z$, by means of local basis functions l_k^e:

$$\varphi_k(x, y) = \begin{cases} l_k^1(x, y), & (x, y) \in G^1, \\ l_k^2(x, y), & (x, y) \in G^2, \\ & \vdots \\ l_k^z(x, y), & (x, y) \in G^z. \end{cases} \tag{4.23}$$

We define these subdomains G^e, called elements, through a partition of the fundamental domain G into z parts. The boundary between two subdomains is always part of both subdomains. The superscripts in Eq. (4.23) indicates the elements, it is not an exponent. The discretisation process will be explained in the next section.

4.2 Partition of the Fundamental Domain

This section consists of two subsections. In the first subsection, the normalization process for elements is described. In the second subsection, the requirements of the functions for describing the elements are developed.

The elements G^e, $e = 1, 2, \ldots, z$, should approximate the ground area G as well as possible. On the other hand, the mathematical description of the elements should be not too complicated. Figure 4.2 shows a possible partition of a two-dimensional area using triangles and quadrangles. Also curvilinear elements, shown in Figure 4.3, are possible. Usually, one achieves a better approximation of the fundamental domain than with linear elements. This advantage is partly compensated by a higher computational effort. Mostly, one reaches a good approximation with linear elements by a sufficiently fine partition. When choosing the form of the elements, it is only necessary to ensure that the angles of the elements are not too sharp or blunt, because these cause numerical troubles. Since the elements can be freely combined, one obtains an extremely flexible description which is perfectly adapted to the mathematical problem in the considered domain. In three-dimensional problems, a partition using tetrahedral or square elements takes place. In order not to define special functions $l_k^e(x, y)$ ($e = 1, 2, \ldots, z$ and $k = 1, 2, \ldots, m$) for each element G^e, we transform the elements into unit elements G^0. Then, there is only one function type necessary per unit element. These functions $l_k^0(x, y)$ are called local basis functions and the transform process is called normalization.

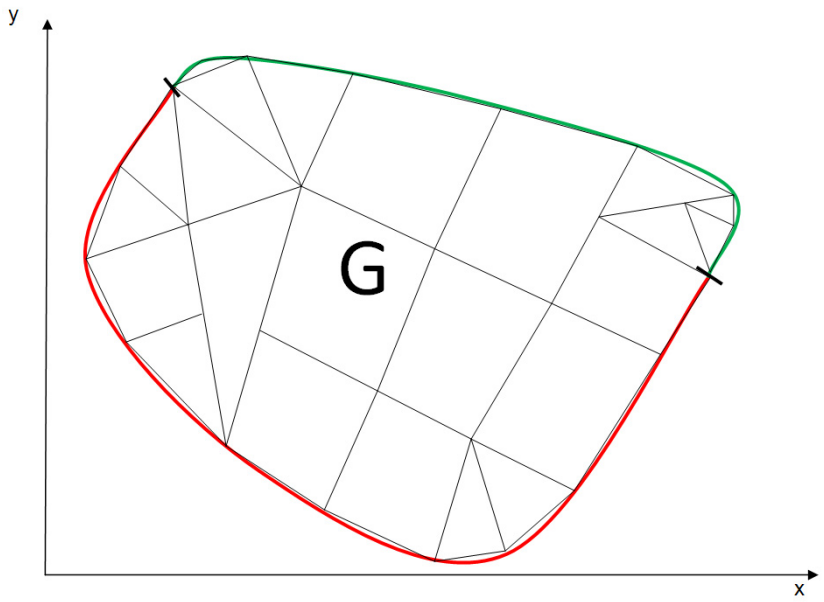

Fig. 4.2: Division of a given domain into subdomains with triangles and quadrangles.

4.2.1 Normalization of the Elements

When transforming the elements, we also have to consider the integral over the residuum, Eq. (4.11). In the method of Galerkin integrals of the type

$$\iint_{G^i} u(x,y,t)\,dxdy, \tag{4.24}$$

$$\iint_{G^i} u^2(x,y,t)\,dxdy, \tag{4.25}$$

$$\iint_{G^i} \left[\frac{\partial u(x,y,t)}{\partial x}\right]^2 + \left[\frac{\partial u(x,y,t)}{\partial y}\right]^2 dxdy, \tag{4.26}$$

for all elements of the area G could appear. For an efficient calculation of these integrals a transformation into unit elements is a major advantage. Thus, the integrals will become independent of the individual shape of the triangles or quadrangles. For this purpose, we must find a bijective transformation for each type of elements. In order to standardize the integration of the elements, the triangular elements will be transformed into unit triangles, Fig. 4.4, and the parallelograms are transformed into unit quadrates, Fig. 4.5.

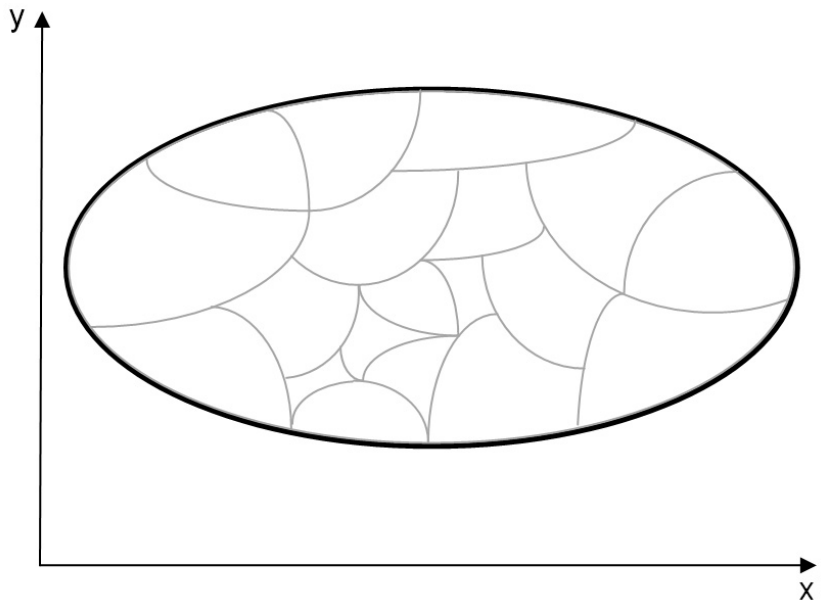

Fig. 4.3: Division of a given domain into subdomains with curvilinear triangles and quadrangles.

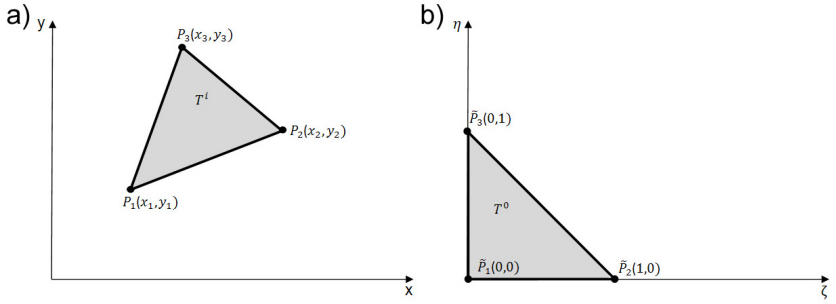

Fig. 4.4: a) General triangle T^i before transformation.
b) Unit triangle T^0 after transformation.

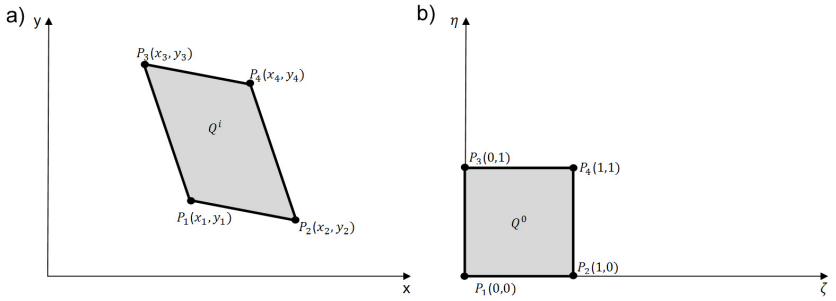

Fig. 4.5: a) General parallelogram Q^i before transformation.
b) Unit quadrate Q^0 after transformation.

A general triangle T^i with corners P_1 to P_3 numbered counterclockwise is transformed by

$$\begin{aligned} x &= x_1 + (x_2 - x_1)\xi + (x_3 - x_1)\eta, \\ y &= y_1 + (y_2 - y_1)\xi + (y_3 - y_1)\eta \end{aligned} \tag{4.27}$$

into a unit triangle T^0, as illustrated in Fig. 4.4. With the help of the ansatz

$$f(\xi, \eta) = \alpha_1 + \alpha_2\xi + \alpha_3\eta \tag{4.28}$$

the transformation (4.27) can be determined. This requires that the coordinates of the vertices

$$\begin{aligned} P_1 &= f(0,0) = \alpha_1, \\ P_2 &= f(1,0) = \alpha_1 + \alpha_2, \\ P_3 &= f(0,1) = \alpha_1 + \alpha_3 \end{aligned} \tag{4.29}$$

are used. From which

$$\begin{aligned} \alpha_1 &= P_1, \\ \alpha_2 &= P_2 - \alpha_1 = P_2 - P_1, \\ \alpha_3 &= P_3 - \alpha_1 = P_3 - P_1 \end{aligned} \tag{4.30}$$

follows. Substituting Eq. (4.30) into Eq. (4.28) yields Eq. (4.27). To calculate the coefficient for the transformation of the parallelogram (4.28), it is advantageous to choose the same numbering as for the triangle (Fig. 4.5), since then the transformation (4.27) is also valid for the unit quadrate. With the transformation (4.27), the complex integrals over the different elements are converted to an integral over a standard region. The integration variables dx and dy must to be transformed with the help of the Jacobian

$$J = \begin{vmatrix} \frac{\partial x}{\partial \xi} & \frac{\partial y}{\partial \xi} \\ \frac{\partial x}{\partial \eta} & \frac{\partial y}{\partial \eta} \end{vmatrix} \tag{4.31}$$

by $dxdy = Jd\xi\, d\eta$. Inserting (4.27) in (4.31) results in

$$J = (x_2 - x_1)(y_3 - y_1) - (x_3 - x_1)(y_2 - y_1). \tag{4.32}$$

By using the chain rule, the partial derivatives

$$\begin{aligned} u_x(x,y,t) &= u_\xi(x(\xi,\eta), y(\xi,\eta), t)\xi_x + u_\eta(x(\xi,\eta), y(\xi,\eta), t)\eta_x \\ u_y(x,y,t) &= u_\xi(x(\xi,\eta), y(\xi,\eta), t)\xi_y + u_\eta(x(\xi,\eta), y(\xi,\eta), t)\eta_y \end{aligned} \tag{4.33}$$

of the integral (4.26) are determined. If now the functions (4.27) are derivated with aspect to x and y, respectively, the relations

$$\begin{aligned} 1 &= (x_2 - x_1)\xi_x + (x_3 - x_1)\eta_x, \\ 0 &= (y_2 - y_1)\xi_x + (y_3 - y_1)\eta_x, \\ 0 &= (x_2 - x_1)\xi_y + (x_3 - x_1)\eta_y, \\ 1 &= (y_2 - y_1)\xi_y + (y_3 - y_1)\eta_y, \end{aligned} \tag{4.34}$$

are obtained, from which we get

$$\xi_x = \frac{1}{(x_2 - x_1) - \frac{(x_3 - x_1)(y_2 - y_1)}{(y_3 - y_1)}} = \frac{y_3 - y_1}{J}, \tag{4.35}$$

$$\eta_x = \frac{1}{-\frac{(x_2 - x_1)(y_3 - y_1)}{y_2 - y_1} + (x_3 - x_1)} = -\frac{(y_2 - y_1)}{J}, \tag{4.36}$$

$$\xi_y = \frac{1}{(y_2 - y_1) - \frac{(y_3 - y_1)(x_2 - x_1)}{(x_3 - x_1)}} = \frac{x_3 - x_1}{J}, \tag{4.37}$$

$$\eta_y = \frac{1}{-\frac{(y_2 - y_1)(x_3 - x_1)}{x_2 - x_1} + (y_3 - y_1)} = -\frac{(x_2 - x_1)}{J}. \tag{4.38}$$

With this result we can now transform the integrals (4.24)-(4.26) into integrals over the standard elements:

$$\iint_{G^i} u(x, y, t)\, dxdy = \iint_{G^0} u(x(\xi, \eta), y(\xi, \eta), t)\; J\; d\xi d\eta \tag{4.39}$$

$$\iint_{G^i} u^2(x, y, t)\, dxdy = \iint_{G^0} u^2(x(\xi, \eta), y(\xi, \eta), t)\; J\; d\xi d\eta \tag{4.40}$$

$$\begin{aligned}
&\iint_{G^i} \left[\frac{\partial u(x, y, t)}{\partial x}\right]^2 + \left[\frac{\partial u(x, y, t)}{\partial y}\right]^2 \, dxdy = \\
&\quad \iint_{G^0} \left\{[u_\xi(x(\xi, \eta), y(\xi, \eta), t)\xi_x + u_\eta(x(\xi, \eta), y(\xi, \eta), t)\eta_x]^2 \right. \\
&\quad \left. + [u_\xi(x(\xi, \eta), y(\xi, \eta), t)\xi_y + u_\eta(x(\xi, \eta), y(\xi, \eta), t)\eta_y]^2 \right\}\; J\; d\xi d\eta \\
&= \frac{(x_3 - x_1)^2 + (y_3 - y_1)^2}{J} \iint_{G^0} \left[\frac{\partial u(x(\xi, \eta), y(\xi, \eta), t)}{\partial \xi}\right]^2 \, d\xi d\eta \\
&\quad + 2\frac{(x_3 - x_1)(x_2 - x_1) + (y_3 - y_1)(y_2 - y_1)}{J} \\
&\quad \times \iint_{G^0} u_\xi(x(\xi, \eta), y(\xi, \eta), t) u_\eta(x(\xi, \eta), y(\xi, \eta), t)\, d\xi d\eta \\
&\quad + \frac{(x_2 - x_1)^2 + (y_2 - y_1)^2}{J} \iint_{G^0} \left[\frac{\partial u(x(\xi, \eta), y(\xi, \eta), t)}{\partial \eta}\right]^2 \, d\xi d\eta.
\end{aligned} \tag{4.41}$$

Having normalized elements, we can think about the basis functions $l_k^0(x, y)$ for $k = 1, 2, \ldots, m$.

4.2.2 Choice of the Basis Functions

Basis functions should be very flexible and, from the mathematical point of view, not unnecessarily complicated. Polynomials satisfy these requirements and are particularly suitable as basis functions. For example polynomials of the form

$$h(x, y) = c_1 + c_2 x + c_3 y + c_4 xy + c_5 x^2 y + c_6 xy^2 + c_7 x^2 + c_8 y^2 + c_9 x^2 y^2 \tag{4.42}$$

could be used. Also, an approach of the form

$$g(x, y) = c_1 + c_2x + c_3y + c_4xy + c_5x^2 + c_6y^2 \tag{4.43}$$

can be used. The choice of the polynomials depends, of course, on the geometry of the underlying elements. Also the nature of the given problem affects the choice of the polynomials. The basis functions need to be continuous in transition from one element to another in order to correctly describe the whole area. Elements with such basis functions are called conform. For the derivatives of the basis functions, the continuity in the transition is generally not necessary. The practice shows often that very good results can also be achieved with non-conform elements. Non-conform elements are often used where the continuity requirements lead to a very large computational effort. However, the use of non-conform elements should be avoided as far as possible. It also proves to be a useful approach when all powers up to a certain degree occur in the polynomial (4.42), or the polynomial is chosen at least symmetrically as in (4.43). Such approaches are called geometrically isotropic, which means that their shape remains unchanged under a linear coordinate transformation.

In a polynomial like (4.42) the coefficients c_i should not be mixed up with the coefficients $c_k(t)$ in Eq. (4.2). In order to determine these coefficients we fix the values of the polynomial at certain points P_i, the so-called node points. Also derivatives at these points of the polynomial could be used to determine the coefficients. They are needed especially if also the derivatives should be continuous. This means, for example, for a polynomial like (4.42) with six coefficients that we have to define exactly six node points, if we do not consider the derivatives of the polynomial. With continuous derivatives we would have to define three node points. In this thesis we do not consider basis functions with continuous derivatives. Therefore, we expect the same number of node points per element as coefficients in the polynomial occur.

Node points must exist at all edges. The positions of the remaining node points can be freely chosen. In the method of weighted residuals, the linear independence of the functions $\varphi_k(x, x)$ for $k = 1, 2, \ldots, m$ is required. To ensure this linear independence we demand

$$\varphi_i(x_j, y_j) = \begin{cases} 0 & \text{for } j \neq i \\ 1 & \text{for } j = i \end{cases} \tag{4.44}$$

with $i = 1, 2, \ldots, m$, $j = 1, 2, \ldots, m$ and m is now the number of all node points in the hole domain G. Here, x_j denotes the x coordinate and y_j the y coordinate of the node point P_j. In addition to this global numbering of the node points one often defines a local numbering, see Fig. 4.6, of these node points within a unit element. The mathematical handling is then more convenient. As example, we consider a one-dimensional domain G with elements consisting of two node points. In this simple case we get due to Eq. (4.44) and Eq. (4.23) for the first global basis function $\varphi_1(x), x \in G$ at node point one

$$\varphi_1(x_1) = l_1^1(x_1) = 1. \tag{4.45}$$

At all other node points, $\varphi_1(x_j)$ is zero. For the first global basis functions, we can write

$$\varphi_1(x) = \begin{cases} l_1^1(x), & P_1 \leq x \leq P_2 \\ 0, & P_2 \leq x \leq P_m \end{cases} . \tag{4.46}$$

For the second basis function at node point two we get due to Eq. (4.44) and Eq. (4.23)

$$\varphi_2(x_2) = l_2^1(x_2) = l_2^2(x_2) = 1. \tag{4.47}$$

At all other node points $\varphi_2(x_j)$ is zero. The second global basis function is now given by

$$\varphi_2(x) = \begin{cases} l_2^1(x), & P_1 \leq x \leq P_2 \\ l_2^2(x), & P_2 \leq x \leq P_3 \\ 0, & P_3 \leq x \leq P_m \end{cases} . \tag{4.48}$$

For the third global basis function at node point three we get

$$\varphi_3(x_3) = l_3^2(x_3) = l_3^3(x_3) = 1. \tag{4.49}$$

At all other node points $\varphi_3(x_j)$ is zero. Hence, the third global basis function is given by

$$\varphi_3(x) = \begin{cases} 0, & P_1 \leq x \leq P_2 \\ l_3^2(x), & P_2 \leq x \leq P_3 \\ l_3^3(x), & P_3 \leq x \leq P_4 \\ 0, & P_4 \leq x \leq P_m \end{cases} . \tag{4.50}$$

The remaining global functions $\varphi_k(x)$ are constructed in an analogous way. Figure 4.7 shows how the global basis functions $\varphi_k(x)$ are composed of the local basis functions $l_k^e(x)$ in this example. One can see form Fig. 4.7 that per element, except the first and last one, only two local basis functions are different form zero. In general, there are as many local basis functions different from zero as node points in an element exist. We now assume that each element is transformed into a unit element and, therefore, the local basis functions of all normalized elements must be identical. This mean for our example that if all elements are transformed into unit elements, there are only two different normalized local basis functions, see Fig. 4.8. Due to the fact that the number of normalized local basis functions and the number of node points per unit element is equal, we use the same local numbering for the normalized local basis functions as for the local node numbering, see Fig 4.8. For the final construction of the normalized local basis functions we must distinguish between different unit elements which is done in the next section.

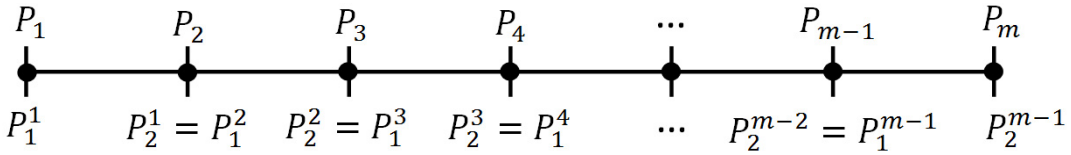

Fig. 4.6: Global and local node numbering.

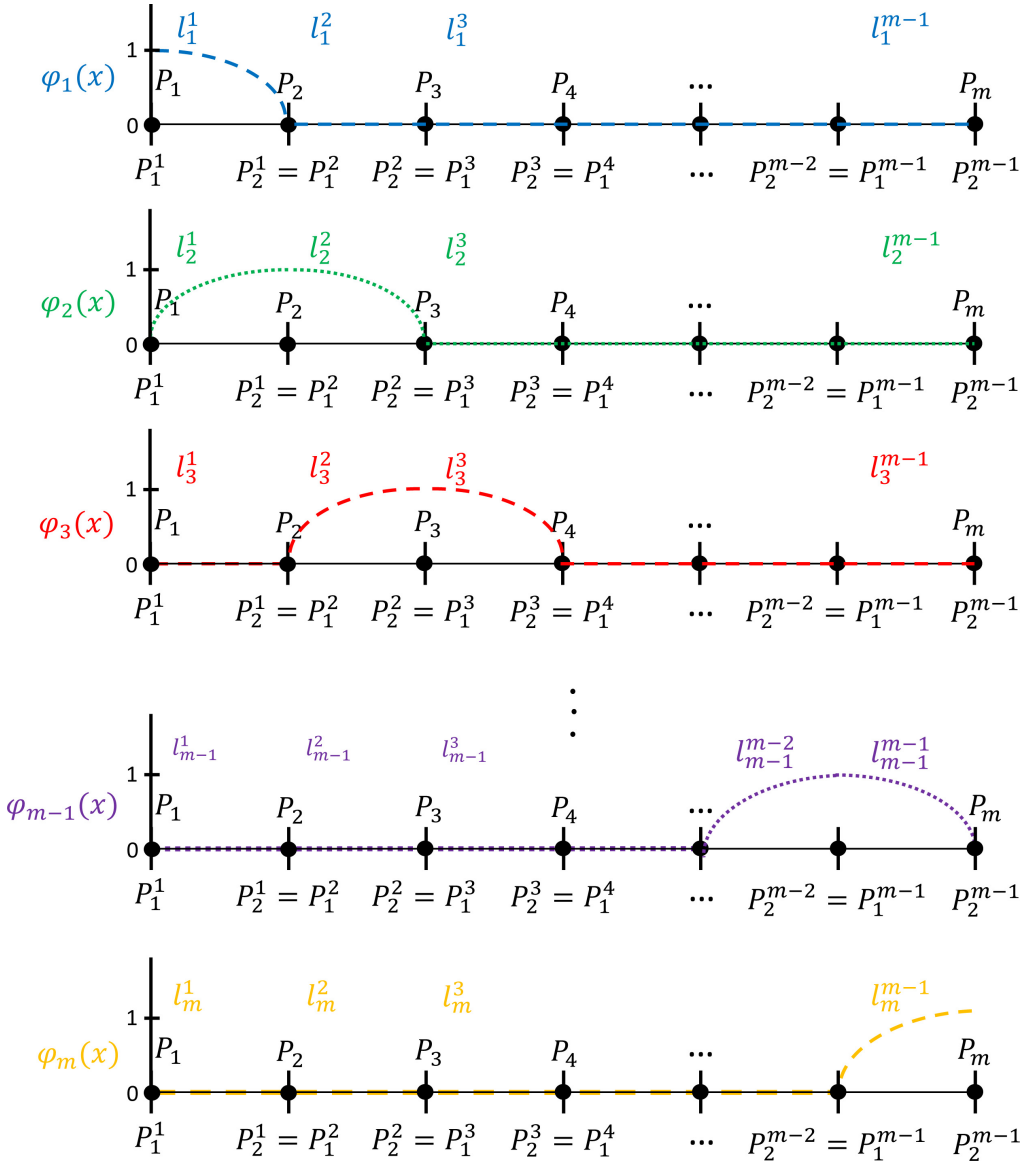

Fig. 4.7: Global basis functions $\varphi_k(x)$ with corresponding local basis functions $l_k^e(x)$.

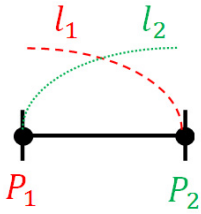

Fig. 4.8: Unit element with corresponding normalized local basis functions.

4.3 Constructing Normalized Local Basis Functions

This section describes a process to construct normalized local basis functions depending on the required element. For a more detailed description of the various elements and its possible basis functions, the reader is referred to [20]. The starting point is the general condition (4.44). This ensures that each basis function $l_i(x, y)$ vanishes at the nodes except one. We also want to achieve a good approximation of the function $u(x, y)$ with the basis functions $l_i(x, y)$. Since the number of node points per element and thus the number of coefficients is variable, we need to specify this parameter. Very good interpolation methods based on polynomials already exist. As an approach for our basis functions, we select the Lagrange interpolation polynomials. [21] In order to proceed, we have to define the dimension of the elements.

4.3.1 One-dimensional Unit Elements

The Lagrange interpolation polynomials of order k are defined by

$$l_j(x) = \prod_{i=1; i\neq j}^{k+1} \frac{x - x_i}{x_j - x_i}, \tag{4.51}$$

$x \in G^0, j = 1, 2, \ldots, k+1$ and $k+1$ is the number of the node points per unit element. These polynomials are especially suitable, because they fulfill the condition (4.44). This follows immediately from the fact that if x is equal to x_j the numerators and the denominators are identical and we get $l_j(x_j) = 1$. On the other hand, if $x = x_i$ one of the numerators are always zero and due to the fact that $i \neq j$ the denominator can not become zero. Thus we get $l_j(x_i) = 0$ and (4.44) is fulfilled. To proceed we have to define the coordinates of the node points.

$$\begin{aligned} x_1 &= -1, \\ x_2 &= 1 \end{aligned} \tag{4.52}$$

of the unit element, see Fig 4.9. If linear basis functions, $k = 1$, are used on a unit element, one speaks from linear elements, if quadratic basis functions, $k = 2$, are used, one speaks from quadratic elements.

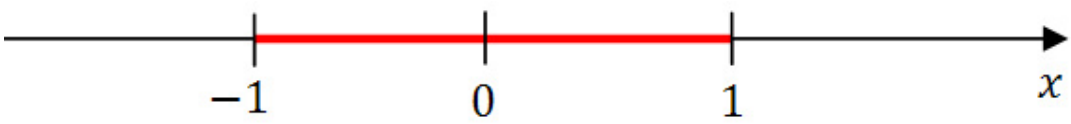

Fig. 4.9: 1D unit element.

4.3.1.1 Linear Elements

Linear elements have two nodes, which means $k = 1$. The choice of the node points

$$\begin{aligned} x_1 &= -1, \\ x_2 &= 1 \end{aligned} \tag{4.53}$$

at the boundaries of the unit element ensures the continuity between adjacent unit elements. For linear elements the normalized local basis functions

$$\begin{aligned} l_1(x) &= \frac{1}{2}(1-x), \\ l_2(x) &= \frac{1}{2}(1+x) \end{aligned} \tag{4.54}$$

are obtained by inserting the node points (4.53) into (4.51). To test if these basic functions meet the condition (4.44) we insert the node points into the basis functions,

$$\begin{aligned} l_1(x_1) &= \frac{1}{2}(1-x_1) = \frac{1}{2}(1-(-1)) = 1, \\ l_1(x_2) &= \frac{1}{2}(1-x_2) = \frac{1}{2}(1-1) = 0, \\ l_2(x_1) &= \frac{1}{2}(1+x_1) = \frac{1}{2}(1-1) = 0, \\ l_2(x_2) &= \frac{1}{2}(1+x_2) = \frac{1}{2}(1+1) = 1, \end{aligned} \tag{4.55}$$

which immediately reveals the solution is correct. Fig. 4.10 shows a one-dimensional linear Lagrange element with corresponding basis functions.

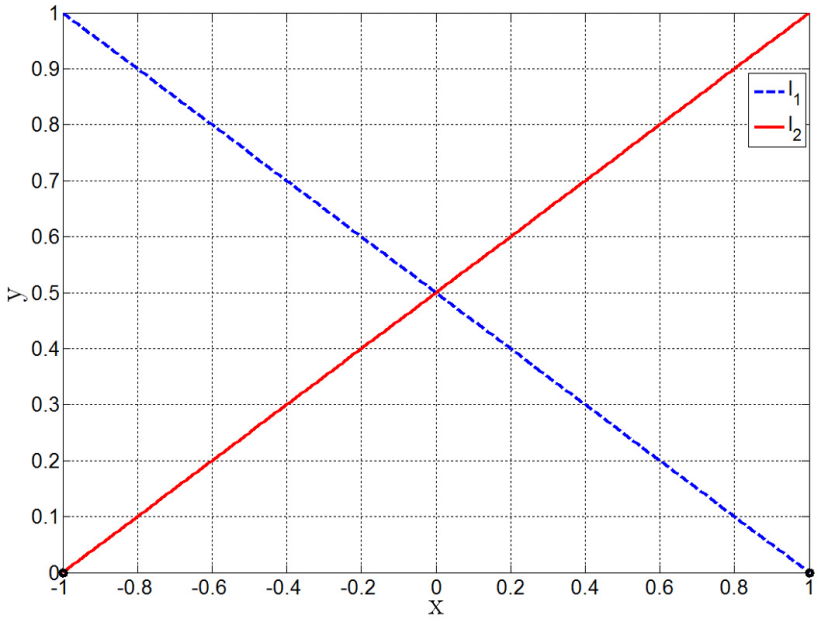

Fig. 4.10: One-dimensional linear Lagrange element with corresponding local basic functions.

4.3.1.2 Quadratic Elements

A quadratic Lagrange element, k=2, requires an additional node. It is possible to choose freely the position of the additional node in the following way:

$$\begin{aligned} x_1 &= -1, \\ x_2 &= 0, \\ x_3 &= 1. \end{aligned} \tag{4.56}$$

According to (4.51), one obtains the local basis functions

$$\begin{aligned} l_1(x) &= \frac{1}{2}(x^2 - x), \\ l_2(x) &= 1 - x^2, \\ l_3(x) &= \frac{1}{2}(x^2 + x). \end{aligned} \tag{4.57}$$

It can be easily shown that these basis functions meet condition (4.44). Figure. 4.11 displays a one-dimensional quadratic Lagrange element with the corresponding local basis functions.

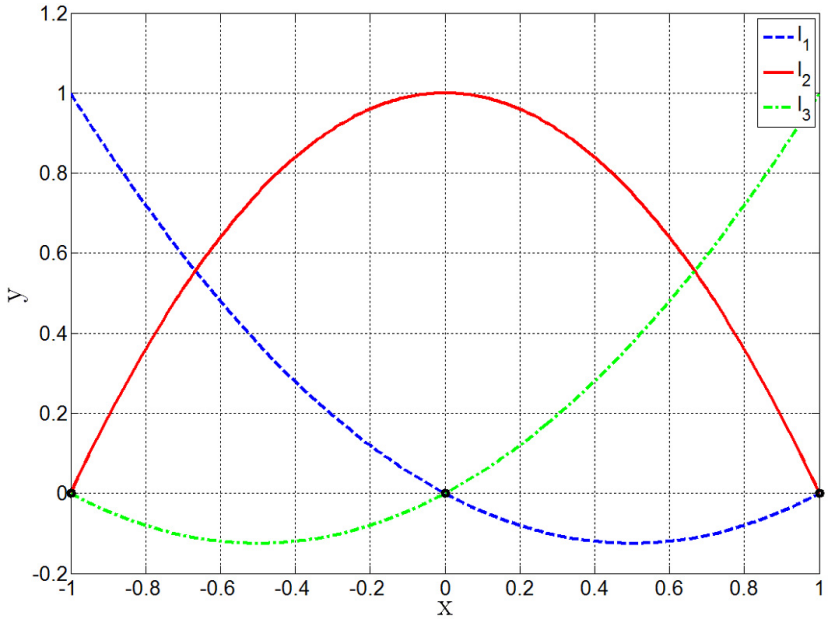

Fig. 4.11: One-dimensional quadratic Lagrange element with the corresponding local basis functions.

4.3.2 Two-dimensional Quadrangle Elements

Two-dimensional quadratic Lagrange quadrangle elements are formed due to the linear independence of the functions l_1,l_2 and l_3 in the following way:

$$\begin{aligned}
g_1(x,y) &= l_1(x)l_1(y),\\
g_2(x,y) &= l_1(x)l_2(y),\\
g_3(x,y) &= l_1(x)l_3(y),\\
g_4(x,y) &= l_2(x)l_1(y),\\
g_5(x,y) &= l_2(x)l_2(y),\\
g_6(x,y) &= l_2(x)l_3(y),\\
g_7(x,y) &= l_3(x)l_1(y),\\
g_8(x,y) &= l_3(x)l_2(y),\\
g_9(x,y) &= l_3(x)l_3(y).
\end{aligned} \tag{4.58}$$

For two-dimensional quadratic Lagrange quadrangle elements we, therefore obtain

$$\begin{aligned}
g_1(x,y) &= \frac{1}{4}(x^2-x)(y^2-y),\\
g_2(x,y) &= \frac{1}{2}(x^2-x)(1-y^2),\\
g_3(x,y) &= \frac{1}{4}(x^2-x)(y^2+y),\\
g_4(x,y) &= \frac{1}{2}(1-x^2)(y^2-y),\\
g_5(x,y) &= (1-x^2)(1-y^2),\\
g_6(x,y) &= \frac{1}{2}(1-x^2)(y^2+y),\\
g_7(x,y) &= \frac{1}{4}(x^2+x)(y^2-y),\\
g_8(x,y) &= \frac{1}{2}(x^2+x)(1-y^2),\\
g_9(x,y) &= \frac{1}{4}(x^2+x)(y^2+y)
\end{aligned} \tag{4.59}$$

as basic functions. The position of the nodes

$$\begin{aligned}
x_1 &= -1 & y_1 &= -1,\\
x_2 &= -1 & y_2 &= 0,\\
x_3 &= -1 & y_3 &= 1,\\
x_4 &= 0 & y_4 &= -1,\\
x_5 &= 0 & y_5 &= 0,\\
x_6 &= 0 & y_6 &= 1,\\
x_7 &= 1 & y_7 &= -1,\\
x_8 &= 1 & y_8 &= 0,\\
x_9 &= 1 & y_9 &= 1
\end{aligned} \tag{4.60}$$

results from the combination of the positions of the nodes in the 1D product formation. Here, x_i means the x position and y_i the y position of the node point P_i. In Fig. 4.12 such a quadratic Lagrange element with the corresponding nodes is shown. The numbering of the nodes is a result of the arbitrary order in the product formation. One can choose it in an arbitrary way. The normalized local basic functions of this element shows Fig. 4.13.

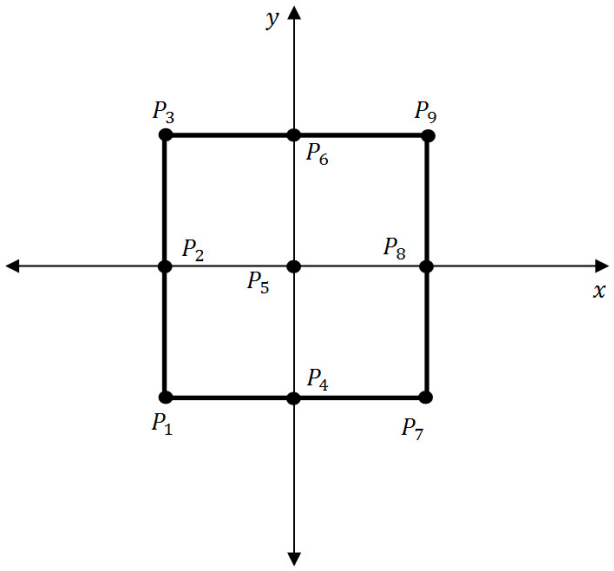

Fig. 4.12: Nodes P_1 to P_9 of a 2D normalized quadratic Lagrange quadrangle element.

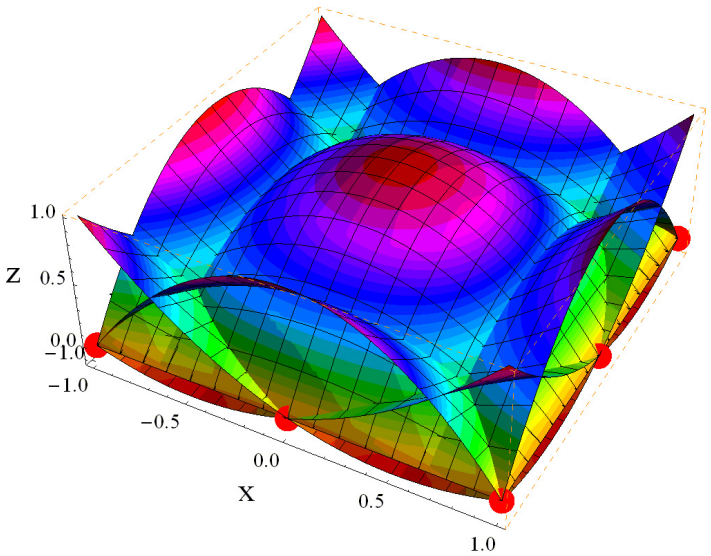

Fig. 4.13: Two-dimensional normalized local basic functions of a quadratic Lagrange quadrangle element.

By forming the product of one-dimensional elements not all two-dimensional elements can be generated. The basis functions of triangular elements can not be obtained by the product of one-dimensional basis functions. There exists, however, an elegant way how such basic functions, corresponding to the nodes, can be easily determined. With the help of Pascal's triangle [22], shown in Fig. 4.14, both the position of the nodes and the local basis functions $l_i(x, y)$ can be obtained. The first level of the Pascal's triangle corresponds to $k = 0$ in (4.51), the second one to $k = 1$ and so on.

To determine the nodes of the triangles, we associate the outer boundaries of the corresponding Pascal's triangle, beginning from the required order, to a closed triangle, as shown in Fig. 4.14 (red dashed line). The terms $1, x, x^2, \ldots$ represent the nodes along the border of the triangle. The corresponding polynomial consists of all involved terms. To get an element for a quadrangle of the same order, we simply reflect the triangle element downwards, Fig. 4.14 (green dashed line). Again connected terms represent the nodes along the border of the quadrangle. Internal terms represent inner nodes.

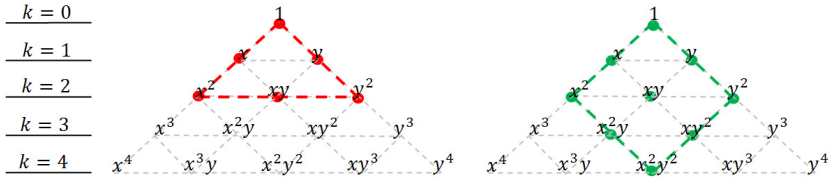

Fig. 4.14: Pascal's triangle to determine the node positions and the polynomial for Lagrange triangle and Lagrange quadrangle elements.

For our quadratic quadrangle element, we get the relative position of the 9 node points from Pascal's triangle. We establish, therefore, the following 9 local basis functions

$$l_i(x, y) = c_1^i + c_2^i x + c_3^i y + c_4^i x^2 + c_5^i xy + c_6^i y^2 + c_7^i x^2 y + c_8^i xy^2 + c_9^i x^2 y^2, \quad i = 1, \ldots, 9. \tag{4.61}$$

We have 81 different coefficients c_j^i for the nine basis functions. In contrast to (4.51), the coefficients of the polynomials, obtained from Pascal's triangle, are not yet determined. To evaluate the coefficients, the absolute position and the numbering of the nodes has to be fixed. The coordinates and the numbering of the nodes of the quadrangular elements are defined in Fig. 4.15.

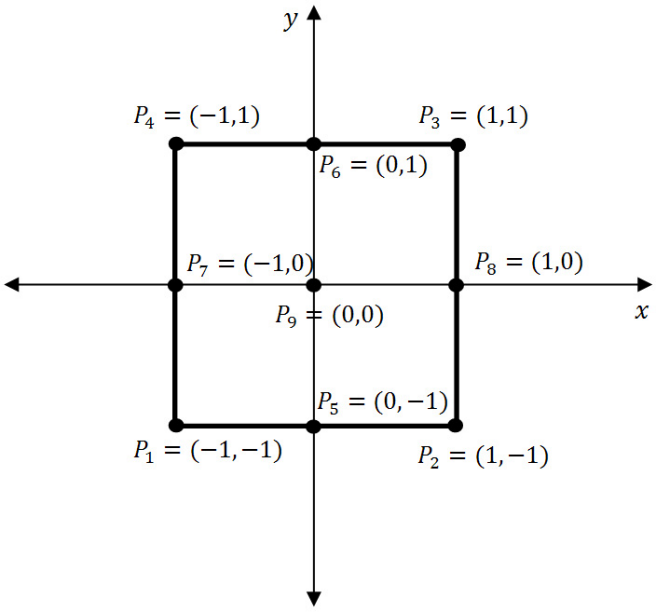

Fig. 4.15: Normalized quadrangular element with nodes P_1 to P_9.

Due to the numbering in Fig 4.15, the coordinates of the nodes are

$$\begin{array}{llll} x_1 = & -1 & y_1 = & -1, \\ x_2 = & 1 & y_2 = & -1, \\ x_3 = & 1 & y_3 = & 1, \\ x_4 = & -1 & y_4 = & 1, \\ x_5 = & 0 & y_5 = & -1, \\ x_6 = & 0 & y_6 = & 1, \\ x_7 = & -1 & y_7 = & 0, \\ x_8 = & 1 & y_8 = & 0, \\ x_9 = & 0 & y_9 = & 0, \end{array} \tag{4.62}$$

where x_i denotes the x position of the node point P_i and y_i the y position. Once the position of the nodes is determined, we obtain, based on Eq. (4.44), for each local basis

function l_i, $i = 1, 2, \ldots, 9$, defined by Eq. (4.61), a system of equations:

$$
\begin{aligned}
l_1(x_1, y_1) &= c_1^1 + c_2^1 x_1 + c_3^1 y_1 + c_4^1 x_1^2 + c_5^1 x_1 y_1 + \ldots = 1, \\
l_1(x_2, y_2) &= c_1^1 + c_2^1 x_2 + c_3^1 y_2 + c_4^1 x_2^2 + c_5^1 x_2 y_2 + \ldots = 0, \\
&\vdots \\
l_1(x_9, y_9) &= c_1^1 + c_2^1 x_9 + c_3^1 y_9 + c_4^1 x_9^2 + c_5^1 x_9 y_9 + \ldots = 0,
\end{aligned}
$$

$$
\begin{aligned}
l_2(x_1, y_1) &= c_1^2 + c_2^2 x_1 + c_3^2 y_1 + c_4^2 x_1^2 + c_5^2 x_1 y_1 + \ldots = 0, \\
l_2(x_2, y_2) &= c_1^2 + c_2^2 x_2 + c_3^2 y_2 + c_4^2 x_2^2 + c_5^2 x_2 y_2 + \ldots = 1, \\
l_2(x_3, y_3) &= c_1^2 + c_2^2 x_3 + c_3^2 y_3 + c_4^2 x_3^2 + c_5^2 x_3 y_3 + \ldots = 0, \\
&\vdots \\
l_2(x_9, y_9) &= c_1^2 + c_2^2 x_9 + c_3^2 y_9 + c_4^2 x_9^2 + c_5^2 x_9 y_9 + \ldots = 0,
\end{aligned}
$$

$$\vdots$$

$$
\begin{aligned}
l_9(x_1, y_1) &= c_1^9 + c_2^9 x_1 + c_3^9 y_1 + c_4^9 x_1^2 + c_5^9 x_1 y_1 + \ldots = 0, \\
&\vdots \\
l_9(x_8, y_8) &= c_1^9 + c_2^9 x_8 + c_3^9 y_8 + c_4^9 x_8^2 + c_5^9 x_8 y_8 + \ldots = 0, \\
l_9(x_9, y_9) &= c_1^9 + c_2^9 x_9 + c_3^9 y_9 + c_4^9 x_9^2 + c_5^9 x_9 y_9 + \ldots = 1.
\end{aligned}
\tag{4.63}
$$

which can be written in a compact matrix form for $i = 1, 2, \ldots, 9$:

$$
\begin{pmatrix}
1 & x_1 & y_1 & x_1^2 & x_1 y_1 & y_1^2 & y_1^2 y_1 & x_1 y_1^2 & x_1^2 y_1^2 \\
1 & x_2 & y_2 & x_2^2 & x_2 y_2 & y_2^2 & y_2^2 y_2 & x_2 y_2^2 & x_2^2 y_2^2 \\
1 & x_3 & y_3 & x_3^2 & x_3 y_3 & y_3^2 & y_3^2 y_3 & x_3 y_3^2 & x_3^2 y_3^2 \\
1 & x_4 & y_4 & x_4^2 & x_4 y_4 & y_4^2 & y_4^2 y_4 & x_4 y_4^2 & x_4^2 y_4^2 \\
1 & x_5 & y_5 & x_5^2 & x_5 y_5 & y_5^2 & y_5^2 y_5 & x_5 y_5^2 & x_5^2 y_5^2 \\
1 & x_6 & y_6 & x_6^2 & x_6 y_6 & y_6^2 & y_6^2 y_6 & x_6 y_6^2 & x_6^2 y_6^2 \\
1 & x_7 & y_7 & x_7^2 & x_7 y_7 & y_7^2 & y_7^2 y_7 & x_7 y_7^2 & x_7^2 y_7^2 \\
1 & x_8 & y_8 & x_8^2 & x_8 y_8 & y_8^2 & y_8^2 y_8 & x_8 y_8^2 & x_8^2 y_8^2 \\
1 & x_9 & y_9 & x_9^2 & x_9 y_9 & y_9^2 & y_9^2 y_9 & x_9 y_9^2 & x_9^2 y_9^2
\end{pmatrix}
\begin{pmatrix} c_1^i \\ c_2^i \\ c_3^i \\ c_4^i \\ c_5^i \\ c_6^i \\ c_7^i \\ c_8^i \\ c_9^i \end{pmatrix}
=
\begin{pmatrix} \delta_{i1} \\ \delta_{i2} \\ \delta_{i3} \\ \delta_{i4} \\ \delta_{i5} \\ \delta_{i6} \\ \delta_{i7} \\ \delta_{i8} \\ \delta_{i9} \end{pmatrix}
\tag{4.64}
$$

For the coefficients of the basis functions we obtain

$$
\begin{array}{lllllllll}
c_1^1 = 0 & c_2^1 = 0 & c_3^1 = 0 & c_4^1 = 0 & c_5^1 = \frac{1}{4} & c_6^1 = 0 & c_7^1 = -\frac{1}{4} & c_8^1 = -\frac{1}{4} & c_9^1 = \frac{1}{4} \\
c_1^2 = 0 & c_2^2 = 0 & c_3^2 = 0 & c_4^2 = 0 & c_5^2 = -\frac{1}{4} & c_6^2 = 0 & c_7^2 = -\frac{1}{4} & c_8^2 = \frac{1}{4} & c_9^2 = \frac{1}{4} \\
c_1^3 = 0 & c_2^3 = 0 & c_3^3 = 0 & c_4^3 = 0 & c_5^3 = \frac{1}{4} & c_6^3 = 0 & c_7^3 = \frac{1}{4} & c_8^3 = \frac{1}{4} & c_9^3 = \frac{1}{4} \\
c_1^4 = 0 & c_2^4 = 0 & c_3^4 = 0 & c_4^4 = 0 & c_5^4 = -\frac{1}{4} & c_6^4 = 0 & c_7^4 = \frac{1}{4} & c_8^4 = -\frac{1}{4} & c_9^4 = \frac{1}{4} \\
c_1^5 = 0 & c_2^5 = 0 & c_3^5 = -\frac{1}{2} & c_4^5 = 0 & c_5^5 = 0 & c_6^5 = \frac{1}{2} & c_7^5 = \frac{1}{2} & c_8^5 = 0 & c_9^5 = -\frac{1}{2} \\
c_1^6 = 0 & c_2^6 = 0 & c_3^6 = \frac{1}{2} & c_4^6 = 0 & c_5^6 = 0 & c_6^6 = \frac{1}{2} & c_7^6 = -\frac{1}{2} & c_8^6 = 0 & c_9^6 = -\frac{1}{2} \\
c_1^7 = 0 & c_2^7 = -\frac{1}{2} & c_3^7 = 0 & c_4^7 = \frac{1}{2} & c_5^7 = 0 & c_6^7 = 0 & c_7^7 = 0 & c_8^7 = \frac{1}{2} & c_9^7 = -\frac{1}{2} \\
c_1^8 = 0 & c_2^8 = \frac{1}{2} & c_3^8 = 0 & c_4^8 = \frac{1}{2} & c_5^8 = 0 & c_6^8 = 0 & c_7^8 = 0 & c_8^8 = -\frac{1}{2} & c_9^8 = -\frac{1}{2} \\
c_1^9 = 1 & c_2^9 = 0 & c_3^9 = 0 & c_4^9 = -1 & c_5^9 = 0 & c_6^9 = -1 & c_7^9 = 0 & c_8^9 = 0 & c_9^9 = 1
\end{array}
\tag{4.65}
$$

Inserting the coefficients into (4.61) yields the basis functions of a quadratic quadrangle element:

$$
\begin{aligned}
l_1(x,y) &= \frac{1}{4}(x-1)x(y-1)y, \\
l_2(x,y) &= \frac{1}{4}(x+1)x(y-1)y, \\
l_3(x,y) &= \frac{1}{4}(x+1)x(y+1)y, \\
l_4(x,y) &= \frac{1}{4}(x-1)x(y+1)y, \\
l_5(x,y) &= -\frac{1}{2}(x^2-1)(y-1)y, \\
l_6(x,y) &= -\frac{1}{2}(x^2-1)(y+1)y, \\
l_7(x,y) &= -\frac{1}{2}(x-1)x(y^2-1), \\
l_8(x,y) &= -\frac{1}{2}(x+1)x(y^2-1), \\
l_9(x,y) &= (x^2-1)(y^2-1).
\end{aligned}
\tag{4.66}
$$

Due to the construction based on Pascal's triangle again a Lagrange element arises. As can be seen, the result is equivalent to (4.59). For this reason, the elements created with the help of Pascal's triangle are also often called Lagrange elements.

4.3.3 Two-dimensional Triangle Elements

The basis functions of two-dimensional triangle elements can be determined again by Pascal's triangle. The evaluation based on Fig. 4.14 results in six basis functions for a quadratic Lagrange triangle:

$$l_i(x,y) = c_1^i + c_2^i x + c_3^i y + c_4^i x^2 + c_5^i xy + c_6^i y^2, \quad i = 1,\ldots,6. \tag{4.67}$$

The numbers and positions of the nodes for this quadratic triangle are shown in Fig. 4.16.

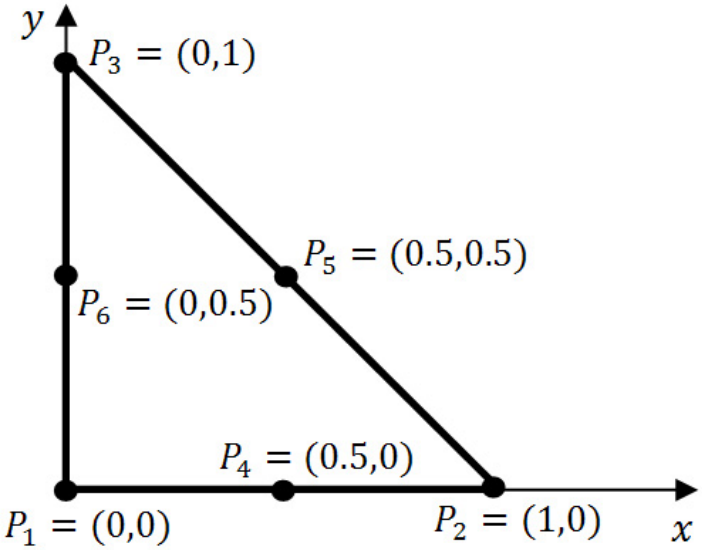

Fig. 4.16: Quadratic Lagrange triangle element with nodes P_1 to P_6.

Setting up the system of equations due to Eq. (4.44) and Eq. (4.67) results in

$$\begin{pmatrix} 1 & x_1 & y_1 & x_1^2 & x_1y_1 & y_1^2 \\ 1 & x_2 & y_2 & x_2^2 & x_2y_2 & y_2^2 \\ 1 & x_3 & y_3 & x_3^2 & x_3y_3 & y_3^2 \\ 1 & x_4 & y_4 & x_4^2 & x_4y_4 & y_4^2 \\ 1 & x_5 & y_5 & x_5^2 & x_5y_5 & y_5^2 \\ 1 & x_6 & y_6 & x_6^2 & x_6y_6 & y_6^2 \end{pmatrix} \begin{pmatrix} c_1^i \\ c_2^i \\ c_3^i \\ c_4^i \\ c_5^i \\ c_6^i \end{pmatrix} = \begin{pmatrix} \delta_{i1} \\ \delta_{i2} \\ \delta_{i3} \\ \delta_{i4} \\ \delta_{i5} \\ \delta_{i6} \end{pmatrix} \tag{4.68}$$

with $i = 1, 2, \ldots, 6$. For the coefficients we obtain

$$\begin{array}{llllll} c_1^1 = 1 & c_2^1 = -3 & c_3^1 = -3 & c_4^1 = 2 & c_5^1 = 4 & c_6^1 = 2 \\ c_1^2 = 0 & c_2^2 = -1 & c_3^2 = 0 & c_4^2 = 2 & c_5^2 = 0 & c_6^2 = 0 \\ c_1^3 = 0 & c_2^3 = 0 & c_3^3 = -1 & c_4^3 = 0 & c_5^3 = 0 & c_6^3 = 2 \\ c_1^4 = 0 & c_2^4 = 4 & c_3^4 = 0 & c_4^4 = -4 & c_5^4 = 4 & c_6^4 = 0 \\ c_1^5 = 0 & c_2^5 = 0 & c_3^5 = 0 & c_4^5 = 0 & c_5^5 = 4 & c_6^5 = 0 \\ c_1^6 = 0 & c_2^6 = 0 & c_3^6 = 4 & c_4^6 = 0 & c_5^6 = -4 & c_6^6 = -4 \end{array} \tag{4.69}$$

Inserting the coefficients into (4.67) yields

$$\begin{aligned} l_1(x, y) &= 2x^2 + 4xy - 3x + 2y^2 - 3y + 1, \\ l_2(x, y) &= 2x^2 - x, \\ l_3(x, y) &= -4x^2 - 4xy + 4x, \\ l_4(x, y) &= -4x^2 - 4xy + 4x, \\ l_5(x, y) &= 4xy, \\ l_6(x, y) &= -4xy - 4y^2 + 4y. \end{aligned} \tag{4.70}$$

In Fig. 4.17, the basis functions of such a quadratic Lagrange triangle element with the corresponding nodes are shown.

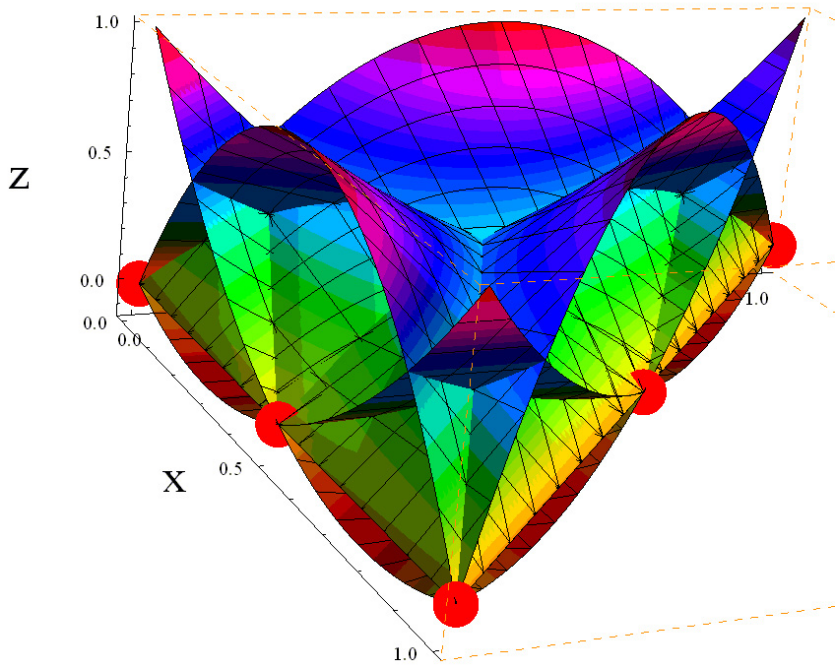

Fig. 4.17: Two-dimensional local basic functions of a quadratic Lagrange triangle element.

Since we have completely defined the basis functions we can now calculate the residual integrals which is done in the next section.

4.4 Calculation of the Residual Integrals

If one uses quadratic Lagrange triangle or quadrangle elements, an analytical calculation of the integrals (4.39) up to (4.41) would be possible. The resulting formulas are usually complex and, therefore, time-intensive in the evaluation. For geometrically more complex elements, such as curvilinear elements, a Gauss-Legendre integration method [23] is often used. This integration method is a variant of the so-called Gaussian quadrature. It is assumed that the elements were already transformed into unit elements in ξ and η. In the one-dimensional case, the integral

$$\int_a^b f(\xi)\, d\xi = \int_a^b \Phi(\xi)\omega(\xi)\, d\xi \approx \int_a^b p(\xi)\omega(\xi)\, d\xi \tag{4.71}$$

over a function $f(\xi)$ is separated into a weight function $\omega(\xi)$ and a remaining function $\Phi(\xi)$. This remaining function is than approximated by a polynomial $p(\xi)$ of the degree n. This integral

$$\int_a^b p(\xi)\omega(\xi)\, d\xi = \sum_{i=1}^{n} p(\xi_i)\omega_i \tag{4.72}$$

can then be converted again into a sum with integration points ξ_i and weights ω_i. Integration points should not be mixed up with the node points P_i in Sec. 4.3. If the function $f(\xi)$ is a polynomial of degree $(2n-1)$ the integration is even accurate. This is of particular importance as the basis functions are polynomials. The minimum number n of integration points is thus directly related to the degree of the polynomials describing the element. The weights

$$\omega_i = \int_a^b \omega(\xi) \prod_{j=1, j\neq i}^{n} \frac{\xi - \xi_j}{\xi_i - \xi j} \, d\xi \tag{4.73}$$

depend on the Interwall $[a, b]$, the weight function $\omega(\xi)$ and on the integration points ξ_i. If we choose the weight function $\omega(\xi) = 1$ and and $a = -1$, $b = 1$ (most popular), then we get the Gauss-Legendre integration. The integration points are then the zeros of the Legendre polynomials. Weights for various elements can also be found in literature [24, 25, 26].

The basis functions of a quadratic element can be created by the product of two one-dimensional basis functions, Eq. (4.58), therefore, we can apply Eq. (4.72) to these one-dimensional functions and obtain

$$\iint_{Q^0} f(\xi)g(\eta) \, d\xi d\eta \approx \sum_{i=1}^{n} \sum_{j=1}^{n} p(\xi_i)q(\eta_j)\hat{\omega}_i\tilde{\omega}_j. \tag{4.74}$$

In the case of triangular elements a similar form results. Ready formulas for determining the integration points with the corresponding weights can be found in [27, 28]. In Fig. 4.18 a possible distribution of integration points for the unit triangle and the unit square is shown. In Tab. 4.1-4.3 the coordinates of integration points and corresponding weights for quadratic elements with 3, 9 and 16 integration points are shown.

Tabelle 4.1: Coordinates of integration points and corresponding weights for quadratic elements with 3 integration points.

point	ξ_i	η_j	$\hat{\omega}_i$	$\tilde{\omega}_j$
1	0,788675	0,788675	0,50	0,50
2	0,788675	0,211325	0,50	0,50
3	0,211325	0,788675	0,50	0,50
4	0,211325	0,211325	0,50	0,50

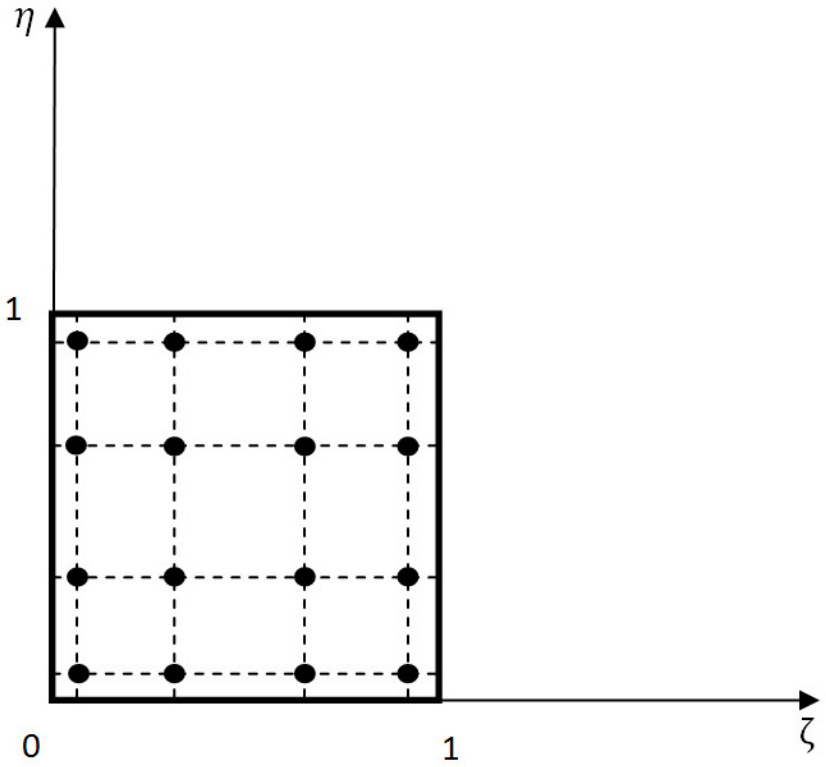

Fig. 4.18: Unit square with 4x4 integration points.

Tabelle 4.2: Coordinates of integration points and corresponding weights for quadratic elements with 9 integration points.

point	ξ_i	η_j	$\hat{\omega}_i$	$\tilde{\omega}_j$
1	0,887295	0,887295	0,277775	0,277775
2	0,887295	0,5	0,277775	0,44444
3	0,887295	0,112705	0,277775	0,277775
4	0,5	0,887295	0,44444	0,277775
5	0,5	0,5	0,44444	0,44444
6	0,5	0,112705	0,44444	0,277775
7	0,112705	0,887295	0,277775	0,277775
8	0,112705	0,5	0,277775	0,44444
9	0,112705	0,112705	0,277775	0,277775

Tabelle 4.3: Coordinates of integration points and corresponding weights for quadratic elements with 16 integration points.

point	ξ_i	η_j	$\hat{\omega}_i$	$\tilde{\omega}_j$
1	0,069435	0,069435	0,17392	0,17392
2	0,069435	0,33001	0,17392	0,32607
3	0,069435	0,930565	0,17392	0,32607
4	0,069435	0,66999	0,17392	0,17392
5	0,33001	0,069435	0,32607	0,17392
6	0,33001	0,33001	0,32607	0,32607
7	0,33001	0,930565	0,32607	0,32607
8	0,33001	0,66999	0,32607	0,17392
9	0,930565	0,069435	0,32607	0,17392
10	0,930565	0,33001	0,32607	0,32607
11	0,930565	0,930565	0,32607	0,32607
12	0,930565	0,66999	0,32607	0,17392
13	0,66999	0,069435	0,17392	0,17392
14	0,66999	0,33001	0,17392	0,32607
15	0,66999	0,930565	0,17392	0,32607
16	0,66999	0,66999	0,17392	0,17392

Now we are in the position to solve the system of differential equations (4.22) which is done in the next section.

4.5 Solving the Differential Equations

First, we transform the system of differential equations (4.22) by defining the matrices

$$\mathbf{A} = (a_{jk}) = \iint_G \text{grad } \varphi_k(x,y) \text{ grad } \varphi_j(x,y)\, dxdy + \int_{C_2} \alpha(s)\varphi_k(\zeta(s))\varphi_j(\zeta(s))\, ds, \tag{4.75}$$

$$\mathbf{B} = (b_{jk}) = \iint_G \varphi_k(x,y)\varphi_j(x,y)\, dxdy \tag{4.76}$$

and the vectors

$$\begin{aligned} \mathbf{c}(t) &= (c_1(t), c_2(t), c_3(t), \ldots, c_m(t))^T, \\ \mathbf{d}(t) &= (d_1(t), d_2(t), d_3(t), \ldots, d_m)^T, \end{aligned} \tag{4.77}$$

with

$$\begin{aligned} d_j(t) = \iint_G \left\{ \text{grad } \varphi_0(x,y,t) \text{ grad } \varphi_j(x,y) + \left[f(x,y,t) + \frac{\partial \varphi_0(x,y,t)}{\partial t} \right] \varphi_j(x,y) \right\} dxdy \\ + \int_{C_2} \left[\alpha(s)\varphi_0(\zeta(s),t) - \gamma_2(s) \right] \varphi_j(\zeta(s))\, ds, \end{aligned} \tag{4.78}$$

into a compact form

$$\mathbf{A}\mathbf{c} + \mathbf{B}\frac{d}{dt}\mathbf{c}(t) + \mathbf{d}(t) = 0. \tag{4.79}$$

Due to the definition of the basis functions (4.23) the integrals over the domain G decay into a sum of integrals over the Elements G^i

$$\mathbf{A} = \sum_{i=1}^{z} \iint_{G^i} \text{grad } l_k^i(x,y) \text{ grad } l_j^i(x,y)\, dxdy + \int_{C_2} \alpha(s)\varphi_k(\zeta(s))\varphi_j(\zeta(s))\, ds, \tag{4.80}$$

$$\mathbf{B} = \sum_{i=1}^{z} \iint_{G^i} l_k^i(x,y) l_j^i(x,y)\, dxdy \tag{4.81}$$

and

$$\begin{aligned} d_j(t) = &\sum_{i=1}^{z} \iint_{G^i} \left\{ \text{grad } \varphi_0(x,y,t) \text{ grad } l_j^i(x,y) + \left[f(x,y,t) + \frac{\partial \varphi_0(x,y,t)}{\partial t} \right] l_j^i(x,y) \right\} dxdy \\ &+ \int_{C_2} \left[\alpha(s)\varphi_0(\zeta(s),t) - \gamma_2(s) \right] \varphi_j(\zeta(s))\, ds. \end{aligned} \tag{4.82}$$

Now we can normalize each Element G^i (see Sec. 4.2.1) and therefore, it is possible to use the integrations method of Sec. 4.4 to calculate the integrals.

The matrices are symmetric. The vector $\mathbf{d}(t)$ depends on t if the boundary conditions depend on t. For the integration of (4.79) an initial condition for the vector $\mathbf{c}(t)$ is required. Due to the definition of (4.19) we choose the ansatz

$$\varphi_0(x,y,0) + \sum_{k=1}^{m} c_k(0)\varphi_k(x,y) = u_0(x,y). \tag{4.83}$$

This condition is generally not fulfilled for all the points in G. Therefore, we apply Galerkin's principle, which results in

$$\sum_{k=1}^{m} c_k(0) \iint_G \varphi_k(x,y)\varphi_j(x,y)\, dxdy + \iint_G \left(\varphi_0(x,y,0) - u_0(x,y) \right) \varphi_j(x,y)\, dxdy = 0 \tag{4.84}$$

for $j = 1, 2, \ldots, m$. The solution of this system of linear algebraic equation yields $c_k(0)$, $k = 1, 2, \ldots, m$.

The system of differential equations (4.79) is linear, allowing a simple numerical integration method. Such a method is the trapezoidal method [29]. First, we transform (4.79) into an explicit form

$$\frac{d}{dt}\mathbf{c}(t) = -\mathbf{B}^{-1}\mathbf{A}\mathbf{c}(t) - \mathbf{B}^{-1}\mathbf{d}(t) \tag{4.85}$$

so that the formal integration step

$$\mathbf{c}_{n+1} = \mathbf{c}_n - \frac{1}{2}\Delta t \left(-\mathbf{B}^{-1}\mathbf{A}\mathbf{c}_n - \mathbf{B}^{-1}\mathbf{d}_n + \mathbf{B}^{-1}\mathbf{A}\mathbf{c}_{n+1} + \mathbf{B}^{-1}\mathbf{d}_{n+1}\right) \tag{4.86}$$

can be executed with the step size Δt at the time $t = n\Delta t$. Then, the equation has to be multiplied with $\mathbf{B}$ and sorted. Finally, we obtain the linear system of algebraic equations

$$\left(\mathbf{B} + \frac{1}{2}\Delta t\mathbf{A}\right)\mathbf{c}_{n+1} = \left(\mathbf{B} + \frac{1}{2}\Delta t\mathbf{A}\right)\mathbf{c}_n + \frac{1}{2}\Delta t\left(\mathbf{d}_n - \mathbf{d}_{n+1}\right) \tag{4.87}$$

with the coefficient matrix $\mathbf{B} + \frac{1}{2}\Delta t\mathbf{A}$.

For complex problems an algorithm which use matrix inversions to solve Eq. (4.87), is generally not the best idea, because the matrices are usually much too large for direct inversion. For this reason, the system of algebraic equations (4.87) is solved approximately by using iterative algorithms. A standard procedure would be, for example, the conjugate gradient method [30]. For the selection of a suitable algorithm, it is important to know that the matrices are generally not filled symmetrically. However, they are filled weakly. This fact allows an intelligent storage of the matrix at the PC, so that the memory needed is minimized for the matrices. Since the RAM memory is much faster than the memory on the hard disk one will always try to store the hole matrices in the RAM. For the size of the matrices, the numbering of the elements and the associated structure plays a major role. The structure of the matrix also affects the convergence speed of the algorithm. An overview of the various options for numbering the elements after discretization, and the various storage methods for sparse matrices can be found in [19]. A very stable and highly efficient algorithm for solving unbalanced sparse linear systems $\mathbf{A}x = \mathbf{b}$ offers the program library UMFPACK by Timothy A. Davis, University of Florida. This library is available under the GNU GPL license. A more detailed description of this process would go beyond the scope of this thesis. For this reason, the reader is referred to the official home page “www.cise.ufl.edu/research/sparse/umfpack/ “.

But even the best algorithm is no guarantee for correct values, because the achieved accuracy depends also on the used mesh. For a stationary solution, this problem is usually solved by using a coarse grid in the first solution process. After that the achieved solution is used to build a finer and better mesh. With the new mesh a new solution can be calculated. If two consecutive solutions no longer differ, the correct stationary solution is found. But if one is interested in the time evolution of the involved particles, checking the achieved accuracy is not so easy anymore. During the time evolution, the particle density can change in the device, which can cause a move of areas with high particle density difference. But this areas need a fine grid. Since one can not know exactly where these areas are during the time evolution, it is necessary to ensure that the entire mesh is fine enough. This problem is dealt with in Sec. 5.

5 Calculation of the Capacity of OTFTs as Accuracy and Stability Test

In order to check the accuracy of the time evolution of the simulated quantities, we design a simple test model that can be verified. Normally, we are interested in the steady state of the device. The time evolution of the variables after switching on is often not evaluated separately. In this thesis the temporal evolution of H^+ ions in a pentacene-based OTFT is required. In order to make correct conclusions, the achieved accuracy of the calculated values during the time evolution is important, a precisely calculated steady state is not sufficient in this case. To calculate the error of the time evolution, an indirect attempt is made. To determine if the mesh size requirements are fulfilled, we calculate a time-independent value (amount of stored charge in the FET) from a time-dependent quantity (in- and out-flowing currents). Then we calculate the same value from a stationary quantity (stationary carrier density). If they match, the mesh should be fine enough.

Starting point is an organic thin film transistor with a structure as shown Fig. 5.1.

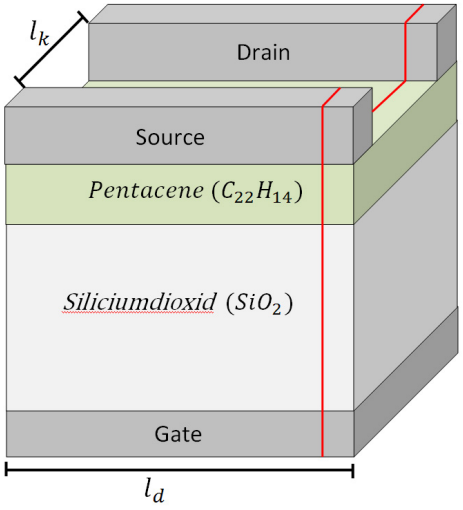

Fig. 5.1: Organic thin-film transistor with the channel length l_k and device length l_d.

To reduce the device to a two-dimensional problem, it is cut along the red line in Fig.

5.1. The resulting cross section is plotted in Fig. 5.2. This structure can be considered as a capacitor as illustrated in Fig. 5.3. The dielectric of the capacitor is pentacene with

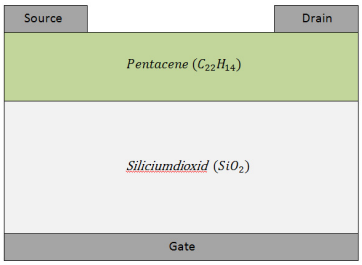

Fig. 5.2: Two-dimensional section through the transistor.

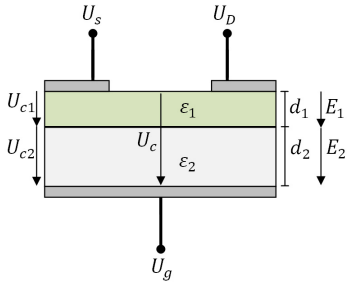

Fig. 5.3: Schematic design of the plate capacitor.

the dielectric constant $\varepsilon_1 = \varepsilon_{r1}\varepsilon_0$ and the silicon dioxide with the dielectric constant $\varepsilon_2 = \varepsilon_{r2}\varepsilon_0$. The dielectric constant of vacuum $\varepsilon_0 = 8.854187 \cdot 10^{-12} AsV^{-1}m^{-1}$.

5.1 Simulation Model

The charge transport in pentacene, based on holes, are described by the drift diffusion equation (3.100) in combination with the Poisson equation (3.126). The Poisson equation is given by

$$\varepsilon_0 \nabla \left[\varepsilon_r(\mathbf{r}) \nabla \phi(\mathbf{r}, t)\right] = -q\, n(\mathbf{r}, t) \tag{5.1}$$

where

$$\varepsilon_r(\mathbf{r}) = \begin{cases} \varepsilon_{r1}(\mathbf{r}) & \text{in pentacene,} \\ \varepsilon_{r2}(\mathbf{r}) & \text{in } SiO_2, \end{cases} \tag{5.2}$$

and

$$n(\mathbf{r}, t) = \begin{cases} n_p(\mathbf{r}, t) & \text{in pentacene,} \\ 0 & \text{in } SiO_2. \end{cases} \tag{5.3}$$

Here n_p is the hole density, $q = 1,602 \cdot 10^{-19}$ the elementary charge and ϕ the electric potential. The drift-diffusion equation which consist of the continuity equation (3.41) and the drift-diffusion current equation (3.98) are given by

$$\frac{\partial}{\partial t} n_p(\mathbf{r}, t) = -\frac{1}{q} \nabla \mathbf{J}_p(\mathbf{r}, t) \tag{5.4}$$

and

$$\mathbf{J}_p(\mathbf{r}, t) = -q\mu_p n_p(\mathbf{r}, t) \nabla\phi(\mathbf{r}, t) - \mu_p k_B T \nabla n_p(\mathbf{r}, t) \tag{5.5}$$

in pentacene, where $\mathbf{J}_p$ is the hole current density, μ_p the hole mobility and $k_B = 1,380 \cdot 10^{-23}$ J/K represents the Boltzmann constant. In Eq. (5.5) we replaced the electric field $\mathbf{E}(\mathbf{r}, t)$ by the electric potential ϕ with the help of Eq. (3.121).

5.2 Numerical Calculation

In order to determine the amount of charge in the channel and, therefore, the capacitance of the FET, the in- and out-flowing currents I_1 and I_2, as shown in Fig. 5.4, are simulated temporally resolved. By integrating the x-component of the current density $\mathbf{J}_p$ along the semiconductor at the channel entrance and exit, the currents

$$I_1(t) = \int_{y=0}^{d_1} \left[q\mu_p n_p(x_1, y, t) E_x(x_1, y, t) - \mu_p k_B T \frac{\partial n_p(x_1, y, t)}{\partial x} \right] dy, \tag{5.6}$$

$$I_2(t) = \int_{y=0}^{d_1} \left[q\mu_p n_p(x_2, y, t) E_x(x_2, y, t) - \mu_p k_B T \frac{\partial n_p(x_2, y, t)}{\partial x} \right] dy \tag{5.7}$$

can be determined. The dash-dotted red line in Fig. 5.4 represents the beginning of the channel at the position x_1 and the end of the channel at the position x_2. The time-integrated difference between the two currents

$$Q = l_d \int_{t=0}^{\infty} \left(I_1(t) - I_2(t) \right) \, dt \tag{5.8}$$

results in the amount of charge stored in the channel. To check the accuracy of Q, we integrate also the resulting stationary carrier density $n_p(x, y)$ in the channel to obtain the total charge

$$Q = l_d \int_{x=0}^{l_k} \int_{y=0}^{d_1} n_p(x, y) \, dxdy. \tag{5.9}$$

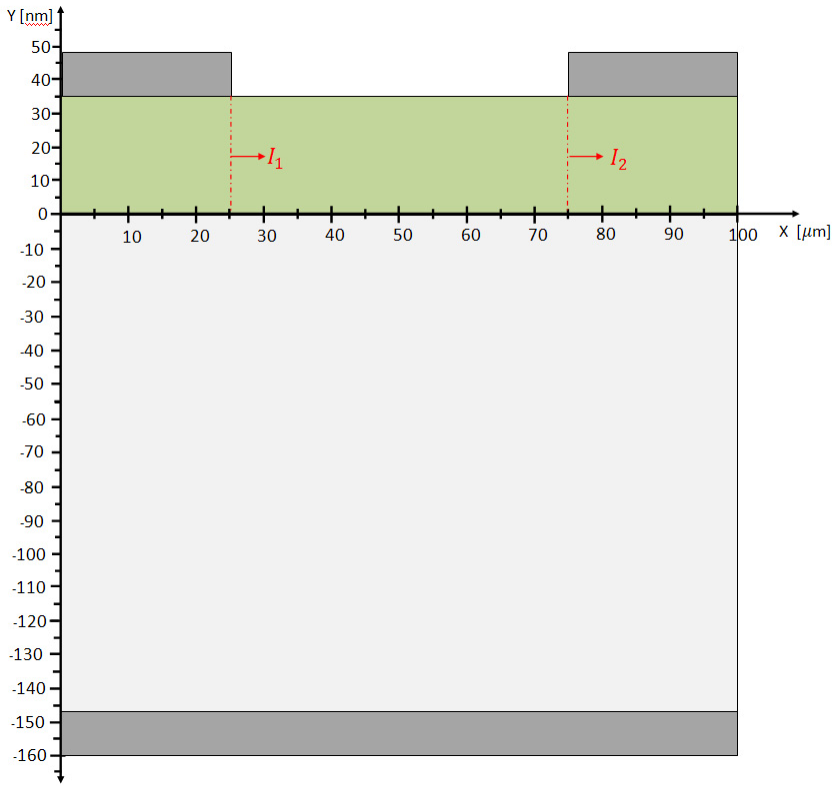

Fig. 5.4: Geometry of the two-dimensional model for the organic thin film transistor.

Boundary conditions: For the numerical simulation boundary conditions must be set in addition to the input parameters (initial conditions). In Fig. 5.5, the device with the appropriate boundary conditions is shown. Source, drain, and gate are at a given potential. Therefore, Dirichlet boundary conditions

$$\begin{aligned} \phi(x,y) &= U_S \quad \text{on } C_s, \\ \phi(x,y) &= U_D \quad \text{on } C_d, \\ \phi(x,y) &= U_G \quad \text{on } C_g \end{aligned} \tag{5.10}$$

are suitable for the potential. At the interface between the organic layer and the source and drain, respectively, we adopt contacts with constant hole density c_{pSD}. [31][32][33]. Assuming an injection barrier $\triangle E$ between the organic layer and gold contacts of 0.47 eV [34]. the particle densities at source and drain are then given by

$$c_{pSD} = c_{pSource} = c_{pDrain} = c_{pi}\, e^{\frac{-q\,\triangle E}{k_B T}}. \tag{5.11}$$

The constants are the temperature $T = 298.15$ K, the elementary charge $q = 1.602 \cdot 10^{-19}$ C and the Boltzmann constant $k_B = 1.38 \cdot 10^{-23}$ J/K. The intrinsic hole densities c_{pi} of the contacts is in the order of 10^{27} m^{-3}. Due to the exponential relationship between the particle density c_{pSD} and the injection barrier $\triangle E$ the resulting particle

density is very sensitive to changes of the injection barrier [35][36][37][38]. It can vary in a range of $10^{18} - 10^{24}\ m^{-3}$. However, the carrier concentration at the interface between the contacts and pentacene plays a minor role for the capacity of the FET. For the hole densities, therefore, also Dirichlet boundary conditions

$$n_p(x, y) = c_{pSD} \quad \text{on } C_s \text{ and } C_d \tag{5.12}$$

are suitable at the contacts. The length of the contacts is a few mm, equipotential lines between source and drain contact and gate pass in some μm distance from the channel parallel to the contacts. For this reason, it is justified for the lateral boundaries C_b and C_e to adopt Neumann boundary conditions

$$\begin{aligned} \frac{\partial \phi(x, y)}{\partial x} &= 0 \quad \text{on } C_b \text{ and } C_e, \\ \frac{\partial n_p(x, y)}{\partial x} &= 0 \quad \text{on } C_b\ . \end{aligned} \tag{5.13}$$

Due to the channel length the electric field can be assumed to be parallel to C_b, so that

$$\frac{\partial \phi(x, y)}{\partial y} = 0 \quad \text{at } C_a \tag{5.14}$$

can be adopted as boundary condition. For the holes, the interface pentacene-SiO_2 and pentacene-air provides a impenetrable barrier, therefore,

$$\frac{\partial n_p(x, y)}{\partial y} = 0 \quad \text{at } C_a \text{ and } C_c \tag{5.15}$$

holds.

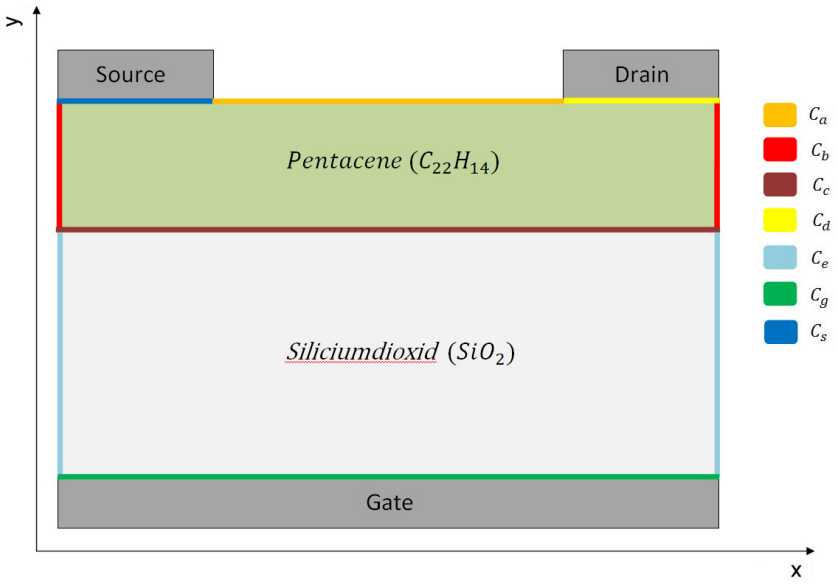

Fig. 5.5: Boundary conditions of the organic thin film transistor.

Discretisation of the device: Because of the geometry of the device, a discretization by rectangular elements is useful. As basis functions quadratic Lagrange quadrangle elements were chosen. These elements are described in Sec. 4.3. As can bee seen in Fig. 5.6, the area is discretized very fine near the contacts. At the interface between pentacene and SiO_2 also a very fine discretization is chosen. Because of the very long channel, it is inefficient to realize this fine discretization over the entire channel length.

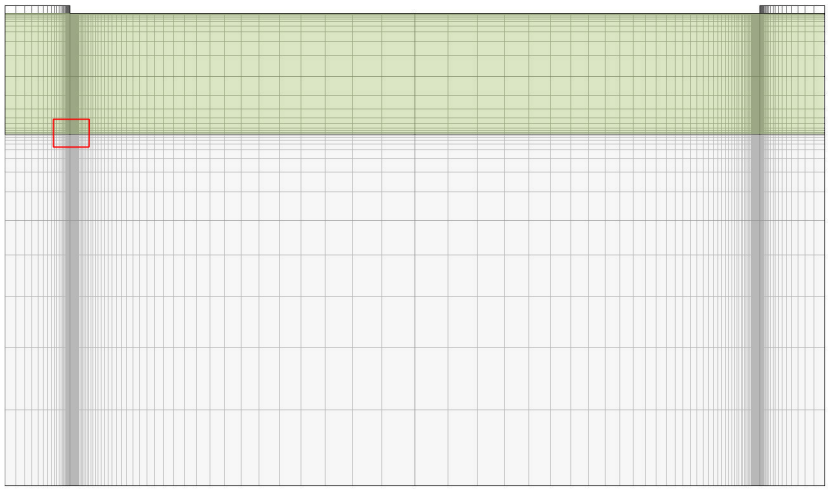

Fig. 5.6: Schematic representation for the discretization of the domain.

For this reason, the elements are chosen in a way so that they grow in area exponentially from the channel beginning towards th channel center as can be seen in Fig. 5.6. The area marked in red symbolizes the zoom range of Fig.5.7.

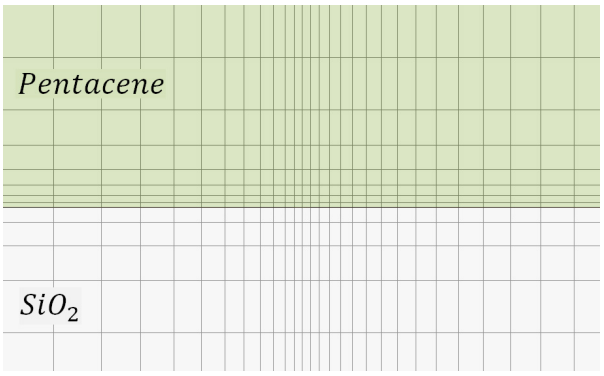

Fig. 5.7: Zoomed area of Fig. 5.6.

Simulation results: We start with Tab. 5.1 in which all input parameters required for the simulation are given. The simulation results are presented graphically and analyzed. To validate the numerical accuracy, the numerically calculated stored charge (capaci-

tance) of the FET is compared between two different methods. The charging of the capacitor channel is also plotted.

Tabelle 5.1: Parameters for the simulation

ε_{r1} / $A^1s^1V^{-1}m^{-1}$	3.4
ε_{r2} / $A^1s^1V^{-1}m^{-1}$	4.5
d_1 / nm	35
d_2 / nm	147
l_k / μm	50
l_d / mm	7
U_S / V	0
U_D / V	-2
U_G / V	-60
μ_p / $m^2V^{-1}s^{-1}$	$1 \cdot 10^{-6}$
c_{pSD} /m^{-3}	$1 \cdot 10^{24}$
T / K	298.15

The simulation based on the parameters in Tab. 5.1 yields a charge amount of $Q_{n1} = 5.56 \cdot 10^{-}9$ As in the channel. This amount of charge is calculated by subtracting the current flowing out of the channel from the current flowing into the channel, as can be seen in Fig. 5.8. The direct integration of the charge density n_p in the channel based on Eq. (5.9) resulted in a charge amount of $Q_{n2} = 5.597 \cdot 10^{-9}$ As. Furthermore, one can see in Fig. 5.8 that the charging time of such a FET is in the range of $3 \cdot 10^{-5}$ seconds. It turns out that the loading process runs fairly uniform as can be seen in Fig. 5.9a. This is due to the slow decrease of the difference between inflowing and outflowing currents ever a period of $\approx 10^{-5}$ sec (Fig. 5.9b). After that point the difference rapidly goes to zero and one can stop the simulation. The deviation of the two numerically determined amounts of charge Q_{n1} and Q_{n2}, is less than one percent. This demonstrates that the calculation of the hole densities as shown in Fig. 5.10-5.11 and the resulting currents during the time evolution provide reliable data.

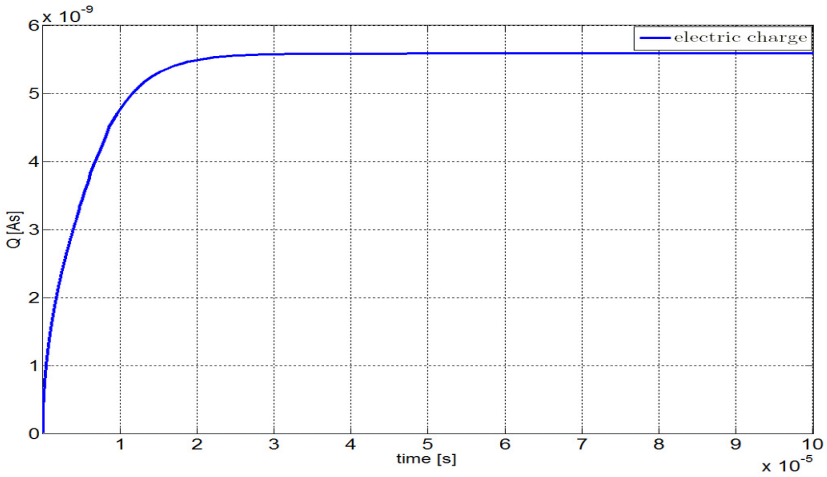

Fig. 5.8: Charging of the capacitor over time.

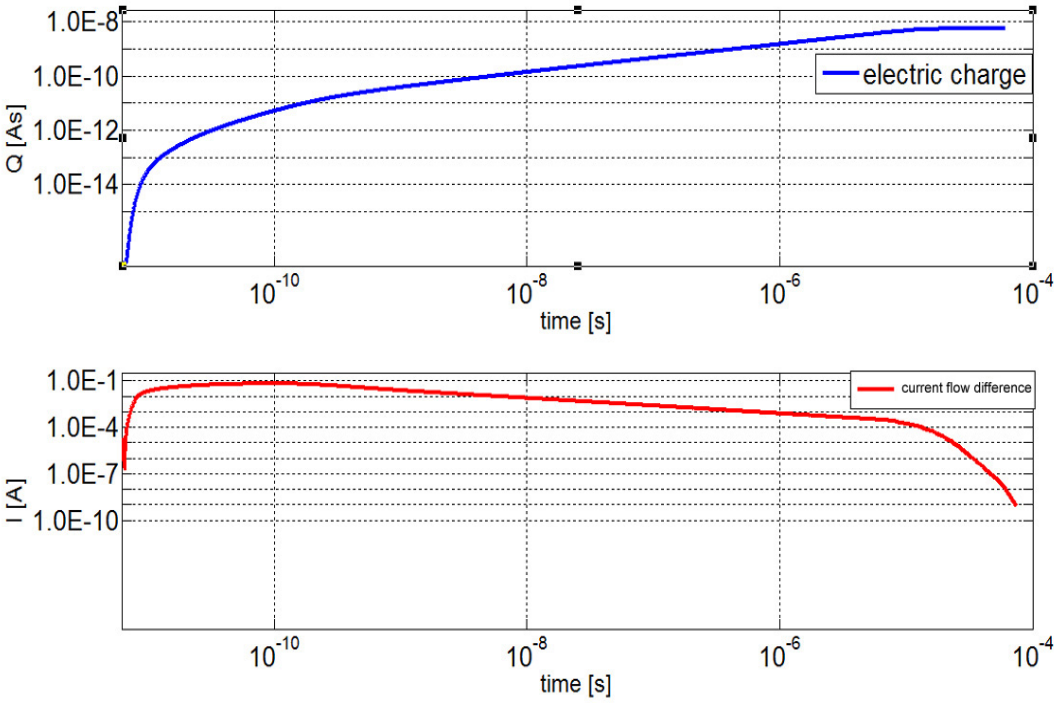

Fig. 5.9: a.) Logarithmic plotted charging Q(t) of the capacitor over time.
b.) Difference I between the currents flowing in and out of the channel.

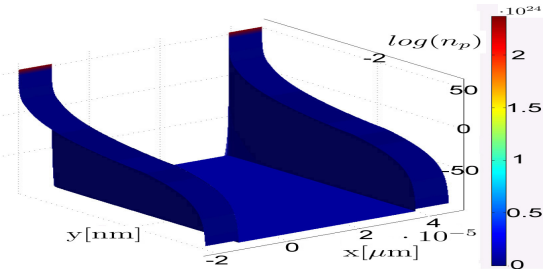

(a) Hole density n_p at the time $t = 10^{-20}$.

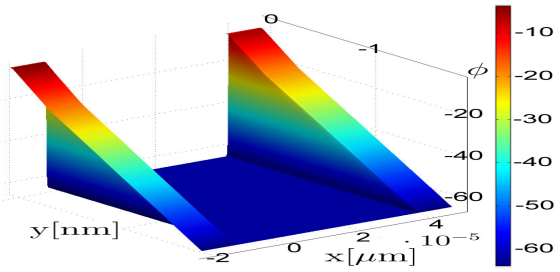

(b) Potential ϕ at the time $t = 10^{-20}$.

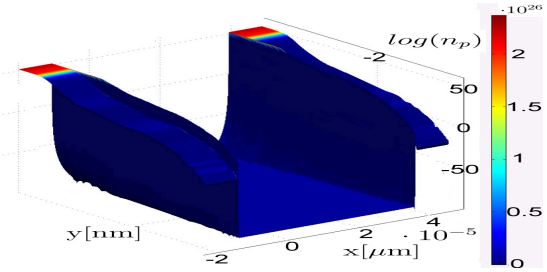

(c) Hole density n_p at the time $t = 10^{-11}$.

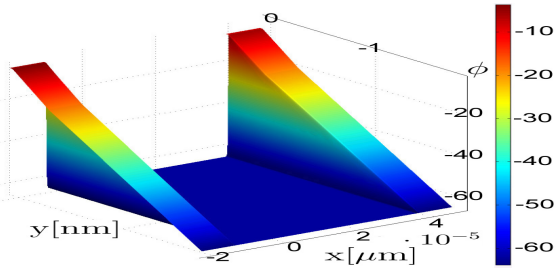

(d) Potential ϕ at the time $t = 10^{-11}$.

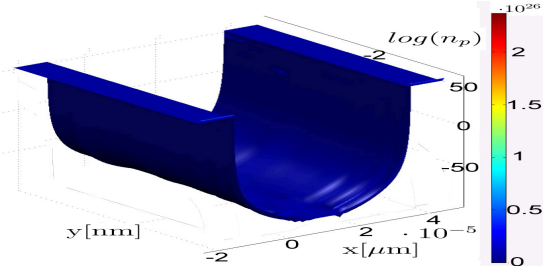

(e) Hole density n_p at the time $t = 10^{-10}$.

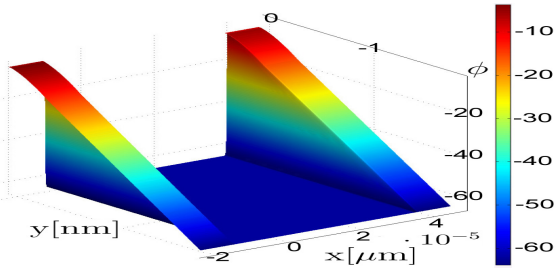

(f) Potential ϕ at the time $t = 10^{-10}$.

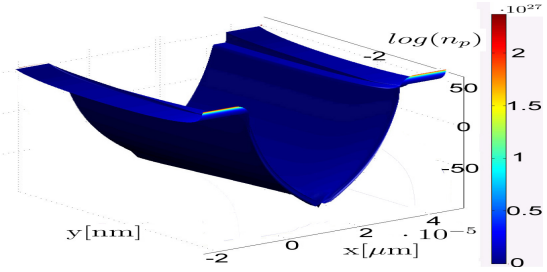

(g) Hole density n_p at the time $t = 10^{-7}$.

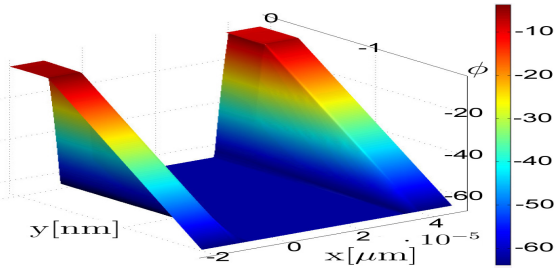

(h) Potential ϕ at the time $t = 10^{-7}$.

Fig. 5.10: Distribution of the potential ϕ and the charge carrier density n_p in the device in the first 10^{-7} seconds after the switch on.

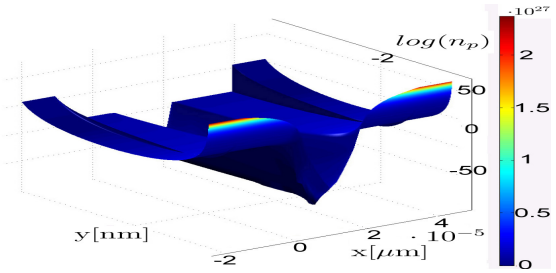

(a) Hole density n_p at the time $t = 2 \times 10^{-6}$.

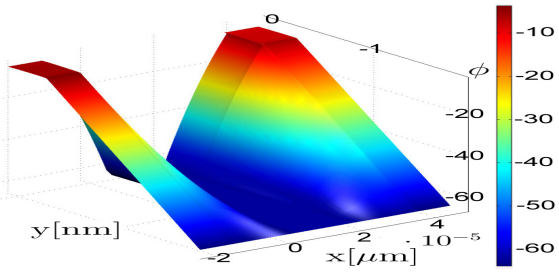

(b) Potential ϕ at the time $t = 2 \times 10^{-6}$.

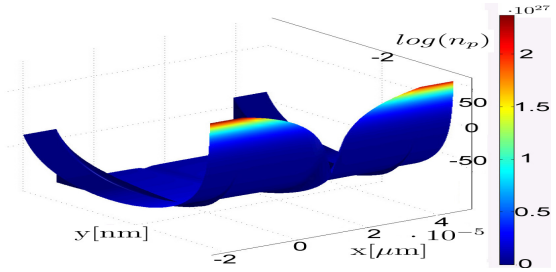

(c) Hole density n_p at the time $t = 4 \times 10^{-6}$.

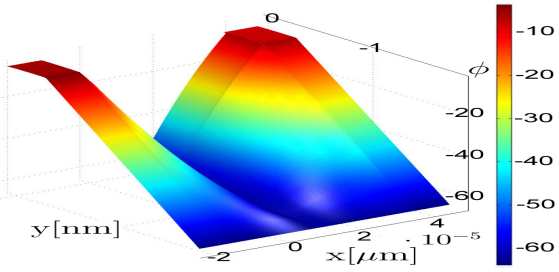

(d) Potential ϕ at the time $t = 4 \times 10^{-6}$.

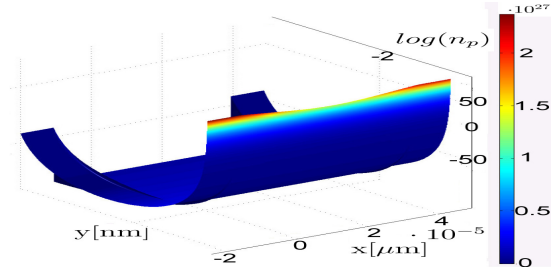

(e) Hole density n_p at the time $t = 10^{-5}$.

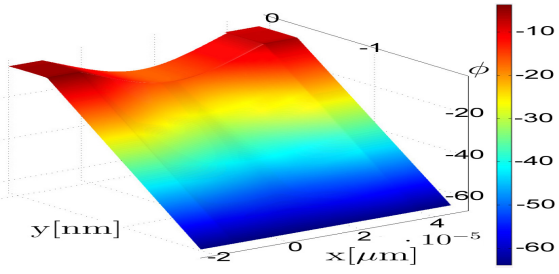

(f) Potential ϕ at the time $t = 10^{-5}$.

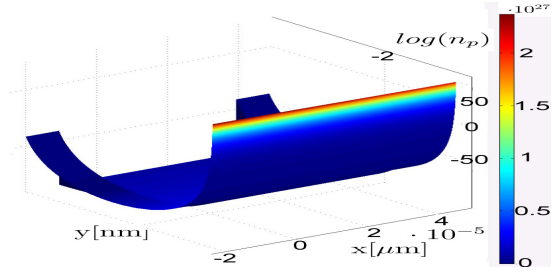

(g) Hole density n_p at the time $t = 10^{-4}$.

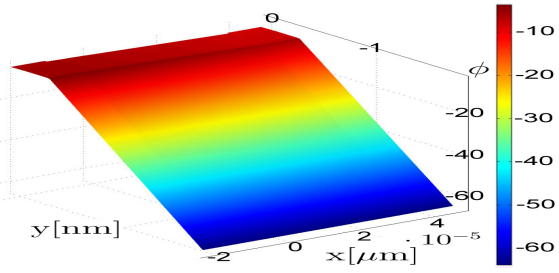

(h) Potential ϕ at the time $t = 10^{-4}$.

Fig. 5.11: Distribution of the potential ϕ and the charge carrier density n_p in the device between 10^{-7} and 10^{-4} seconds (stady state) after the switch on.

6 Experimental Results

This chapter consists of three sections. In the first section the construction of the organic thin-film transistor is described. The second section contains the measurements and the last section deals with interpretations of the results.

6.1 Architecture of the Organic Thin-Film Transistor

All experimental data shown and discussed are obtained from measurements on OTFTs built and characterized by Ausserlechner [39] in the period from 2009-2010. The OTFT is based on an active layer of pentacene with a thickness of 35nm. An additional layer of two trichlorosilanes, namely 4-(2-(trichlorosilyl)ethyl)benzene-1-sulfonyl chloride (T-SC, 70 %) and a sulfonic acid derivate 4-(2-(trichlorosilyl)ethyl)benzenesulfonic acid (T-SA, 30 %) is arranged between the SiO_2 and pentacene as shown in Fig. 6.1. The thickness of this layer is 1 nm.

The outer dimensions of this OTFT are identical to those in Sec. 5 (see, Fig. 5.3 and Tab. 5.1). The device width $l_d = 7$ mm (see Fig. 5.1) and the channel length $l_k = 50$ μm. For investigating the behavior of the interfacial layer, three different oxide layer thicknesses $d_2 = 100, 147.5$ and 245 nm were considered. As a reference for the measurements also transistors without an interfacial layer for each oxide thickness were produced.

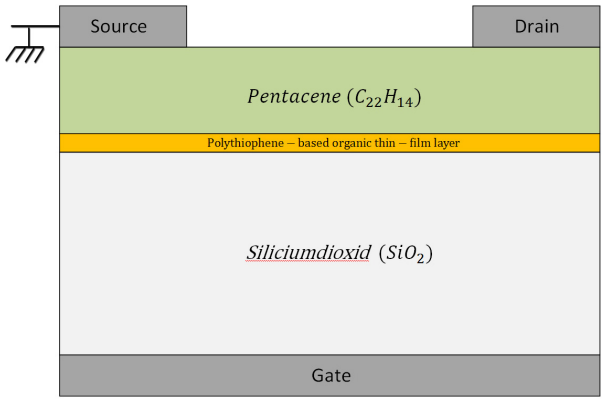

Fig. 6.1: Schematic structure of the organic thin-film transistors with an interfacial layer.

6.2 Measurements

This section presents the electrical characterization of OTFTs with oxide thicknesses of 100 nm, 147.5 nm and 245 nm. All the necessary measurements were performed by Ausserlechner [39]. Mobility measurements of the pentacene devices yield a hole mobility of about 10^{-6} $m^2V^{-1}s^{-1}$.

Transistors With an Oxide Thickness of 100, 147.5 and 245 nm: In total eight devices with a SiO_2 layer of 100 nm were investigated. The first four transistors are endowed with the interfacial layer being one nm thick. The remaining four transistors are produced without the interfacial layer and serve as a reference. In total six devices with an SiO_2 layer thickness of 147 and 245 nm were measured. The first three transistors with 147 and 245 nm were equipped with the interfacial layer. The remaining transistors are produced without the interfacial layer to serve again as a reference.

In Fig. 6.2, Fig. 6.6 and Fig. 6.10 the transfer characteristic of the reference devices are shown. From the plots it can be seen that the threshold voltage of all reference devices is about 0 V. The threshold voltage U_{th} is defined as the gate voltage at which a charge-carrier layer is formed at the interface between the insulating material and the pentacene. After reaching the U_{th}, the source-drain current begins to rise. The transistors with the interfacial layer and an oxide thickness of 100 nm, however, have a threshold voltage of about 30 V, as can be seen in Fig. 6.3 and 6.4. The transistors with the interfacial layer and an oxide thickness of 147.5 nm have a threshold voltage of about 60 V, as can be seen in Fig. 6.7 and Fig. 6.8, and the transistors with the interfacial layer and an oxide thickness of 245 nm have a threshold voltage of approximately 120 V, as can be seen in Fig. 6.11 and 6.12. The figures show a significant hysteresis. To, nevertheless, analyze the data, the measured values were averaged by

$$y(x_n) = \frac{y1(x_n) + y2(x_n)}{2} \quad \text{for } n = 1, 2, \ldots, m, \tag{6.1}$$

to obtain a unique function of all m values. In Eq. (6.1), $y1(x_n)$ denotes the higher and $y2(x_n)$ the lower measured current value I_D at a gate voltage $U_g = x_n$. Then, the resulting transfer curve is interpolated in the linear region between $U_G = 0$ V and $U_G = 25$ V using a linear least-squares fit [40]. Fig. 6.5 shows the interpolated function and the linear fit for the first device with an oxide thickness of 100 nm. Figure 6.9 shows the interpolated function and the linear fit for one of the 147.5 nm devices with interfacial layer and Figure 6.13 shows the interpolated function and the linear fit for one of the 245 nm devices with interfacial layer. The so calculated threshold voltage for all 100 nm devices is displayed in Tab. 6.1, the threshold voltages of the 147.5 nm devices are listed in Tab. 6.2 and the threshold voltage of the 245 nm devices is listed in Tab. 6.3.

Tabelle 6.1: Threshold voltages for the four transistors with an an interfacial layer and a 100 nm thick SiO_2 layer.

Parameter	Value
$U1_{th}$ / V	35.4
$U2_{th}$ / V	29.5
$U3_{th}$ / V	33.4
$U4_{th}$ / V	35.9

Tabelle 6.2: Threshold voltages for the three transistors with an an interfacial layer and a 147.5 nm thick SiO_2 layer.

Parameter	Value
$U1_{th}$ / V	62.8
$U2_{th}$ / V	63.9
$U3_{th}$ / V	50.54

Tabelle 6.3: Threshold voltages for the three transistors with an an interfacial layer and a 245 nm thick SiO_2 layer.

Parameter	Value
$U1_{th}$ / V	122.1
$U2_{th}$ / V	125.2
$U3_{th}$ / V	125.0

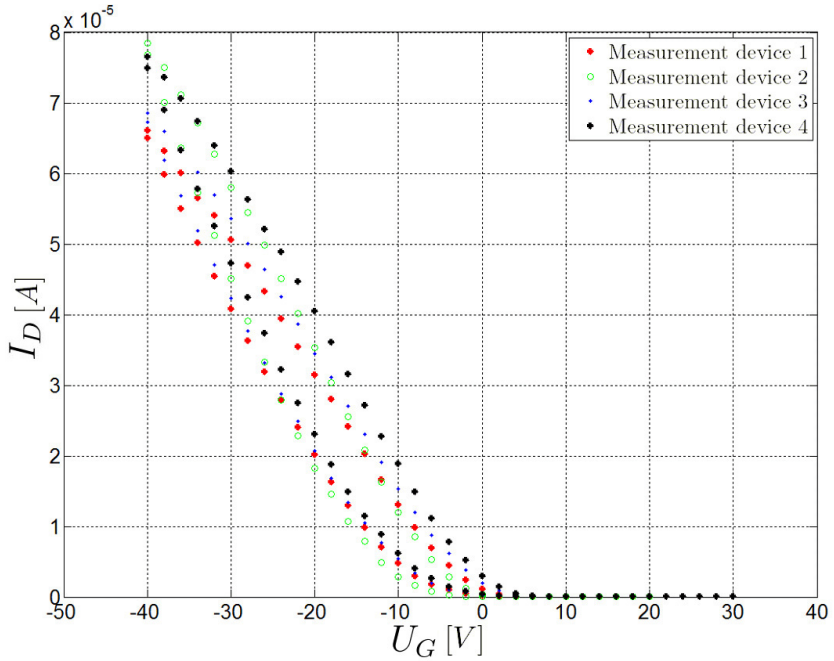

Fig. 6.2: Measured transfer characteristics of the 100 nm transistor without interfacial layer.

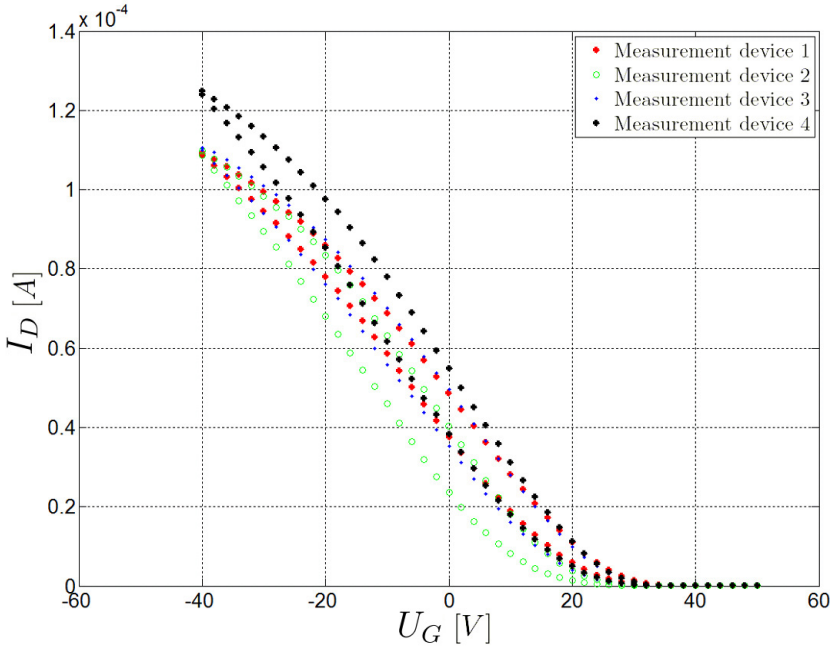

Fig. 6.3: Measured transfer characteristics of the 100 nm transistor with interfacial layer.

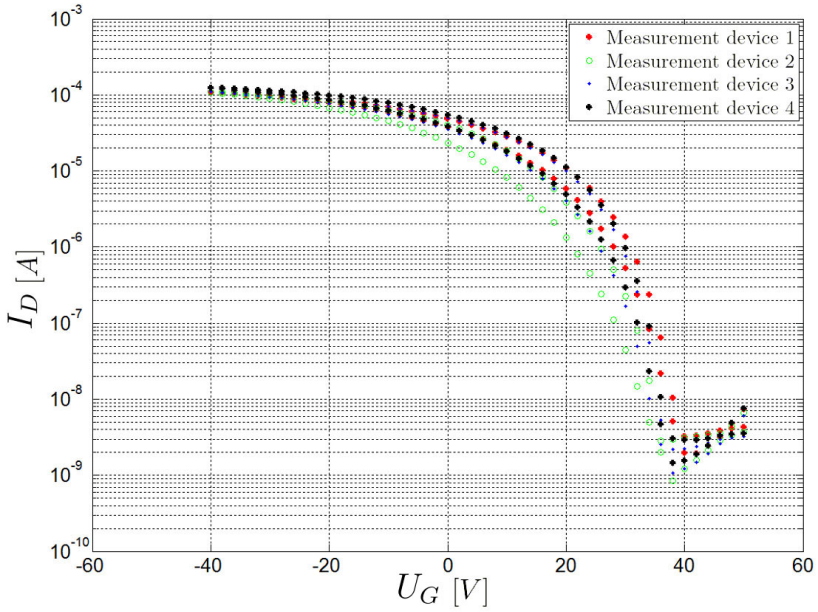

Fig. 6.4: Logarithmic plot of the measured transfer characteristics of the 100 nm transistor with interfacial layer.

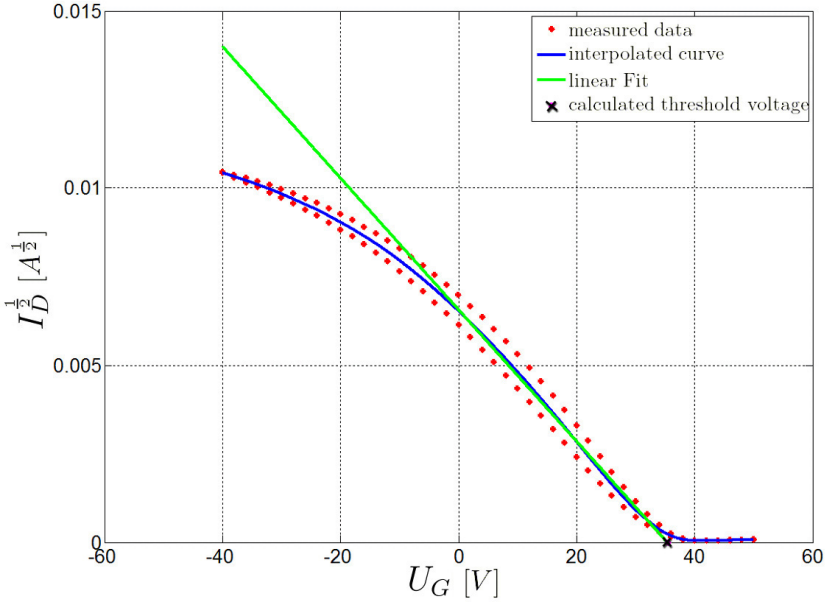

Fig. 6.5: Determination of the threshold voltage for one of the 100 nm transistors with an interfacial layer by a linear fit.

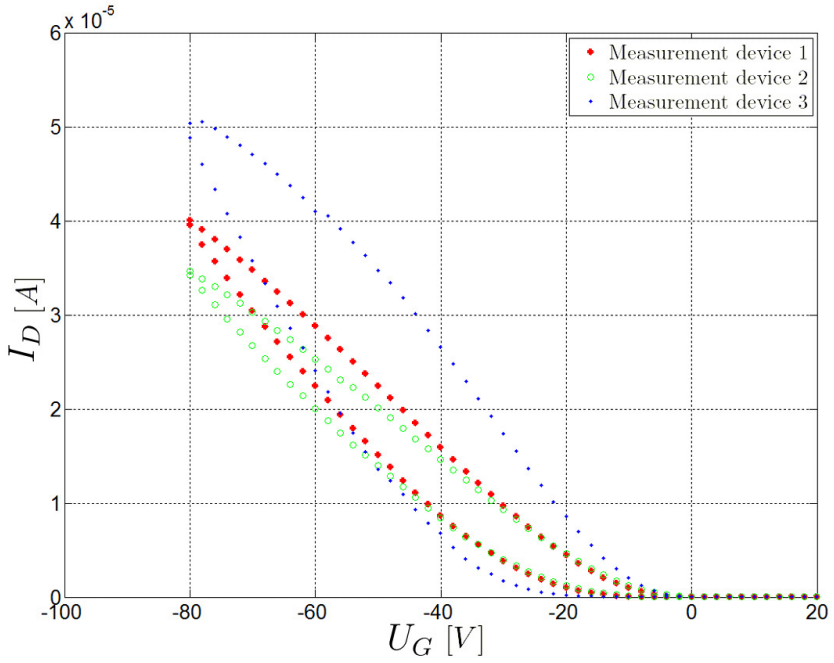

Fig. 6.6: Measured transfer characteristics of the 147.5nm transistor without interfacial layer.

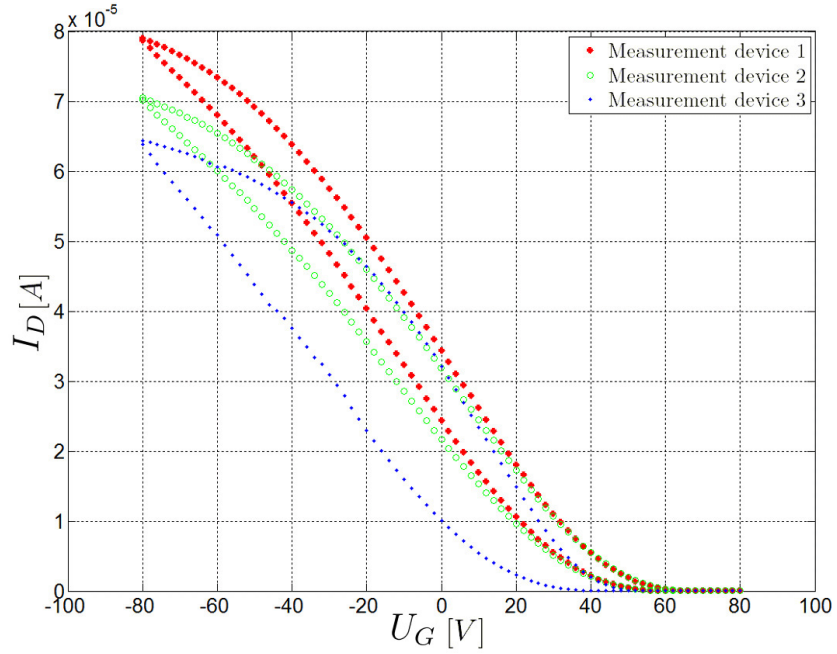

Fig. 6.7: Measured transfer characteristics of the 147.5nm transistor with interfacial layer.

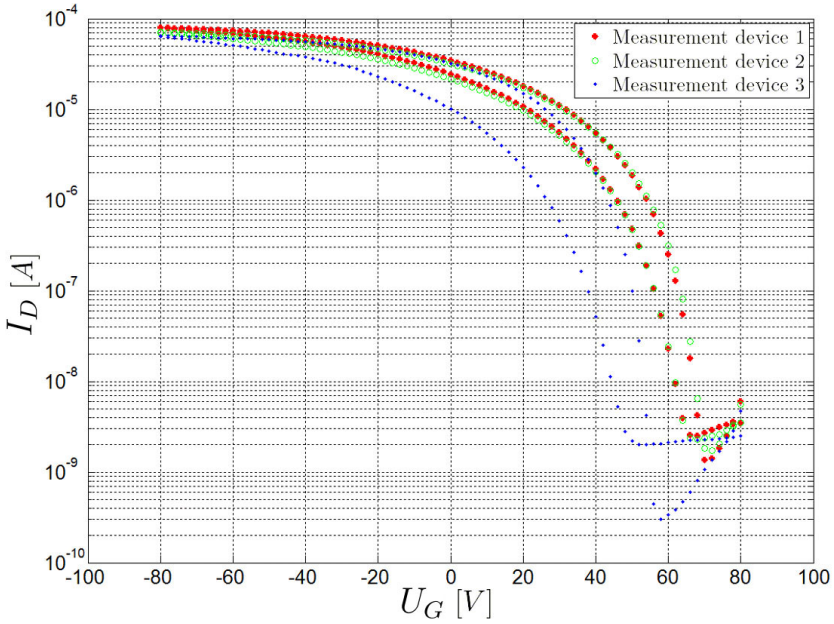

Fig. 6.8: Logarithmic plot of the measured transfer characteristics of the 147.5nm transistor with interfacial layer.

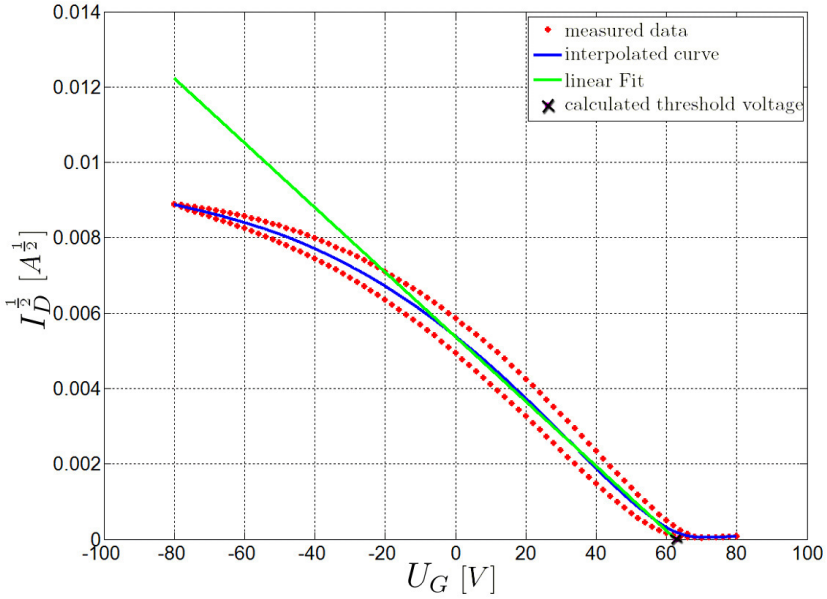

Fig. 6.9: Determination of the threshold voltage for one of the 147.5 nm transistors with an interfacial layer by a linear fit.

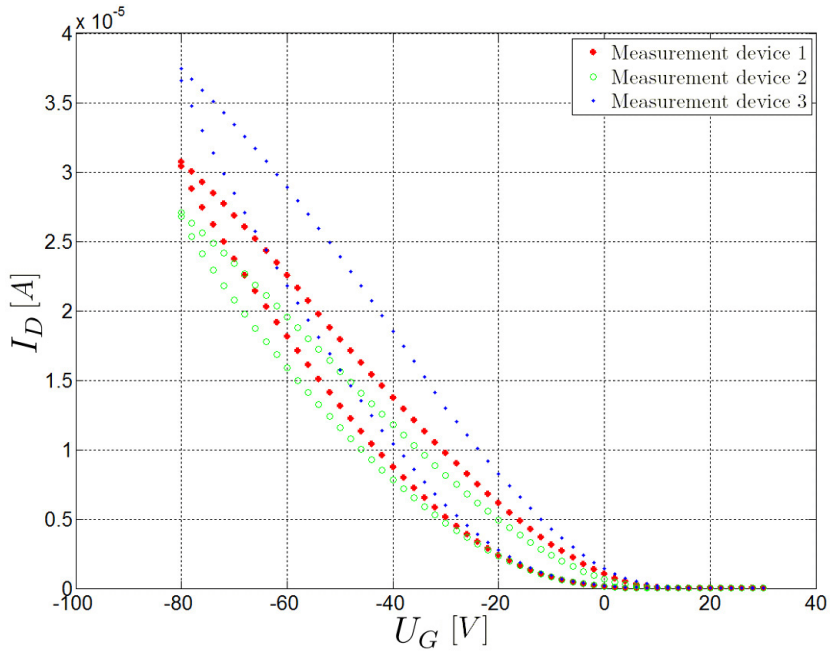

Fig. 6.10: Measured transfer characteristics of the 245nm transistor without interfacial layer.

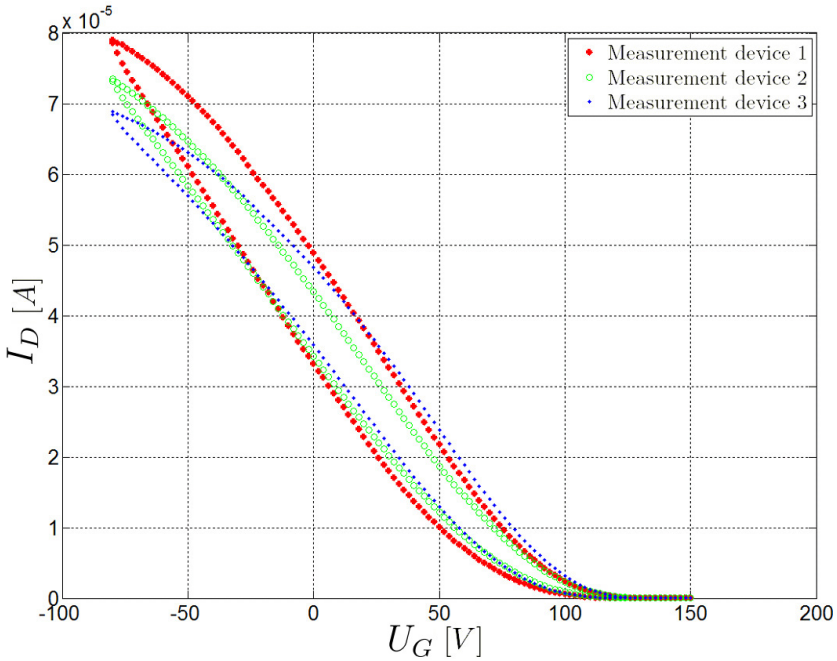

Fig. 6.11: Measured transfer characteristics of the 245nm transistor with interfacial layer.

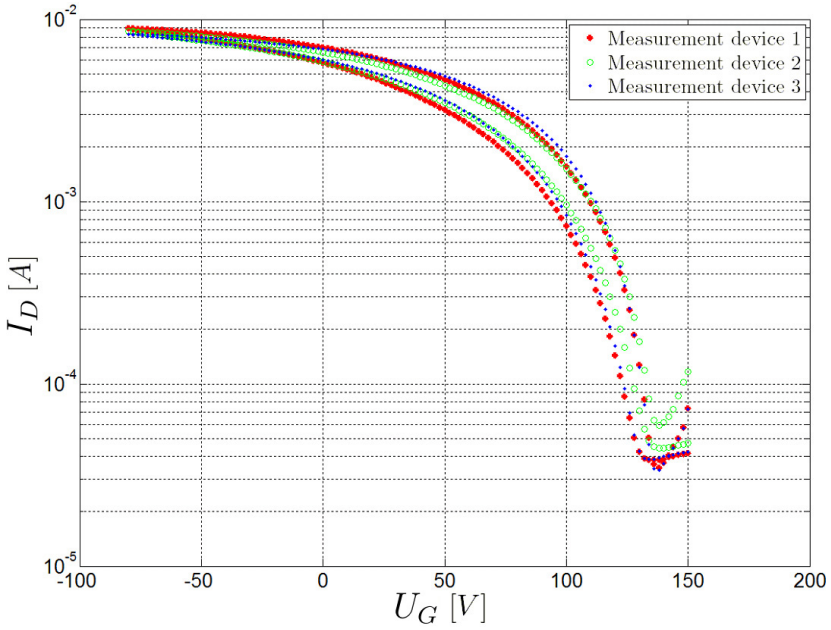

Fig. 6.12: Logarithmic plot of the measured transfer characteristics of the 245nm transistor with interfacial layer.

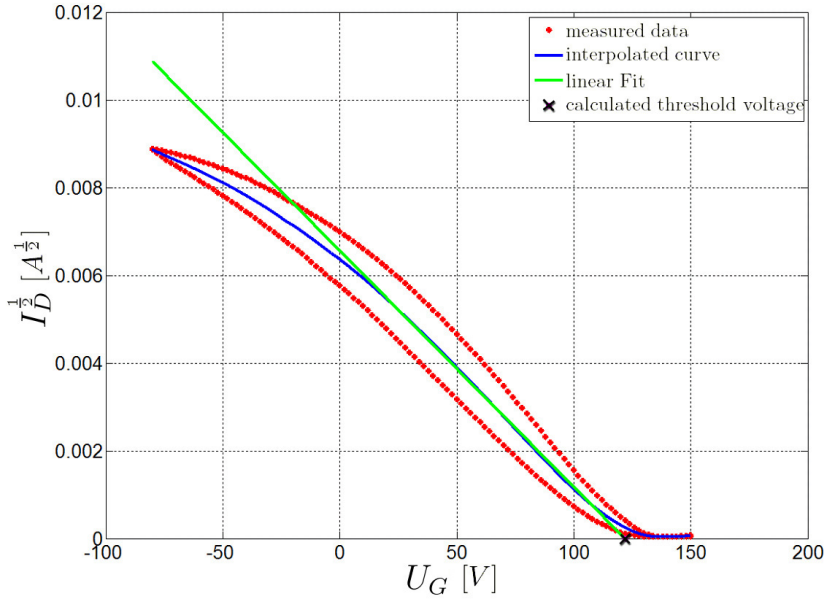

Fig. 6.13: Determination of the threshold voltage for one of the 245 nm transistors with an interfacial layer by a linear fit.

6.3 Evaluation of the Measured Results

In the devices with an interfacial layer, a shift of the threshold voltage by several ten volts compared to the one in the reference devices occurred. It seems likely that this is attributable to the sulfonic acid groups of the T-SA molecules being deprotonated. The resulting H^+ ions can then diffuse into the pentacene. This results in the formation of a space charge layer consisting of the negative acidic residue. Due to the shift we propose a proton doping mechanism with the proton attaching to the central ring of the pentacene molecule shown in Fig. 6.14 and Fig. 6.15.

This is supported by the observation that U_{th} decreases to zero, when exposing the devices to an ammonia (NH_3) gas. The NH_3 molecules react with the protons and the acidic residue groups, [41] resulting in a disappearance of the pentacene doping and of the space charge layer as shown in Fig. 6.16.

The formation of the charge layer is very slow; it takes two to three weeks until the steady state is reached. This raises the question what process is in part responsible for the long time duration. The compensation process with NH_3 just takes a few seconds.

Chapter 7 tries to verify this hypothesis and attempts to give answers to open questions by means of numerical simulations.

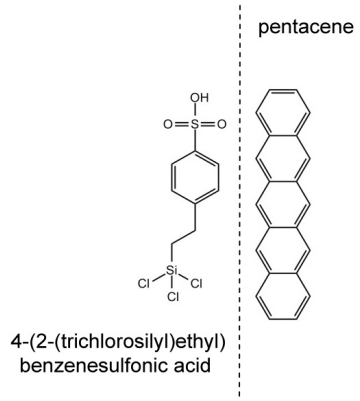

Fig. 6.14: This image shows the interface between pentacene and the interfacial layer at the beginning of the doping process.

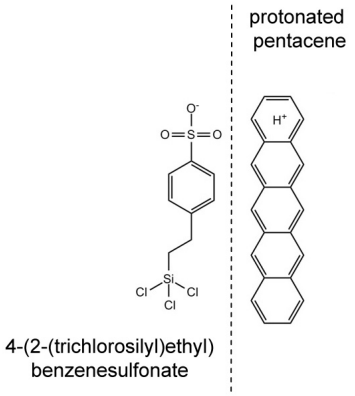

Fig. 6.15: This image shows the interface between pentacene and the interfacial layer at the end of the doping process.

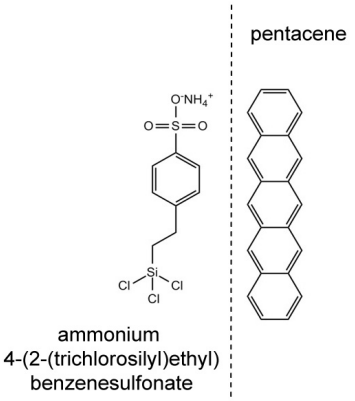

Fig. 6.16: This image shows the interface between pentacene and the interfacial layer after exposure of NH3.

7 Space Charge Layer Formation in Pentacene Based Organic Thin-Film Transistors

This chapter is divided into six sections. The first section briefly describes the discretization of the device for the finite element method. Then in the second section, a simple base model for the simulation of the Organic Thin-Film Transistors with the interface layer is presented. The simulations based on this model are compared with the measured values. With the help of this simulation results an improved model is developed. In the third section this improved model is introduced. The simulation results of the improved models are again compared with the measured values. The findings of that will be reused to improve the simulation model. In sections four and five, the model is evolved based on the results of its predecessor. Section six deals with the influence of NH_3 on the device.

7.1 Discretisation of the Device

Because of the geometry of the device, a discretization by rectangular elements is useful. As basis functions quadratic Lagrange functions were chosen. These elements are described in more detail in Sec. 4.3. As seen in Fig. 7.1 and Fig. 7.2, the area was discretized very fine in near the contacts. At the interface between pentacene - SAM and SAM - SiO_2 also a very fine discretization was chosen. Because of the very long channel, it is inefficient to obtain this fine division over the entire channel length. To reach an efficient simulation with greatest possible accuracy, the elements were chosen so that there extension grow, starting from the beginning and end of the channel towards the channel center, exponentially. The area in Fig. 7.1 marked in red symbolizes the zoom range from Fig. 7.2.

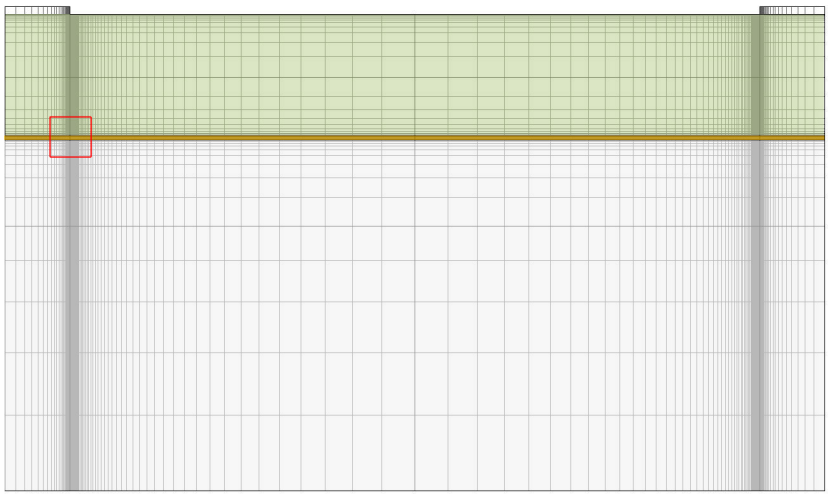

Fig. 7.1: Schematic representation of the discretization of a pentacene based organic thin film transistor with a SAM.

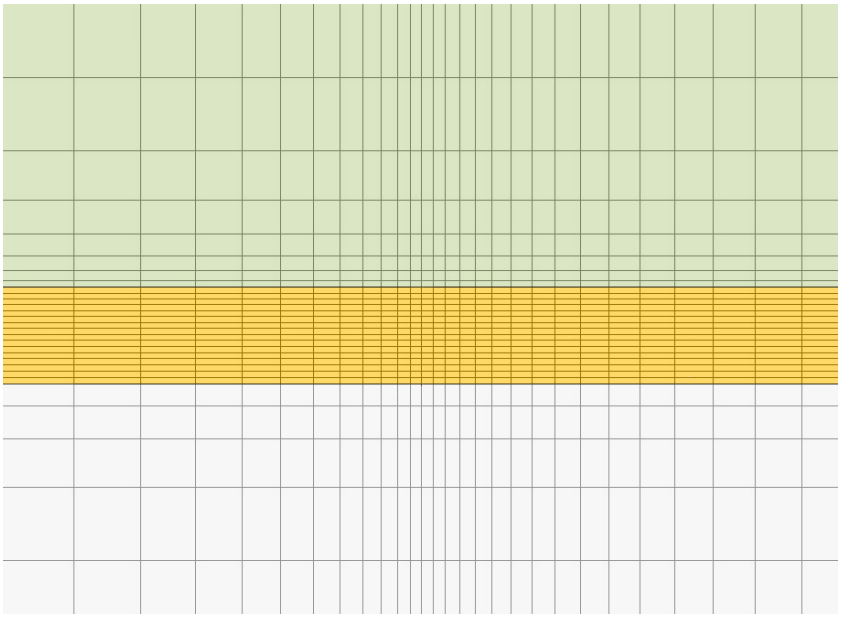

Fig. 7.2: Zoomed area of Fig. 7.1.

7.2 Standard Model

First the standard model for simulating the organic thin film transistor is described briefly. Then the boundary conditions are fixed. The simulation results are presented next. The last part of this chapter deals with the evaluation of the simulation results.

Simulation Model: As a first attempt we try to simulate the measurements of a FET without the interfacial layer. Due to the high injection barrier at the contacts we neglect the influence of electrons for the charge transport. The charge transport in pentacene, is modeled as in Sec. 5.1, the boundary conditions are as in Sec. 5.2.

Simulation Results: This section presents the simulation results of the standard model. All parameters for the model are listed in Tab. 7.2. As one can see in Fig. 7.3 and Fig. 7.4 the agrement between the simulation and the measured data is poor. Measurements of the devices (Sec. 6), yield a hole mobility of about 1×10^{-6} $\mathrm{m^2V^{-1}s^{-1}}$ in pentacene. For gate voltages of just a few volts, the simulation of the transfer curve is near the measurements as one can see in Fig. 7.3. But for gate voltages above 20V the measured current increases much stronger than predicted through the simulation. The consistency of the simulation with the measurements can be improved for higher voltages by a higher mobility. With a higher mobility, the simulation provides wrong results in the section below U_G=−30V as can be seen in Fig. 7.4.

Tabelle 7.1: Parameters for the simulation of the standard model

Parameter	Value
ε_{r1} / $A^1s^1V^{-1}m^{-1}$	3.4
ε_{r2} / $A^1s^1V^{-1}m^{-1}$	4.5
d_1 / nm	35
d_2 / nm	147
l_k / μm	50
l_d / mm	7
U_S / V	0
U_D / V	-2
U_G / V	$-80 \ldots 20$
μ_p / $m^2V^{-1}s^{-1}$	$1 \cdot 10^{-6}$; $1 \cdot 10^{-5}$;
$\triangle E$ /eV	0.47
c_{pi} / m^{-3}	$1 \cdot 10^{27}$
T / K	298.15

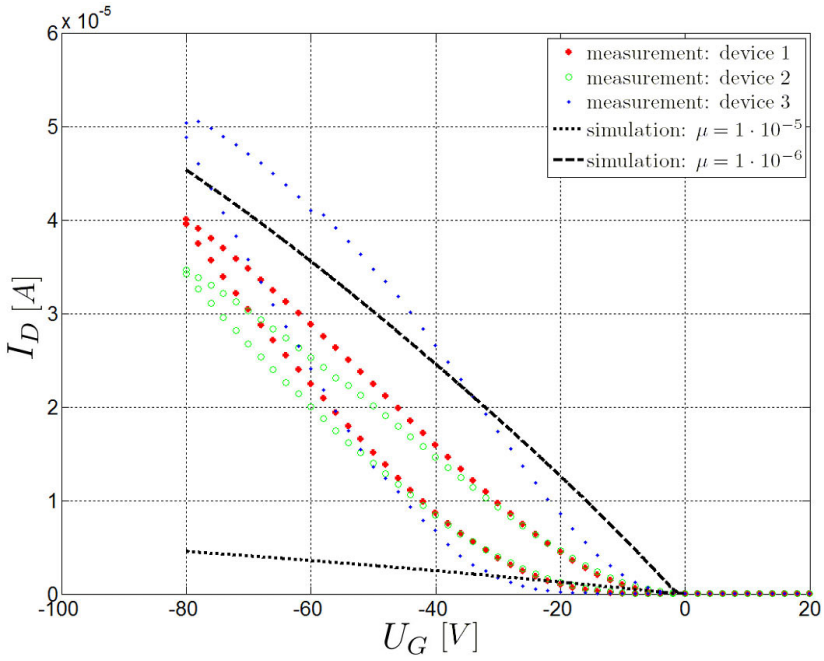

Fig. 7.3: Linear plot of the transfer characteristic of the simulation. ($d_2 = 147$nm)

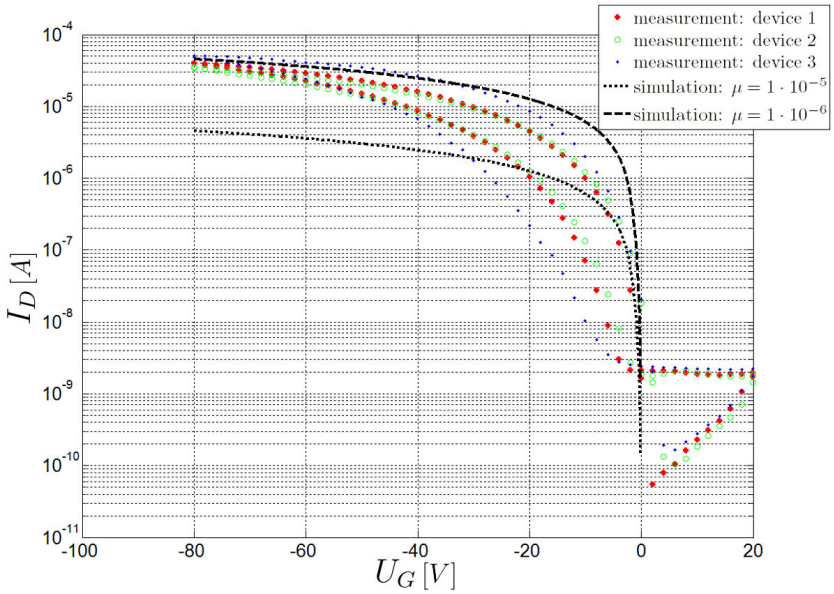

Fig. 7.4: Logarithmic plot of the transfer characteristic of the simulation.

To get better results in the simulation it is necessary to take into account the electric field dependence of the mobility. According to the Poole-Frenkel effect one use an approximation of the mobility which depends on the square root of the electric field [2].

For the mobility in the device we get:

$$\mu_p = \mu_{p0} e^{\left(-q\frac{\Theta}{k_B T} + q\left[\frac{\beta}{k_B T} - \gamma\right]\sqrt{||\mathbf{E}||}\right)} \tag{7.1}$$

It depends on the temperature T, on the norm of the electric field $\mathbf{E}$, on the zero field mobility μ_{p0}, on the zero field activation energy Θ, on the Poole-Frenkel factor β and on a fit parameter γ. For the zero field mobility μ_{p0} we use the mobility from the measurements of 10^{-6}. We assume for the zero field activation energy $\Theta = 0.1$ eV and for the Poole-Frenkel factor $\beta = 3.58 \times 10^{-5}$ eV$(\mathrm{cmV}^{-1})^{1/2}$ as proposed in [2]. In the simulation, the fit parameter is $\gamma = 10^{-4}$ $(\mathrm{cmV}^{-1})^{1/2}$. As one can see in Fig. 7.5 the consistency with the measured values is now much better. One sees that the measurements show a hysteresis which does not occur in the simulation. To simulate this hysteresis we must still consider traps in pentacene[42]. However, this would not provide significant new insights because we are interested in a change of the threshold voltage through an additional layer in the device. In order to get along with a minimum of parameters, the influence of traps will be ignored throughout this thesis and are discussed in [43].

Tabelle 7.2: Parameters for the simulation of the standard model

Parameter	Value
ε_{r1} / $A^1s^1V^{-1}m^{-1}$	3.4
ε_{r2} / $A^1s^1V^{-1}m^{-1}$	4.5
d_1 / nm	35
d_2 / nm	147
l_k / μm	50
l_d / mm	7
U_S / V	0
U_D / V	-2
U_G / V	$-80 \ldots 20$
μ_{p0} / $m^2V^{-1}s^{-1}$	$2 \cdot 10^{-6}$
θ / eV	0.1
β / $eV(cm/V)^{1/2}$	$3.58 \cdot 10^{-5}$
γ / $(cm/V)^{1/2}$	$1 \cdot 10^{-4}$
$\triangle E$ /eV	0.47
c_{pi} / m^{-3}	$1 \cdot 10^{27}$
T / K	298.15

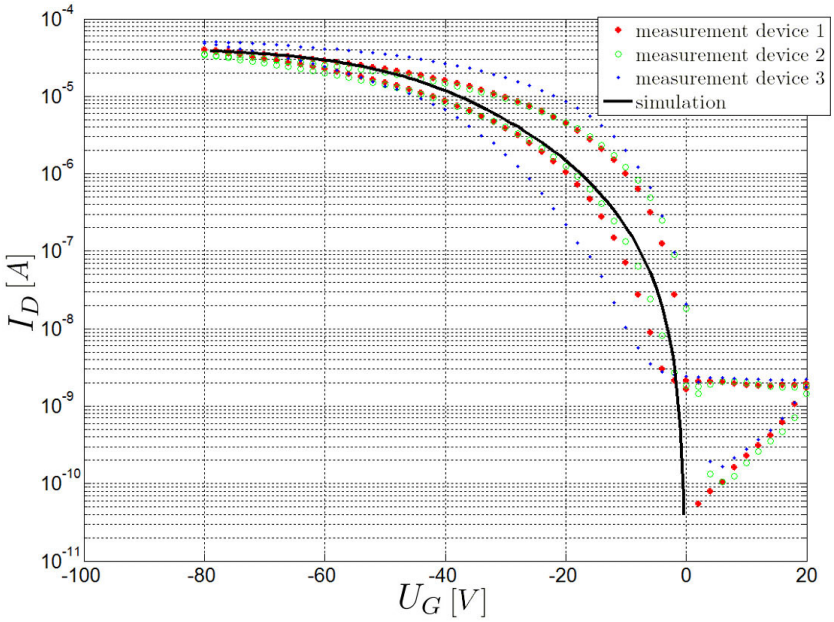

Fig. 7.5: Logarithmic plot of the transfer characteristic of the simulation with field dependent mobility.

7.3 Model 1

In the first sub-section the model 1 for simulating the organic thin film transistor is described briefly. Then the boundary conditions are fixed. The simulation results are presented in the third subsection. Chapter four deals with the evaluation of the simulation results.

Simulation Model: As a first attempt we try to simulate the results with a very simple base model to better understand the working principle. Leakage currents between source and gate or drain and gate are neglected. The charge transport in pentacene, based on holes, is described by the drift diffusion equation (3.100) in combination with the Poisson equation (3.126). Chemical reactions such as the formation of H^+ ions in the SAM are neglected. It is assumed that at the beginning of the simulation in the SAM, a constant positive H^+ ion density $c_I = c_{I-SAM}$ with a mobility μ_I is present. The H^+ ion density can be estimated by assuming that from 0.1 to a maximum of one molecule of SAM (4-(2-(trichlorosilyl)ethyl)benzenesulfonic acid) per nm^2 one H^+ ion is released. This assumption leads to an H^+ ion density c_{I-SAM} of about 10^{26} m^{-3} up to a maximum of 10^{27} m^{-3}. The relative permittivity of the SAM is not known. Since the SAM is with a single nm very thin, an average value of $\varepsilon_{r-SAM} \approx 4$ between pentacene and SiO_2 will be assumed. It is also assumed that the mobility of H^+ ions in the SAM and pentacene is identical. The negative acidic residue $c_r = c_{I-SAM}$ has the same density as the H^+ ions so that charge neutrality is preserved. The negative acidic residue has no mobility. The H^+ ions can diffuse in the pentacene but not in the SiO_2. The H^+ ions cannot escape

into the vacuum or on the contacts. The number of H^+ ions in pentacene and SAM is thus a conserved quantity. To consider the electric potential of holes and H^+ ions in the device we use the Poisson equation (3.126). The Poisson equation for this model is given by

$$\varepsilon_0 \nabla \left[\varepsilon_r(\mathbf{r}) \nabla \phi(\mathbf{r},t)\right] = -q \ \left[n(\mathbf{r},t) + c(\mathbf{r},t)\right] \tag{7.2}$$

where

$$\varepsilon_r(\mathbf{r}) = \begin{cases} \varepsilon_{Penta}(\mathbf{r}) & \text{in pentacene,} \\ \varepsilon_{SAM}(\mathbf{r}) & \text{in the SAM,} \\ \varepsilon_{SiO2}(\mathbf{r}) & \text{in } SiO_2, \end{cases} \tag{7.3}$$

and

$$n(\mathbf{r},t) = \begin{cases} n_p(\mathbf{r},t) & \text{in pentacene,} \\ 0 & \text{in the SAM,} \\ 0 & \text{in } SiO_2, \end{cases} \tag{7.4}$$

$$c(\mathbf{r},t) = \begin{cases} c_I(\mathbf{r},t) & \text{in pentacene,} \\ -c_I(\mathbf{r},t) + c_r & \text{in the SAM,} \\ 0 & \text{in } SiO_2. \end{cases} \tag{7.5}$$

The drift-diffusion equations which consists of the continuity equation (3.41) and the drift-diffusion current equation (3.98) are given by

$$\frac{\partial}{\partial t} n_p(\mathbf{r},t) = -\frac{1}{q} \nabla \mathbf{J}_p(\mathbf{r},t), \tag{7.6}$$

$$\frac{\partial c_I(\mathbf{r},t)}{\partial t} = -\frac{1}{q} \nabla \mathbf{J}_I(\mathbf{r},t) \tag{7.7}$$

and

$$\mathbf{J}_p(\mathbf{r},t) = -q\mu_p(\mathbf{r},t) n_p(\mathbf{r},t) \nabla \phi(\mathbf{r},t) - q\mu_p(\mathbf{r},t) k_B T \nabla n_p(\mathbf{r},t), \tag{7.8}$$

$$\mathbf{J}_I(\mathbf{r},t) = -q\mu_I c_I(\mathbf{r},t) \nabla \phi - q\mu_I k_B T \nabla c_I(\mathbf{r},t) \tag{7.9}$$

with

$$\mu_p(\mathbf{r},t) = \mu_{p0} e^{\left(-q\frac{\Theta}{k_B T} + q\left[\frac{\beta}{k_B T} - \gamma\right]\sqrt{||\mathbf{E}(\mathbf{r},t)||}\right)}. \tag{7.10}$$

Boundary Conditions: In addition to the input parameters (initial conditions) boundary conditions must be set for the numerical simulation. In Fig. 7.6 the device with the appropriate boundary conditions is shown. For this model we have to adapt the

boundary conditions of Sec. 5.2. Additionally to the conditions in Sec. 5.2 we adopt for the lateral boundaries C_b,C_f and C_e of the simulation, Neumann boundary conditions:

$$\begin{aligned} \frac{\partial \phi(x,y)}{\partial x} &= 0 \quad \text{at } C_b,C_f \text{ and } C_e, \\ \frac{\partial n_p(x,y)}{\partial x} &= 0 \quad \text{at } C_b \text{ and } C_f \ , \\ \frac{\partial c_I(x,y)}{\partial x} &= 0 \quad \text{at } C_b \text{ and } C_f \ . \end{aligned} \tag{7.11}$$

For the ions, the interface pentacene-SiO_2 and pentacene-air provides a barrier, therefore,

$$\frac{\partial c_I(x,y)}{\partial y} = 0 \quad \text{at } C_a \text{ and } C_h \tag{7.12}$$

holds.

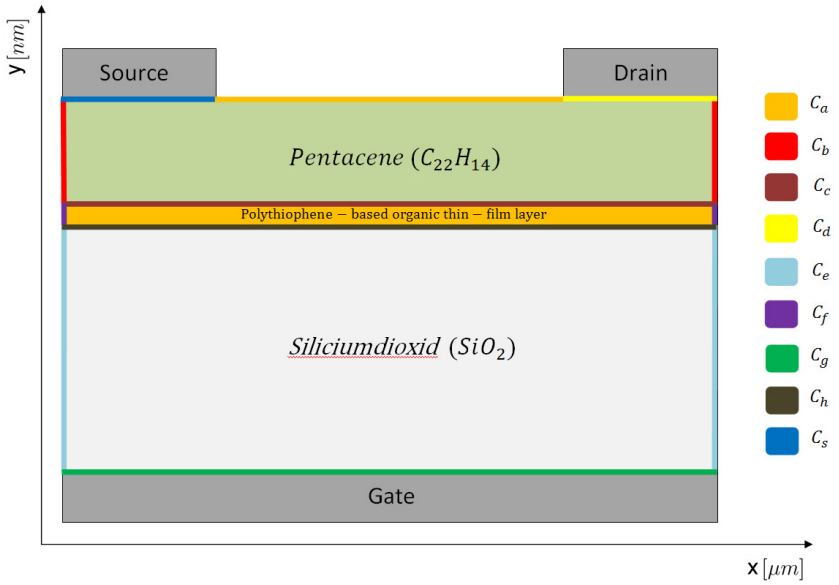

Fig. 7.6: Boundary conditions of the device with model 1.

7.3.1 Simulation Results

This section presents the simulation results of Model 1. The section consists of three parts. In the first part the H^+ ion mobility is varied and the resulting changes are presented. In the second part the existing H^+ ion density in the SAM is varied. In the last part of this section the simulation results are compared with the results of the measurements. All the general parameters for the model 1 are listed in Tab. 7.3.

To assess the impact of individual parameter changes in the individual cases considered below, the total charge Q of ions

$$Q(t) = l_d \int_{x=0}^{l_k} \int_{y=0}^{d_1} c_I \, dxdy \tag{7.13}$$

in pentacene will be determined. The more H^+ ions are located in the pentacene the larger is the potential shift of the threshold voltage.

Tabelle 7.3: General parameters for the model

Parameter	Value
ε_{Penta} / $A^1s^1V^{-1}m^{-1}$	3.4
ε_{SiO2} / $A^1s^1V^{-1}m^{-1}$	4.5
ε_{SAM} / $A^1s^1V^{-1}m^{-1}$	4
d_1 / nm	35
d_2 / nm	147
l_k / μm	50
l_d / mm	7
U_S / V	0
U_D / V	-2
U_G / V	-60
$\triangle E$ /eV	0.47
c_{pi} / m^{-3}	$1 \cdot 10^{27}$
T / K	298.15
μ_{p0} / $m^2V^{-1}s^{-1}$	$2 \cdot 10^{-6}$
θ / eV	0.1
β / $eV(cm/V)^{1/2}$	$3.58 \cdot 10^{-5}$
γ / $(cm/V)^{1/2}$	$1 \cdot 10^{-4}$

7.3.1.1 Variation of H^+ Ion Mobility

Since the mobility of the H^+ ions is not known, the mobility is varied to study the effects in the simulation. The simulation based on the input parameters in Tab. 7.3, and Tab. 7.4. This raises the question how large the influence of the H^+ ion mobility on the process speed of space charge building is, and if it influences the threshold voltage. The shift of the threshold voltage in the experiment requires up to four weeks until a steady state is reached.

Tabelle 7.4: Parameters for the simulation of "Variation of the H^+ ion mobility "

Parameter	Value
μ_I / $m^2V^{-1}s^{-1}$	$1 \cdot 10^{-6} \ldots 1 \cdot 10^{-15}$
C_{I-SAM} / m^{-3}	$4 \cdot 10^{26}$

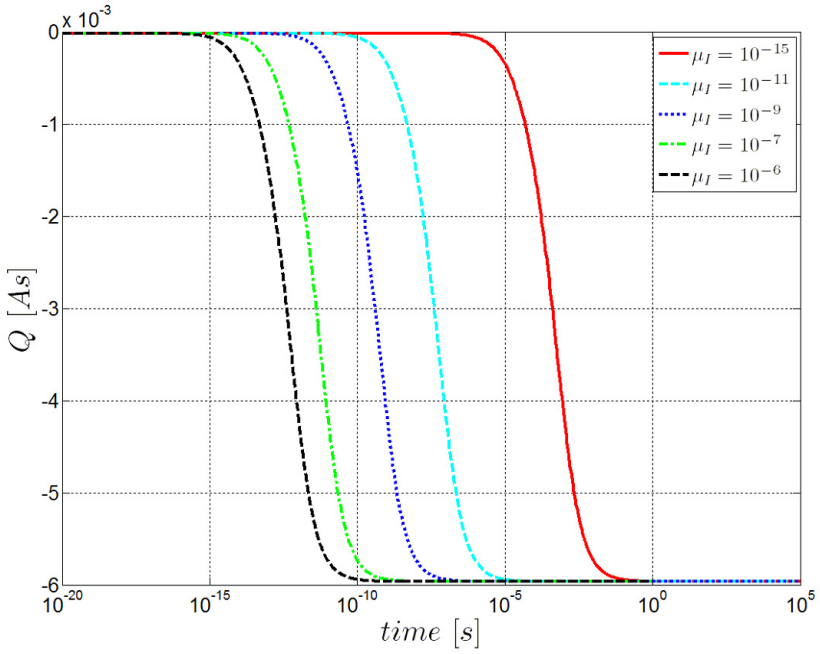

Fig. 7.7: Temporal formation of the ionic charge amount Q in pentacene for different H^+ ion mobilities with model 1.

As can be seen from Fig. 7.7, the amount of ionic charge Q in pentacene in the steady state is not affected by different H^+ ion mobilities. The H^+ ion mobility does not play a role for the period necessary to establish steady state, as can be seen out of Fig. 7.7, because the propagation time of the H^+ ions moved in the range of milliseconds. Even the unrealistic assumption of an extremely low mobility of $\mu_I = 10^{-15}\mathrm{m}^2\mathrm{V}^{-1}\mathrm{s}^{-1}$ leads to a process duration of a few milliseconds only.

7.3.1.2 Variation of the H^+ Ion Density in the SAM

Since the exact density of the freely moving H^+ ions in the SAM is unknown, the density of the H^+ ions in the SAM is varied to study the effects in the simulation. The simulation based on the input parameters in Tab. 7.3, and Tab. 7.5. The aim is to determine the H^+ ion density in the simulation, which reproduces the threshold voltage shift from the experiment. As one can see from Fig. 7.8, an increasing initial density c_{I-SAM} generates a rising amount of H^+ ions in the pentacene. A cut through the distribution of H^+ ions in pentacene in the steady state can be seen in Fig. 7.10. Fig 7.9 shows the position of the cut in the device. One can see that the main part of the H^+ ion is close to the SAM. A few nm away from the SAM, the density is to low to contribute significantly to the total amount of H^+ ions in pentacene. Therefore, the variation of the initial density c_{I-SAM} has practically no influence on the charge in pentacene. This is also reflected in a negligible threshold voltage shift as can be seen from Fig. 7.11. Even a highly unrealistic assumption of an initial density of $c_{I-SAM} = 32 \times 10^{26}$ leads only to a threshold voltage shift of about 6 V.

Tabelle 7.5: Parameters for the simulation "Variation of the H^+ ion density in the SAM "

Parameter	Value
U_s / V	0
U_d / V	-2
U_g / V	-60 ... +10
μ_I / $m^2V^{-1}s^{-1}$	$1 \cdot 10^{-7}$
C_{I-SAM} / m^{-3}	$1 \cdot 10^{26}$ ... $32 \cdot 10^{26}$

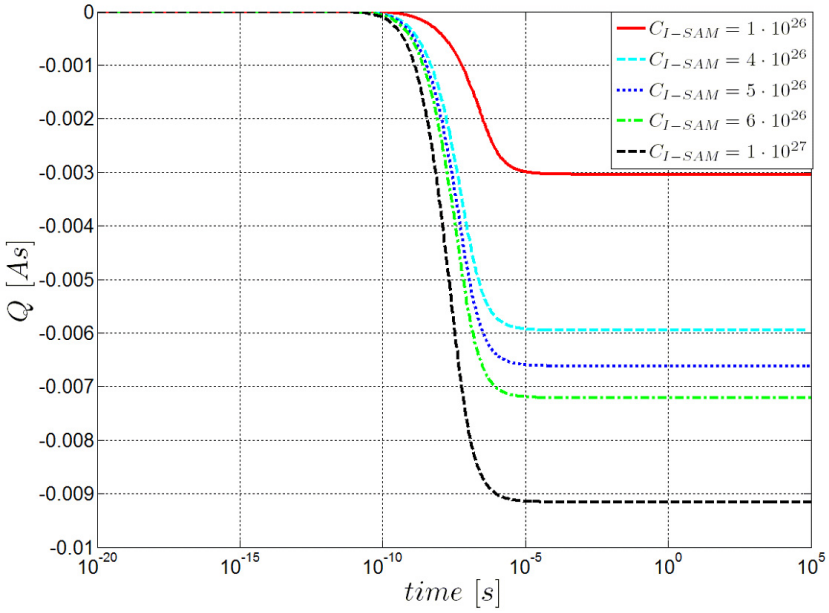

Fig. 7.8: Temporal formation of the ionic charge amount Q in pentacene for different initial densities c_{I-SAM} with model 1 at $U_G = -60$V.

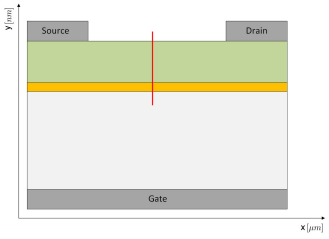

Fig. 7.9: Position of the cut through of the H^+ ion distribution in pentacene from Fig. 7.10.

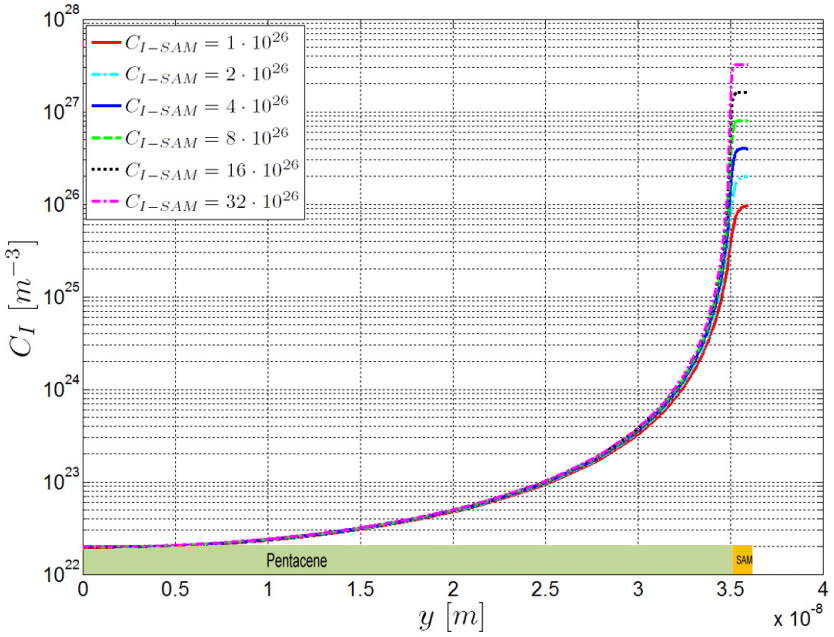

Fig. 7.10: Cut in the y direction through the H^+ ion distribution in pentacene and SAM. ($U_G = -60$V)

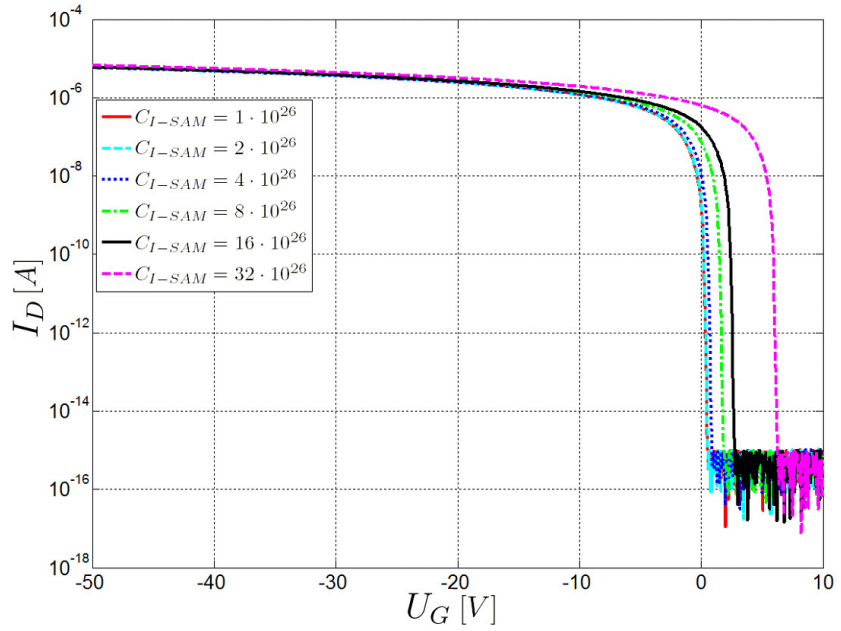

Fig. 7.11: Threshold voltage shift for different initial densities c_{I-SAM} with model 1

7.3.1.3 Evaluation of the Model

The simulations shows that this simple model is not suitable to reproduce the results. Even extremely high H^+ ion densities in the SAM did not lead to the measured threshold voltage shift. Realistically assumed H^+ ion densities in the SAM lead to a threshold voltage shift of less than one volt. According to measurements, however, a threshold voltage shift arising from approximately 60 V.

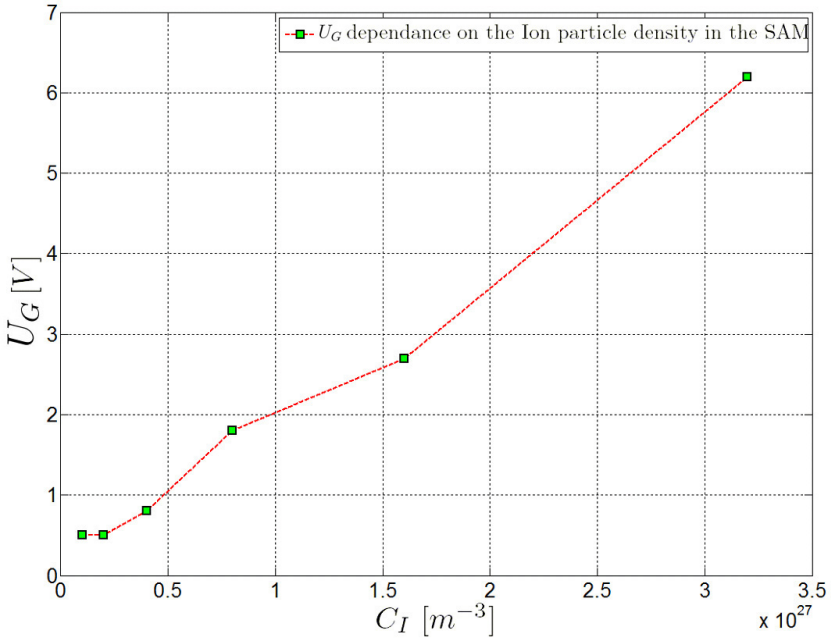

Fig. 7.12: Dependence of the threshold voltage shift from the initial density c_{I-SAM} in the SAM with model 1.

This means that the results can only be reproduced if the positive H^+ ions are neutralized by an initially undetermined process and leave behind a negatively charged layer at the SAM. The H^+ ions cannot escape, since they should have a vanishing vapor pressure in a solid. Moreover, such a hypothesis would be inconsistent with the measurement results of devices that have been exposed to NH_3. The threshold voltage shift upon neutralization by NH_3 could not be explained, because for the neutralization of the space charge layer the positive H^+ ions are required. If the H^+ ions would escape the device, they are no longer available for the neutralization process by NH_3. However, in the case that the H^+ ions remain in the pentacene, a sufficiently large negative space charge density can be achieved only if these H^+ ions are neutralized within the pentacene layer. In the following chapters, the current model is extended accordingly.

7.4 Model 2

In the first sub-section the model 2 of the organic thin film transistor is described briefly. Then the boundary conditions are fixed. The simulation results are presented in the third subsection. Chapter four deals with the evaluation of the simulation results.

Simulation Model: The Model 2 is based on the assumption that the H^+ ions are neutralized by protonation of pentacene [41]. When the H^+ ions protonate the pentacene it would arise a hole which ensures the charge neutrality. This process is also reversible and is, therefore, not in contradiction with the NH_3 measurements. If after the formation of a space charge layer a voltage is applied at the contacts, the holes can flow through the contacts and a negatively charged space charge layer remains in the SAM. This space charge layer caused the threshold voltage shift. To simulate this process it will be assumed that in pentacene a H^+ ion can be converted into an hole. The protonated pentacene molecule which is created in addition to the hole is not considered in this model because it is neutral and immobile. To incorporate this fact, Model 1 needs to be extended by a recombination term Γ. Based on (7.6) it results for the drift diffusion equation of the holes

$$\frac{\partial n_p(\mathbf{r},t)}{\partial t} = -\frac{1}{q}\nabla \mathbf{J}_p(\mathbf{r},t) + \Gamma_p(\mathbf{r},t) \tag{7.14}$$

with

$$\Gamma_p(\mathbf{r},t) = k_1 c_I(\mathbf{r},t) - k_2 n_p(\mathbf{r},t) \tag{7.15}$$

as recombination term. k_1 and k_2 denotes the still undefined rate coefficients. c_I denotes the H^+ ion concentration and n_p the hole concentration. Based on (7.7) it results

$$\frac{\partial c_I(\mathbf{r},t)}{\partial t} = -\frac{1}{q}\nabla \mathbf{J}_I(\mathbf{r},t) + \Gamma_I(\mathbf{r},t) \tag{7.16}$$

for the drift diffusion equation of H^+ ions with

$$\Gamma_I(\mathbf{r},t) = -k_1 c_I(\mathbf{r},t) + k_2 n_p(\mathbf{r},t) \tag{7.17}$$

as recombination term.

Boundary Conditions: The boundary conditions of the model 2 are identical to those of model 1 in Sec. 7.3

7.4.1 Simulation Results

This section presents the simulation results of Model 2. The section consists of six parts. In the first part the H^+ ion mobility is varied and the resulting changes are presented. In the second part, the hole mobility varied. In the third part the existing H^+ ion density

in the SAM is varied. Part four deals with the variation of the rate coefficient k_1. Part five deals with the variation of rate coefficient k_2 and in the last part of this section the simulation results are compared with the results of the measurements. All the general parameters for the model 2 are listed in Tab. 7.3.

7.4.1.1 Variation of H^+ Ion Mobility

Due to the changes from Model 1 to Model 2, we again vary the H^+ ion mobility to to see if the insights gained from model 1 are still valid. The simulation based on the input parameters in Tab. 7.3, and Tab. 7.6.

Tabelle 7.6: Parameters for the simulation "Variation of H^+ ion mobility "

Parameter	Value
μ_I / $m^2V^{-1}s^{-1}$	$1 \cdot 10^{-9} \ldots 1 \cdot 10^{-15}$
C_{I-SAM} / m^{-3}	$4 \cdot 10^{26}$
k_1 / s^{-1}	$1 \cdot 10^{-5}$
k_2 / s^{-1}	$1 \cdot 10^{-8}$

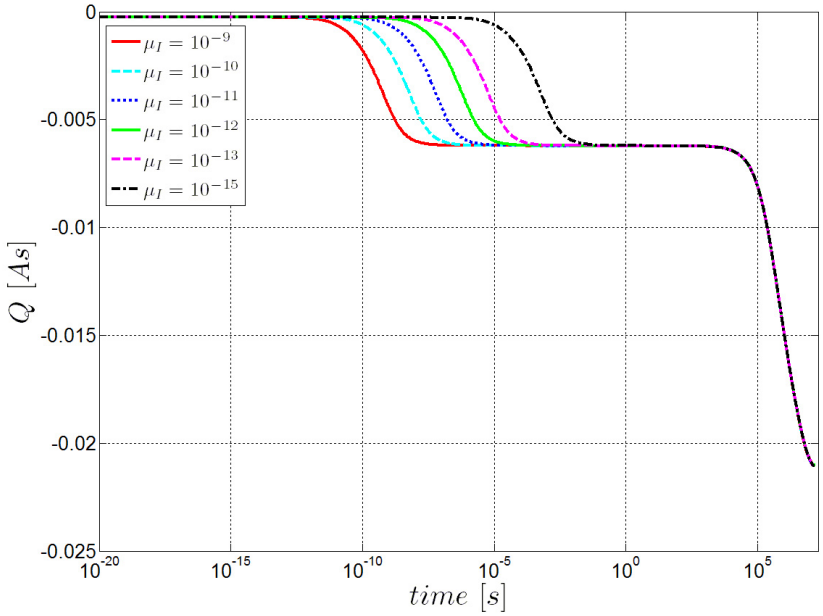

Fig. 7.13: Temporal formation of the ionic charge amount Q in pentacene for different H^+ ion mobilities with model 2 at $U_G = -60$V.

As can be seen from Fig. 7.13, the H^+ ion mobility still plays no role in building the space charge layer. A fundamental change is, however, the added possibility to convert H^+ ions into holes. Fig. 7.13 shows a significant increase in the H^+ ions density in pentacene compared to the situation described by Model 1 in Fig. 7.7. To calculate the

ionic charge Q in pentacene both the freely moving H^+ ions and the protonated H^+ ions were counted.

7.4.1.2 Variation of Hole Mobility

The hole mobility for the devices is known and is approximately 10^{-6} $m^2V^{-1}s^{-1}$. Nevertheless, the hole mobility was varied to investigate whether it has an impact on the simulation. The simulation based on the input parameters in Tab. 7.3, and Tab. 7.7.

Tabelle 7.7: Parameters for the simulation "Variation of hole mobility"

Parameter	Value
μ_I / $m^2V^{-1}s^{-1}$	$1 \cdot 10^{-7}$
C_{I-SAM} / m^{-3}	$4 \cdot 10^{26}$
μ_h / $m^2V^{-1}s^{-1}$	$1 \cdot 10^{-7}$ ... $1 \cdot 10^{-15}$
k_1 / s^{-1}	$1 \cdot 10^{+4}$
k_2 / s^{-1}	$1 \cdot 10^{+1}$

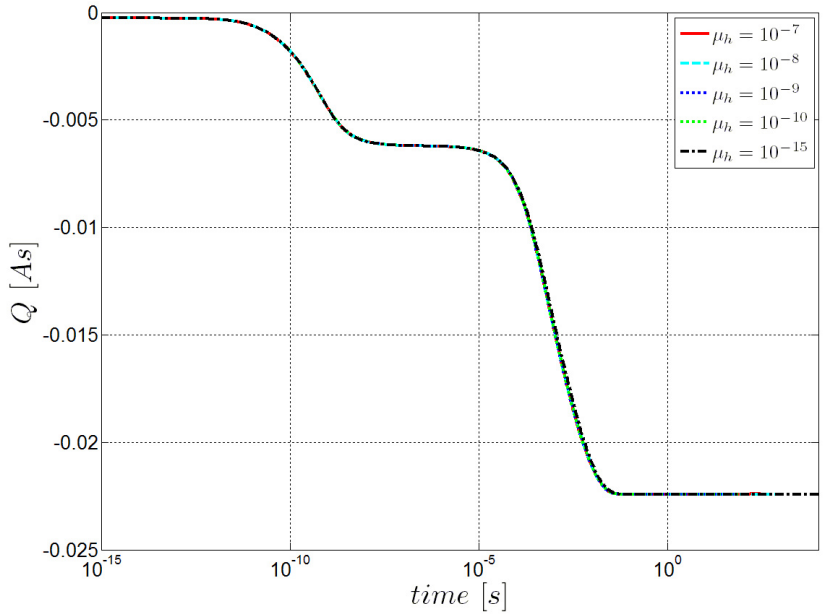

Fig. 7.14: Temporal formation of the ionic charge amount Q in pentacene for different hole mobilities with model 2 at $U_G = -60$V.

As can be seen in Fig. 7.14 the hole mobility has no influence on the ionic charge Q in pentacene and, therefore no influence on the formation of a space charge layer in the SAM.

7.4.1.3 Variation of the H^+ Ion Density in the SAM

The density c_{I-SAM} of the available H^+ ions in the SAM is varied as in Model 1. According to Fig. 7.15, the charge amount of H^+ ions in pentacene increases at the beginning similarly to the first model with increasing initial density c_{I-SAM}. After about 10^{-5} seconds a preliminary H^+ ion maximum is reached in pentacene. Until that time, Model 1 and Model 2 provide identical data. After about 10^2 seconds, the conversion of H^+ ions into holes shows an effect as can be seen from Fig. 7.16. This characteristic time constant depends of course on the rate coefficient. This coefficient was chosen so that the increase of the ionic charge in pentacene based on the protonated H^+ ions could be clearly separated from that H^+ ions which are present in the model 1. Fig. 7.15 shows, that a change in the H^+ ion density c_{I-SAM} has now much more significant effect on the ionic charge in pentacene and thus on the threshold voltage shift. The simulation based on the input parameters in Tab. 7.3, and Tab. 7.8.

Tabelle 7.8: Parameters for the simulation "Variation of the H^+ ion density in the SAM"

Parameter	Value
μ_I / $m^2V^{-1}s^{-1}$	$1 \cdot 10^{-7}$
C_{I-SAM} / m^{-3}	$4 \cdot 10^{26}$ ... $8 \cdot 10^{26}$
k_1 / s^{-1}	$1 \cdot 10^{-2}$
k_2 / s^{-1}	$1 \cdot 10^{-6}$

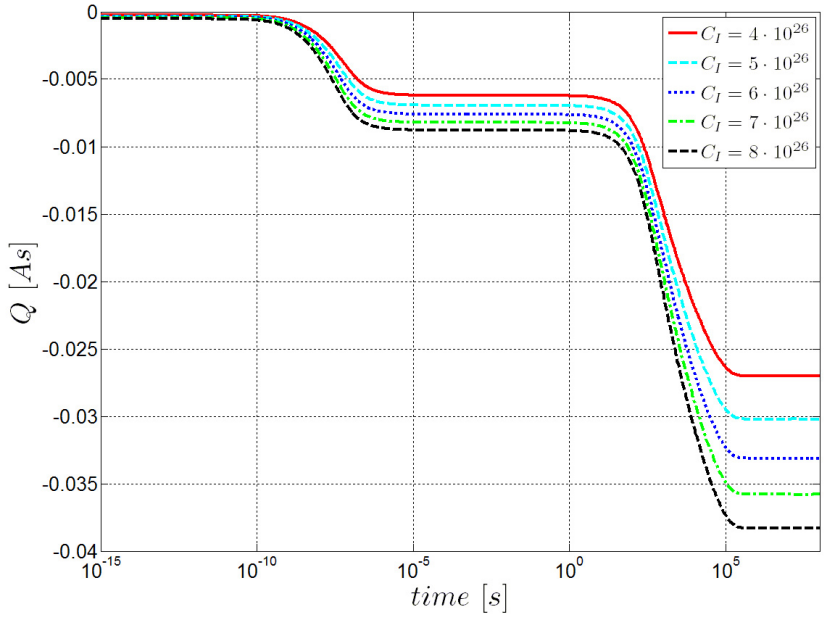

Fig. 7.15: Temporal formation of the ionic charge amount Q in pentacene for different initial densities c_{I-SAM} with model 2 at $U_G = -60$V.

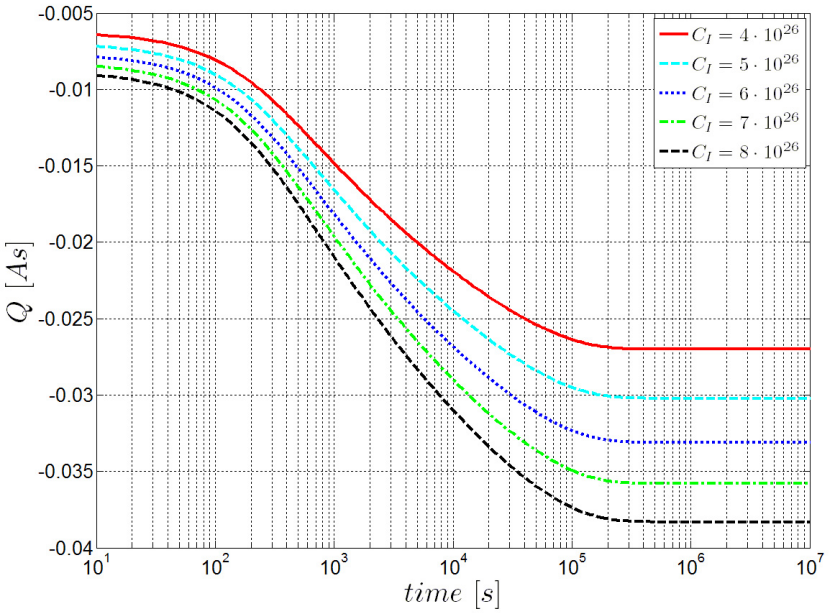

Fig. 7.16: Zoom from Fig. 7.15.

7.4.1.4 Variation of the Generation Coefficient k_1 for Protonated Pentacene

For the generation coefficient k_1 of holes we can make only a vague estimate due to the available measurements. To get more information it will be varied to possibly related effects. The simulation based on the input parameters in Tab. 7.3, and Tab. 7.9. If the ratio of k_1 to k_2 does not change as in this simulation, the amount of ionic charge Q in the steady state will be constant as seen from Fig. 7.17. As one would expect a variation of the coefficient generation k_1 changes only the time from when the conversion of H^+ ions into holes shows an effect. As seen in Fig. 7.17 for a generation coefficient of around $k_1 = 10^{-3}$ the construction of the space charge layer in the SAM needs about of two weeks. In the measurements we have such a behavior.

Tabelle 7.9: Parameters for the simulation "Variation of the generation coefficient k_1"

Parameter	Value
μ_I / $m^2V^{-1}s^{-1}$	$1 \cdot 10^{-7}$
C_{I-SAM} / m^{-3}	$4 \cdot 10^{26}$
μ_h / $m^2V^{-1}s^{-1}$	$1 \cdot 10^{-6}$
k_1 / s^{-1}	$1 \cdot 10^{-4}$ ... $1 \cdot 10^{+4}$
k_2 / s^{-1}	$k_1 \cdot 1 \cdot 10^{-4}$

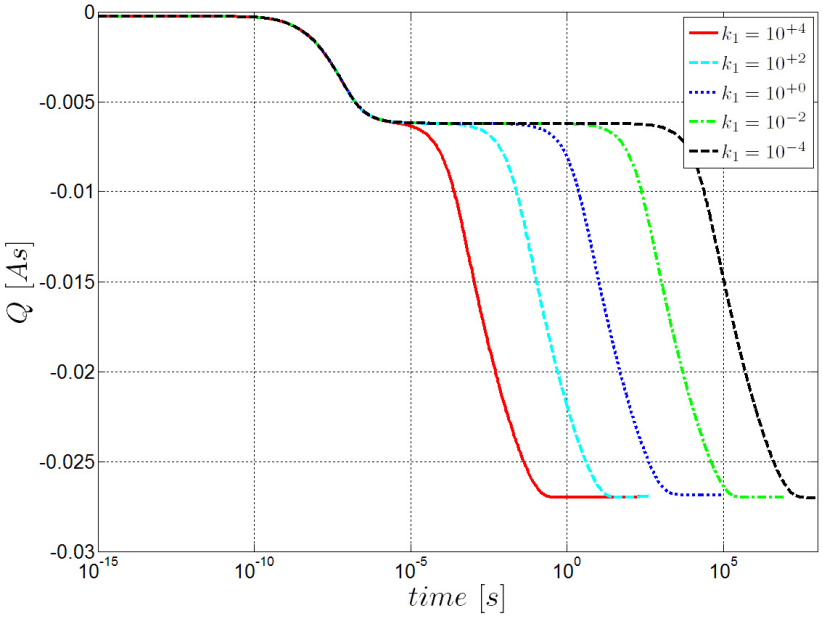

Fig. 7.17: Temporal formation of the ionic charge amount Q in pentacene for different generation coefficients k_1 with model 2.

7.4.1.5 Variation of the Recombination Coefficient k_2 for Protonated Pentacene

It should now be checked how much a change in the recombination coefficient k_2 effects the simulation results. The simulation based on the input parameters in Tab. 7.3, and Tab. 7.10. As seen in Fig. 7.18, a change in the ratio of k_1 to k_2 causes a change in the ionic charge Q in pentacene in the steady state. The larger k_2, the smaller is the H^+ ion charge in pentacene and thus the resulting threshold voltage shift. The time at which the H^+ ion conversion begins to play a role is not influenced by k_2 as one can see from Fig. 7.19.

Tabelle 7.10: Parameters for the simulation "Variation of the recombination coefficient k_2"

Parameter	Value
μ_I / $m^2V^{-1}s^{-1}$	$1 \cdot 10^{-7}$
C_{I-SAM} / m^{-3}	$4 \cdot 10^{26}$
μ_h / $m^2V^{-1}s^{-1}$	$1 \cdot 10^{-6}$
k_1 / s^{-1}	$1 \cdot 10^{-4}$
k_2 / s^{-1}	$1 \cdot 10^{-4}$ ... $1 \cdot 10^{-8}$

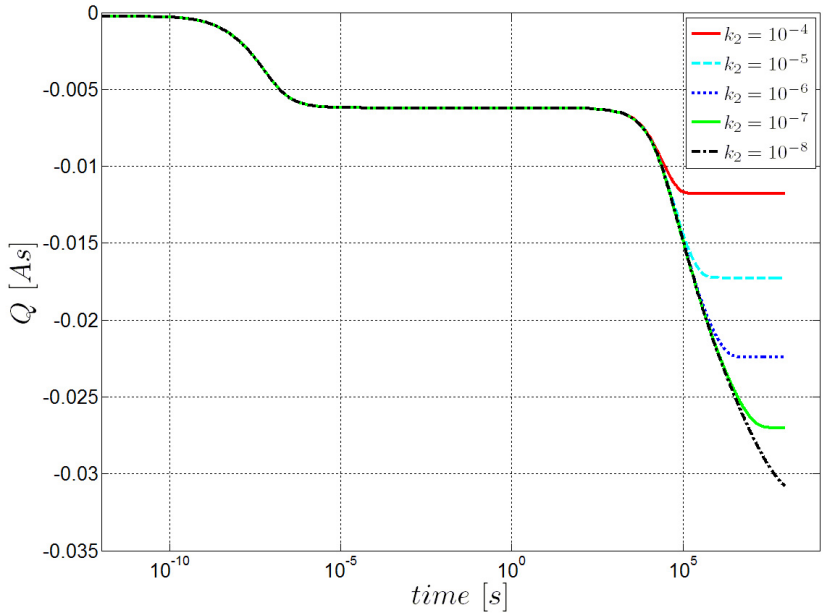

Fig. 7.18: Temporal formation of the ionic charge amount Q in pentacene for different recombination coefficient k_2 with model 2.

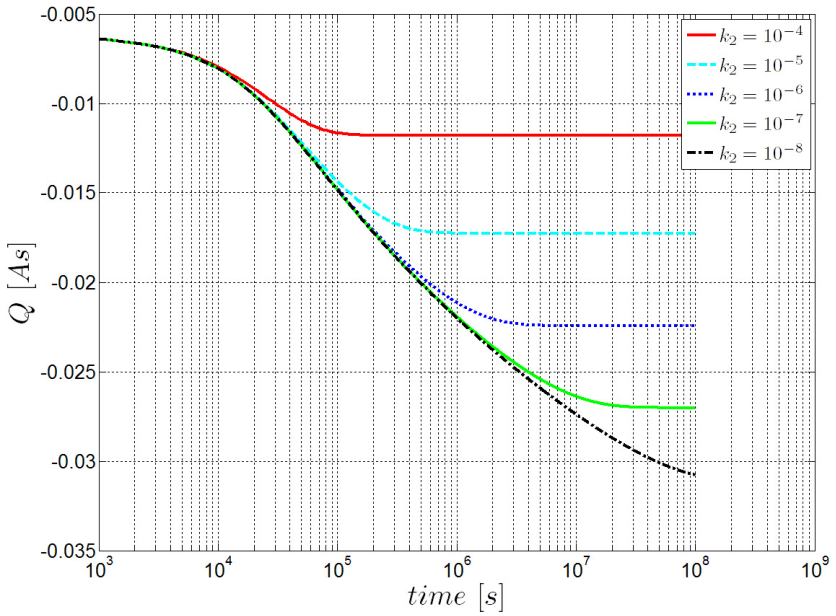

Fig. 7.19: Zoom from Fig. 7.18.

7.4.1.6 Evaluation of the Model

This model already provides far better simulation results, however, this model can not completely reproduce the measurements. Although it is possible with a suitable choice

of the generation coefficient k_1 to generate a similarly long duration of the space charge layer formation. Furthermore, it is also possible with the help of the recombination coefficient k_2 to get the desired amount of H^+ ions into the pentacene to reach the measured threshold voltage shift. Such a parameter set, independent of the physical meaningfulness, is not possible because the measurements with NH_3 show, that the threshold voltage shift can be fed back in a few seconds. If the generation coefficient k_1 and the recombination coefficient k_2 would be selected so that the measurements for the formation of space charge layer is fulfilled, the reduction of the space charge layer with NH_3 would also be in the range of weeks. The time limiting factor may not be in pentacene. Realistically, a slow generation of the H^+ ions take place in the SAM. This has been neglected in the current model. The Model 2 also neglected the protonated pentacene by the direct conversion of H^+ ions into holes. This leads to high conversation rates in the near of the interface which could correspond to unrealistic high protonated pentacene amounts at this point. For this reason, in Model 3, the protonated pentacene considered explicitly to ensure physical processes.

7.5 Model 3

In the first sub-section model 3 of the organic thin film transistor is described briefly. Then the boundary conditions are fixed. The simulation results are presented in the third subsection. Subsection four deals with the evaluation of the simulation results.

Simulation Model: Based on model 2 the protonated pentacene particles must be installed into the simulation to ensure physical processes. This is achieved with neutral pentacene particles with the concentration $c_{penta} = c_{DoPentaMax}$ and neutral protonated pentacene particles with the concentration $c_{DoPenta} = 0$. The protonated pentacene particle density can be estimated by assuming that 0.1 to a maximum of one pentacene molecule per nm^2 is protonated. This assumption leads to a maximum density of protonation $c_{DoPentaMax}$ of around 10^{26} m^{-3} up to a maximum of 10^{27} m^{-3}. Both pentacene and protonated pentacene particles are at rest and electrically neutral and, therefore, do not affect the electric potential. The problem is thus reduced to a simple rate equation (see Sec. 3.3):

$$\frac{\partial c_{penta}(\mathbf{r},t)}{\partial t} = \Gamma_I(\mathbf{r},t) \tag{7.18}$$

and

$$\frac{\partial c_{DoPenta}(\mathbf{r},t)}{\partial t} = -\Gamma_I(\mathbf{r},t). \tag{7.19}$$

Now a conversion of an H^+ ion in a hole depends on the concentration c_{penta}. To achieve that this conversion depends on the concentration c_{penta} the recombination term Γ_p, (7.15), has to be extended to

$$\Gamma_p(\mathbf{r},t) = k_1 c_I(\mathbf{r},t) c_{penta}(\mathbf{r},t) - k_2 n_p(\mathbf{r},t) c_{DoPenta}(\mathbf{r},t). \tag{7.20}$$

The recombination Γ_I from (7.17) is also extended to

$$\Gamma_I(\mathbf{r},t) = -k_1 c_I(\mathbf{r},t) c_{penta}(\mathbf{r},t) + k_2 n_p(\mathbf{r},t) c_{DoPenta}(\mathbf{r},t). \tag{7.21}$$

Boundary Conditions: The boundary conditions of the model 3 are identical to those of model 1 in Sec. 7.3

7.5.1 Simulation Results

This section presents the simulation results of Model 3. The section consists of to parts. In the first part, the maximum concentration of protonated pentacene is varied and the resulting changes are presented. In the second part, the simulation results are compared with the results of the measurements. All the general parameters for the model 3 are listed in Tab. 7.3.

7.5.1.1 Variation of the Maximum Concentration of Protonated Pentacene

At this stage we do not known exactly at which position the H^+ ion dock on the pentacene molecule and if it is possible that more than one H^+ ions can dock on a pentacene molecule. Therefore, it is not possible to specify an exact maximum concentration of protonated pentacene. So we vary the parameter to determine how big the effects are in the simulation. As one can see from Fig. 7.20, the effect of the variation is not high. The value of $c_{DoPentaMax}$ can be varied over a range of $10^{27}\ \frac{1}{m}$ up to $10^{25}\ \frac{1}{m}$ without incurring any inconsistence. An effect which should be considered is, however, a slower process speed as seen in Fig. 7.21. At the beginning enough protonated pentacene molecules are near the interface, later on the H^+ ions have to penetrate further into the pentacene in order to find unprotonated pentacene molecules. And this slows down the process speed. The simulation is based on the input parameters in Tab. 7.3, and Tab. 7.11.

Tabelle 7.11: Parameters for the simulation "Variation of the maximum concentration of doped pentacene"

Parameter	Value
μ_I / $m^2V^{-1}s^{-1}$	$1 \cdot 10^{-7}$
C_{I-SAM} / m^{-3}	$4 \cdot 10^{26}$
μ_h / $m^2V^{-1}s^{-1}$	$1 \cdot 10^{-9}$
k_1 / m^3s^{-1}	$1 \cdot 10^{-26}$
k_2 / m^3s^{-1}	$1 \cdot 10^{-30}$
$C_{DoPentaMax}$ / m^{-3}	$1 \cdot 10^{25} \ldots 1 \cdot 10^{27}$

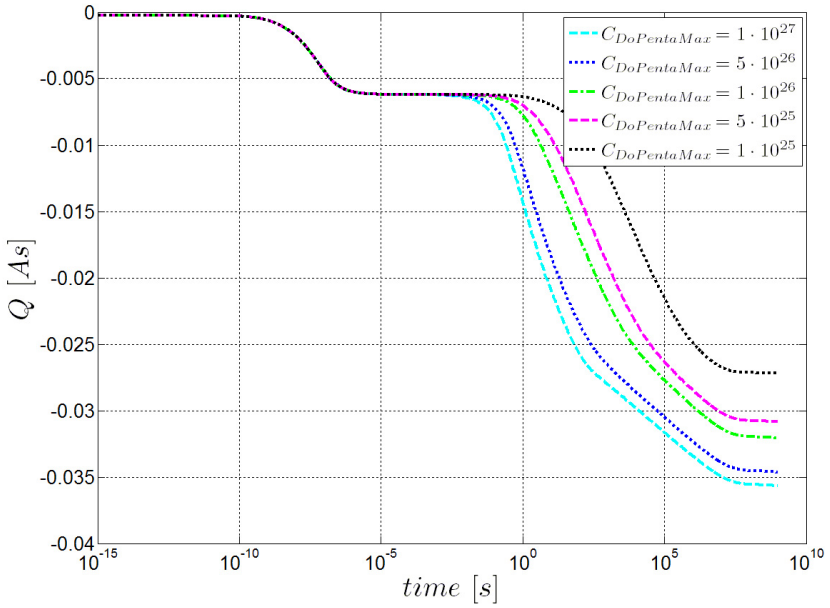

Fig. 7.20: Temporal formation of the ionic charge amount Q in pentacene for different maximum concentration of protonated pentacene with model 3.

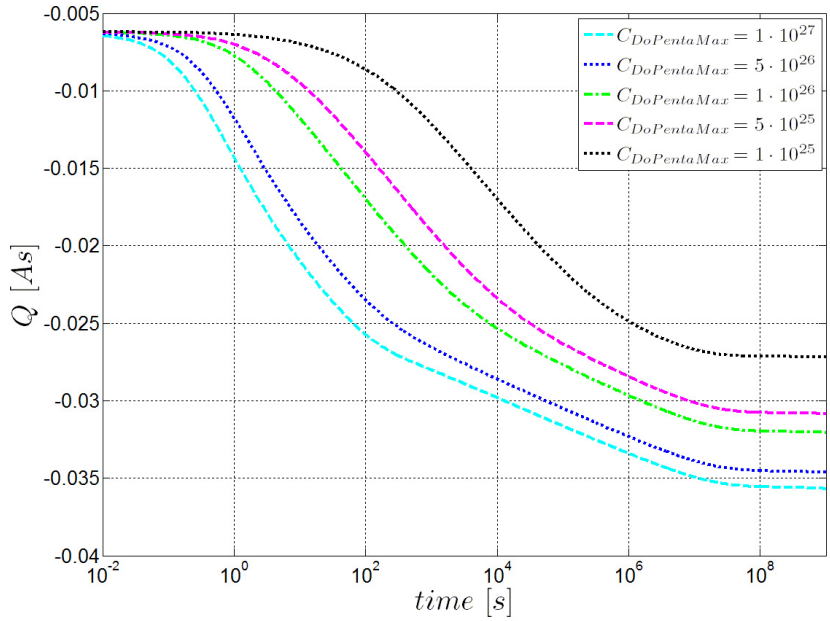

Fig. 7.21: Zoom from Fig. 7.20.

7.5.1.2 Evaluation of the Model

The explicit consideration of the pentacene particles did not yield any significant changes in the simulation behave. Slowing down the process flow is going in the right direction

but is still far too little to explain the long duration of the space charge layer formation. Thus, we additionally have to take into account the deprotonation of the sulfonic acid groups of the T-SA molecules in the SAM.

7.6 Model 4

In the first subsection model 4 of the organic thin film transistor is described briefly. Then the boundary conditions are fixed. The simulation results are presented in the third subsection. Subsection four deals with the evaluation of the simulation results.

Simulation Model: To explain the long duration of the the space charge layer formation, the decay process of sulfonic acid groups in the T-SA molecules must be considered. Since the chemical processes in the SAM during the decay is not well known, this process again is described with rate equations (see Sec. 3.3). Therefore, we start from a constant density of sulfonic acid groups c_{SAG} instead of a constant H^+ ion density c_{I-SAM} in the SAM. These sulfonic acid groups are now described by a rate equation to decay with the generation coefficient k_3 into negative H^+ ions and a fixed rest with the density c_r. The recombination coefficient k_4 enables us to recover the initial particles from H^+ ions and the negative residual.

The resulting rate equations are

$$\frac{\partial c_{SAG}(\mathbf{r},t)}{\partial t} = -k_3 c_{SAG}(\mathbf{r},t) + k_4 c_r(\mathbf{r},t) \tag{7.22}$$

$$\frac{\partial c_r(\mathbf{r},t)}{\partial t} = k_3 c_{SAG}(\mathbf{r},t) - k_4 c_r(\mathbf{r},t) \tag{7.23}$$

for the two kinds of particles in the SAM. The recombination term for the H^+ ions in the SAM results in

$$\Gamma_I(\mathbf{r},t) = k_3 c_{SAG}(\mathbf{r},t) - k_4 c_r(\mathbf{r},t). \tag{7.24}$$

Boundary Conditions: The boundary conditions of the model 4 are identical to those of model 1 in Sec. 7.3

7.6.1 Simulation Results

This section presents the simulation results of Model 4. The chapter consists of six parts. In the first part the generation coefficient k_1 is varied and the resulting changes are presented. Afterwards the H^+ ion generation coefficient k_3 is varied. In the third part the recombination coefficient k_4 for H^+ ions in the SAM is varied. Then the parameters are optimized to the measured displacement. In part five, the threshold voltage shift for different oxide thicknesses is studied. In the last part of this section, the simulation results are compared with the results of the measurements. All the general parameters for the model 4 are listed in Tab. 7.3.

7.6.1.1 Variation of the Generation Coefficient k_1 for Protonated Pentacene

For the extension of the model it is necessary to vary the generation coefficient k_1 to see if there are changes in the behavior of the model. The simulation is based on the input parameters in Tab. 7.3, and Tab. 7.12. As can bee seen in Fig. 7.22, the first increase of the ionic charge in pentacene vanishes. This is because at the beginning of the simulation free H^+ ions do not exist, they must be generated with the help of the generation coefficient k_3 from the sulfonic acid groups. Also the second increase of the ionic charge due to deprotonation of pentacene occurs later. As one can see in Fig. 7.23, the variation of the generation coefficient k_1 has no effect until the formation of H^+ ions from the sulfonic acid groups expires slower.

Tabelle 7.12: Parameters for the simulation "Variation of the generation coefficient k_1"

Parameter	Value
μ_I / $m^2V^{-1}s^{-1}$	$1 \cdot 10^{-7}$
C_{SAG} / m^{-3}	$4 \cdot 10^{26}$
μ_h / $m^2V^{-1}s^{-1}$	$1 \cdot 10^{-9}$
$C_{DoPentaMax}$ / m^{-3}	$5 \cdot 10^{26}$
k_1 / m^3s^{-1}	$1 \cdot 10^{-21} \ldots 1 \cdot 10^{-27}$
k_2 / m^3s^{-1}	$k_1 \cdot 10^{-4}$
k_3 / s^{-1}	$1 \cdot 10^{-7}$
k_4 / s^{-1}	$1 \cdot 10^{-10}$

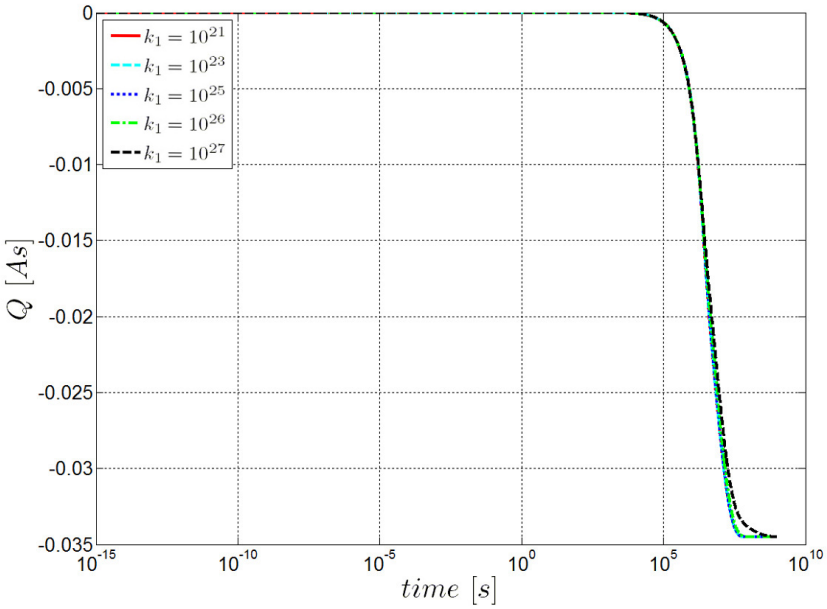

Fig. 7.22: Temporal formation of the ionic charge amount Q in pentacene for different generation coefficient k_1 with model 4.

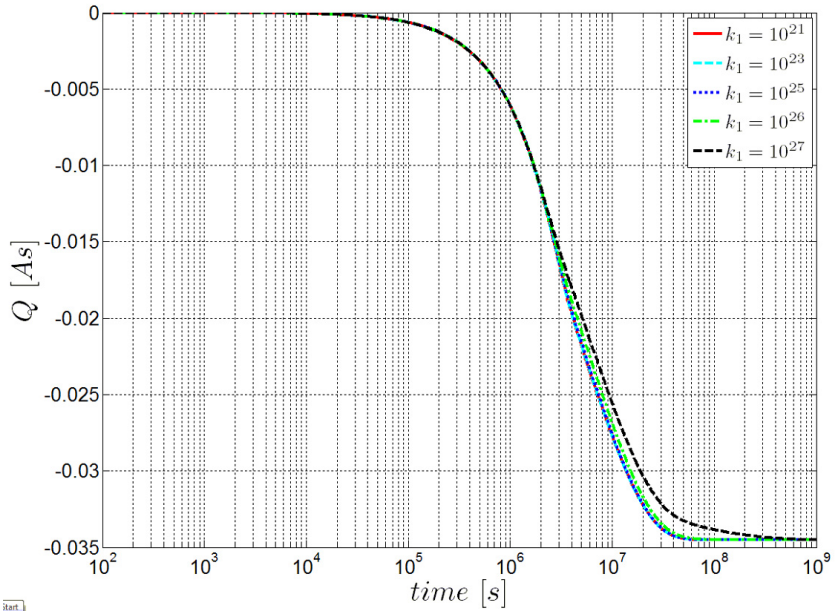

Fig. 7.23: Zoom from Fig. 7.22.

7.6.1.2 Variation of the Generation Coefficient k_3 for H^+ Ions in the SAM

Since the deprotonation of pentacene is not the time limiting factor (see the previous subsection), it remains only the generation coefficient k_3 for H^+ ions to cause the duration. With a variation of the generation coefficient k_3, followed by a comparison with the measured data, it should be possible to determine the generation coefficient k_3. The simulation is based on the input parameters in Tab. 7.3, and Tab. 7.13. As one can see from Fig. 7.24 an increase in the generation coefficient k_3 leads to an acceleration of the process flow. From the point at which the H^+ ion generation is faster than the absorption in pentacene, model 4 is equivalent to model 3. From the measurements we now that the space charge layer has completely formed out after about two weeks ($\approx 1.2 \times 10^6$ seconds). To achieve such a behavior, the generation coefficient k_3 has to be in the order of 10^{-6} s^{-1}, see Fig. 7.25. Since a chemical decomposition process is simulated, such a value of k_3 seems to be not impossible.

Tabelle 7.13: Parameters for the simulation "Variation of the generation coefficient k_3 for Ions"

Parameter	Value
μ_I / $m^2V^{-1}s^{-1}$	$1 \cdot 10^{-7}$
C_{SAG} / m^{-3}	$4 \cdot 10^{26}$
μ_h / $m^2V^{-1}s^{-1}$	$1 \cdot 10^{-9}$
$C_{DoPentaMax}$ / m^{-3}	$5 \cdot 10^{26}$
k_1 / m^3s^{-1}	$1 \cdot 10^{-26}$
k_2 / m^3s^{-1}	$1 \cdot 10^{-30}$
k_3 / s^{-1}	$1 \cdot 10^{-7} \ldots 1 \cdot 10^{+3}$
k_4 / s^{-1}	$k_3 \cdot 10^{-3}$

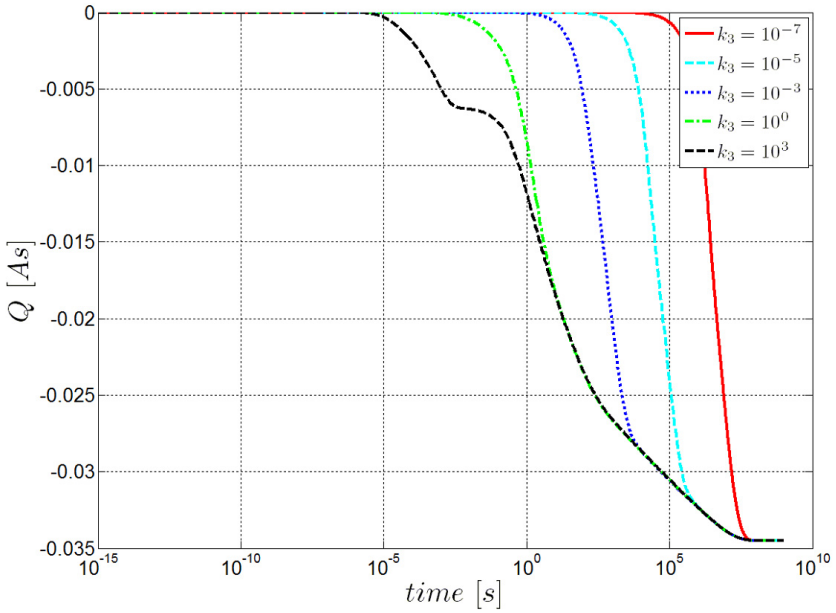

Fig. 7.24: Temporal formation of the ionic charge amount Q in pentacene for different generation coefficient k_3 with model 4.

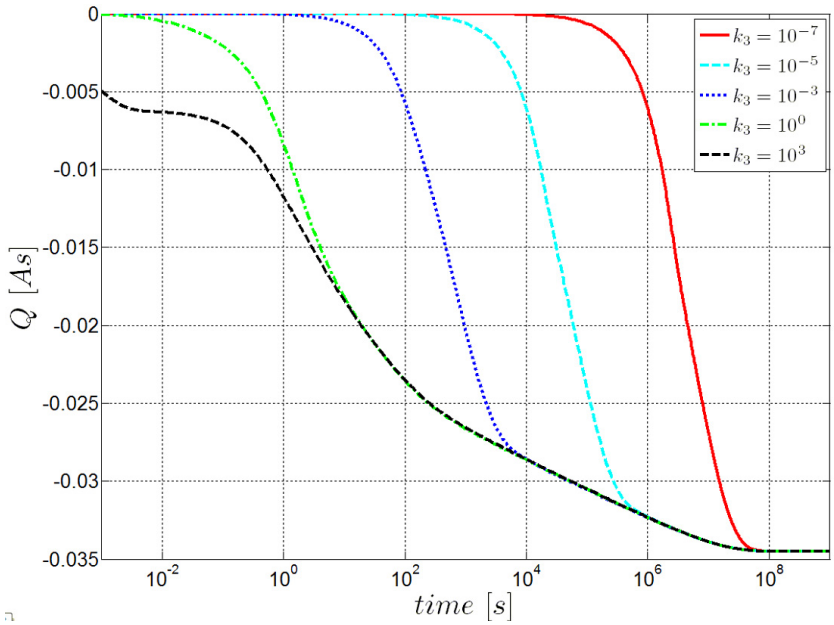

Fig. 7.25: Zoom from Fig. 7.24.

7.6.1.3 Variation of the Recombination Coefficient k_4 for H^+ Ions in the SAM

In this section, the effect of the recombination coefficient k_4 on the amount of ionic charge in pentacene is studied. The simulation is based on the input parameters in Tab. 7.3, and Tab. 7.14. As can be seen from Fig. 7.26, the ratio of generation coefficient to the recombination coefficient k_3/k_4 influences the ionic charge in pentacene significantly. A negligible recombination reproduces the charge amount of H^+ ions from the third model. But if the value of the recombination coefficient becomes comparible with the value of the generation coefficient, the magnitude of the ionic charge in pentacene decreases significantly. This has a direct impact on the threshold voltage shift. To explain the threshold voltage shift with an increasing recombination coefficient k_4 an increase of the sulfonic acid groups density c_{SAG} is necessary. Consequently, the two parameters are not independent of each other. Since neither of the two parameters is accurately determined by measurements, it is at this stage not possible to determine the exact value of both parameters.

Tabelle 7.14: Parameters for the simulation "Variation of the recombination coefficient k_4"

Parameter	Value
μ_I / $m^2V^{-1}s^{-1}$	$1 \cdot 10^{-7}$
C_{SAG} / m^{-3}	$4 \cdot 10^{26}$
μ_h / $m^2V^{-1}s^{-1}$	$1 \cdot 10^{-9}$
$C_{DoPentaMax}$ / m^{-3}	$5 \cdot 10^{26}$
k_1 / m^3s^{-1}	$1 \cdot 10^{-24}$
k_2 / m^3s^{-1}	$1 \cdot 10^{-28}$
k_3 / s^{-1}	$1 \cdot 10^{-7}$
k_4 / s^{-1}	$1 \cdot 10^{-15} \ldots 1 \cdot 10^{-7}$

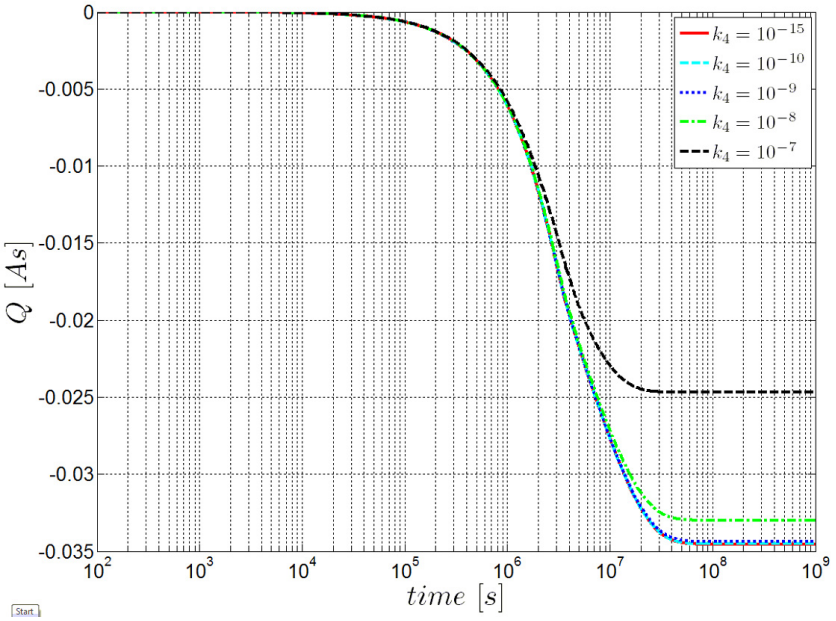

Fig. 7.26: Temporal formation of the ionic charge amount Q in pentacene for different recombination coefficient k_4 with model 4.

7.6.1.4 Optimizing the Parameters to the Measured Displacement

In this section, different parameter sets are tested concerning the threshold voltage shift to filter out the parameter combinations which agree to the measurement results. The simulation based on the input parameters in Tab. 7.3, and Tab. 7.15. Fig. 7.27 shows a threshold voltage shift with respect to all the simulated parameter combinations. For a 147 nm pentacene based organic thin-film transistor, the measurements yield a threshold voltage shift of 60 V (see Sec. 6.2). As it is evident from Fig. 7.28, with a density c_{SAG} less than 1×10^{26} m^{-3} no combination of the remaining simulation parameters k_1, k_2, k_3 and k_4 lead to a threshold voltage shift greater than 45 V. The density c_{SAG} must,

therefore, be larger than 1×10^{26} m^{-3}. For a sulfonic acid groups density c_{SAG} of 2×10^{26} m^{-3}, the parameter sets nine and eight produce a threshold voltage shift of about 60 V as one can see from Fig. 7.29. Both parameter sets are possible. At a sulfonic acid groups density c_{SAG} of 3×10^{26} m^{-3}, the parameter sets 13, 15, 18 and 22 provide a meaningful threshold voltage shift. This can be seen from Fig. 7.30. Parameter set 13 has a ratio k_1/k_2 and k_3/k_4 of one which seems to be reasonable. Parameter set 15 with a ratio k_1 to k_2 of 100 is still within the bounds of possibility. Parameter set 18 is due to the ratio of k_1/k_2 very unlikely. Parameter set 22 uses a ratio of $k_3/k_4 = 100$, which seems to be still possible. Fig. 7.31 shows that at a sulfonic acid group density of $c_{SAG} = 4 \times 10^{26}$ m^{-3} (parameter set 28) still provides the correct threshold voltage shift. Even this combination of parameters could not completely be excluded.

Tabelle 7.15: Parameters for the simulation "Optimizing the parameters to the measured displacement"

Parameter	C_{I-SAM}	k_1	k_2	k_3	k_4
Parameter Set 1	1E+26	1E-20	1E-20	1E-07	1E-07
Parameter Set 2	1E+26	1E-20	1E-21	1E-07	1E-07
Parameter Set 3	1E+26	1E-20	1E-20	1E-07	1E-08
Parameter Set 4	1E+26	1E-20	1E-21	1E-07	1E-08
Parameter Set 5	2E+26	1E-20	1E-20	1E-07	1E-07
Parameter Set 6	2E+26	1E-20	1E-21	1E-07	1E-07
Parameter Set 7	2E+26	1E-20	1E-20	1E-07	1E-08
Parameter Set 8	2E+26	1E-20	1E-21	1E-07	1E-08
Parameter Set 9	2E+26	1E-20	1E-21	1E-07	1E-09
Parameter Set 10	2E+26	1E-20	1E-22	1E-07	1E-09
Parameter Set 11	2E+26	1E-20	1E-22	1E-07	1E-10
Parameter Set 12	2E+26	1E-20	1E-23	1E-07	1E-10
Parameter Set 13	3E+26	1E-20	1E-20	1E-07	1E-07
Parameter Set 14	3E+26	1E-20	1E-21	1E-07	1E-07
Parameter Set 15	3E+26	1E-20	1E-22	1E-07	1E-07
Parameter Set 16	3E+26	1E-20	1E-23	1E-07	1E-07
Parameter Set 17	3E+26	1E-20	1E-24	1E-07	1E-07
Parameter Set 18	3E+26	1E-20	1E-25	1E-07	1E-07
Parameter Set 19	3E+26	1E-20	1E-26	1E-07	1E-07
Parameter Set 20	3E+26	1E-20	1E-20	1E-07	1E-08
Parameter Set 21	3E+26	1E-20	1E-21	1E-07	1E-08
Parameter Set 22	3E+26	1E-20	1E-20	1E-07	1E-09
Parameter Set 23	3E+26	1E-20	1E-21	1E-07	1E-09
Parameter Set 24	3E+26	1E-20	1E-22	1E-07	1E-09
Parameter Set 25	3E+26	1E-20	1E-20	1E-07	1E-10
Parameter Set 26	4E+26	0E+00	1E+00	1E-07	1E-08
Parameter Set 27	4E+26	1E-20	1E-20	1E-07	1E-07
Parameter Set 28	4E+26	1E-20	1E-21	1E-07	1E-07
Parameter Set 29	4E+26	1E-20	1E-20	1E-07	1E-08
Parameter Set 30	4E+26	1E-20	1E-21	1E-07	1E-08

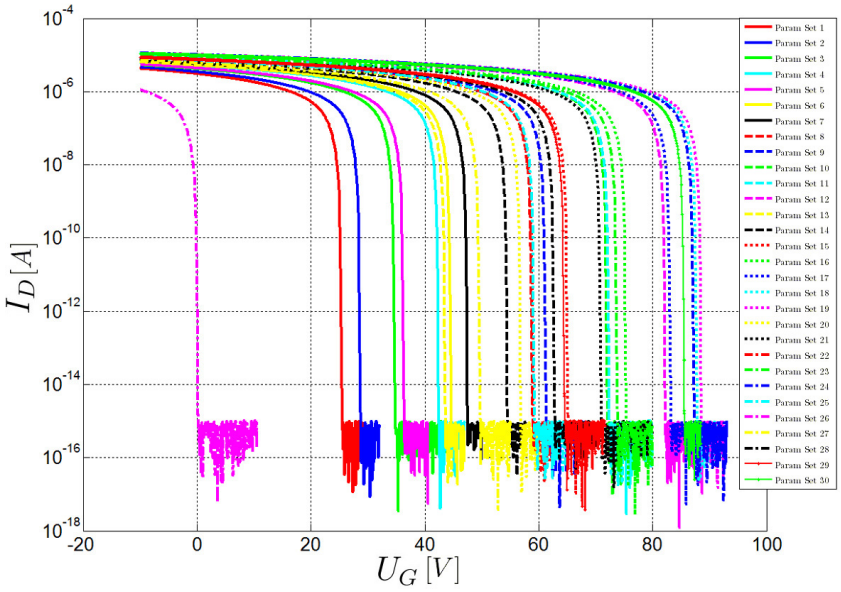

Fig. 7.27: Overview of the threshold voltage shift of all simulations.

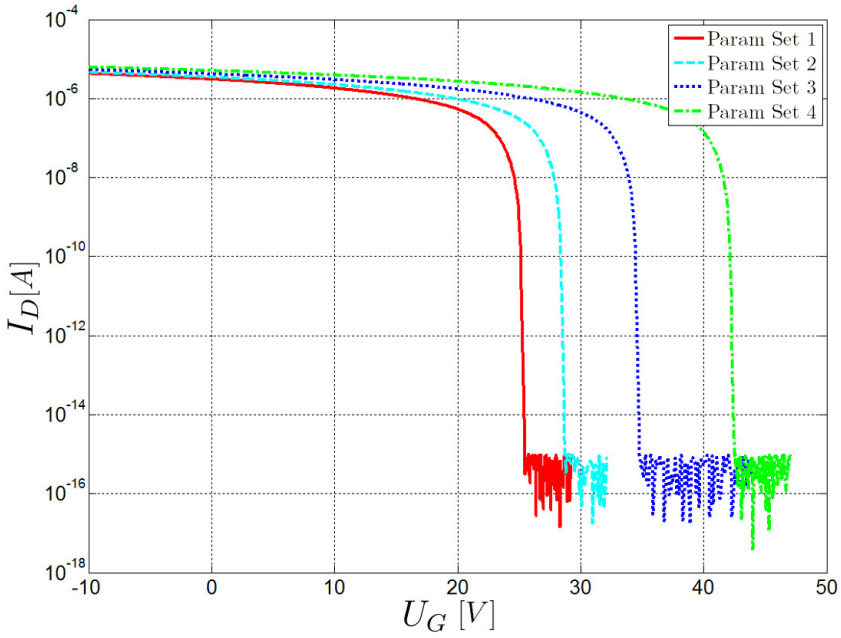

Fig. 7.28: Possible threshold voltage shift at a sulfonic acid groups density c_{SAG} of 1×10^{26} m^{-1}.

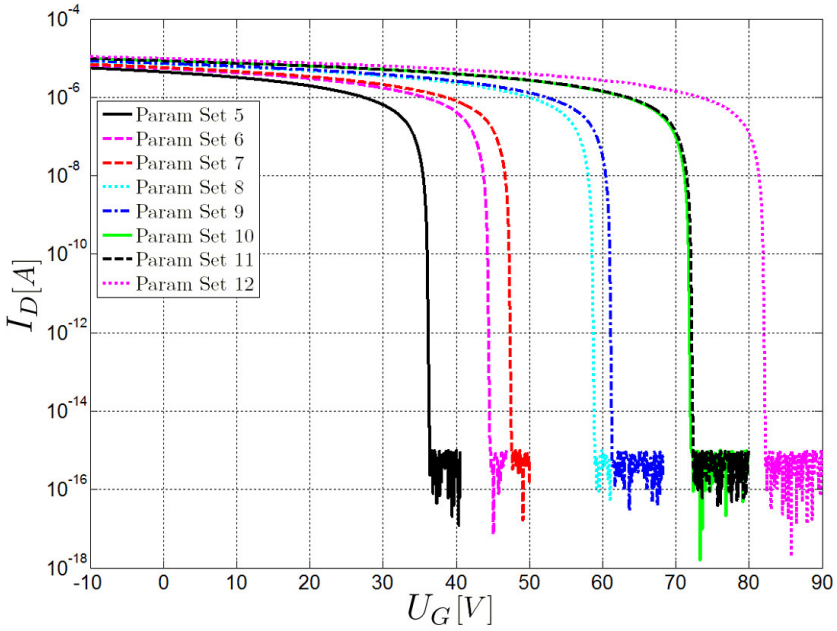

Fig. 7.29: Possible threshold voltage shift at a sulfonic acid groups density c_{SAG} of 2×10^{26} m^{-1}.

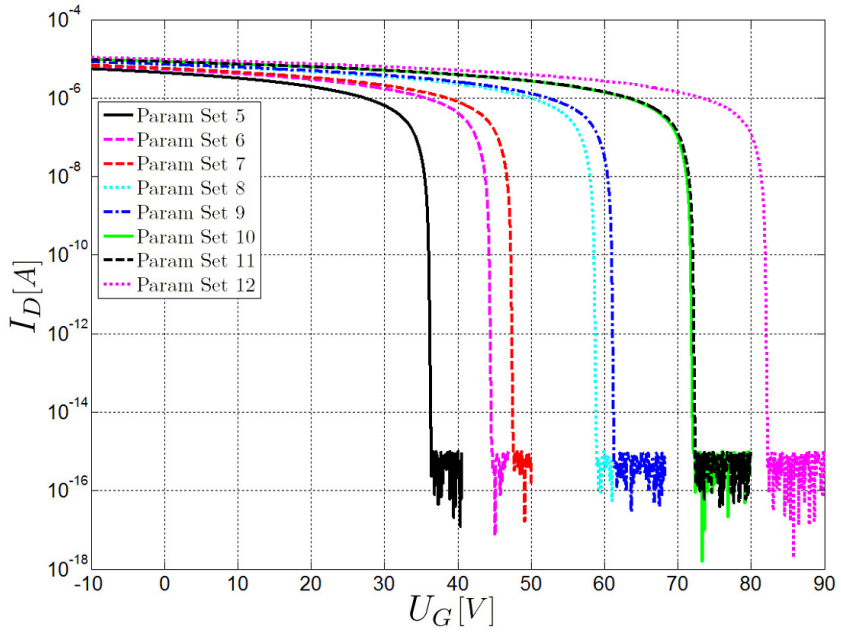

Fig. 7.30: Possible threshold voltage shift at a sulfonic acid groups density c_{SAG} of 3×10^{26} m^{-1}.

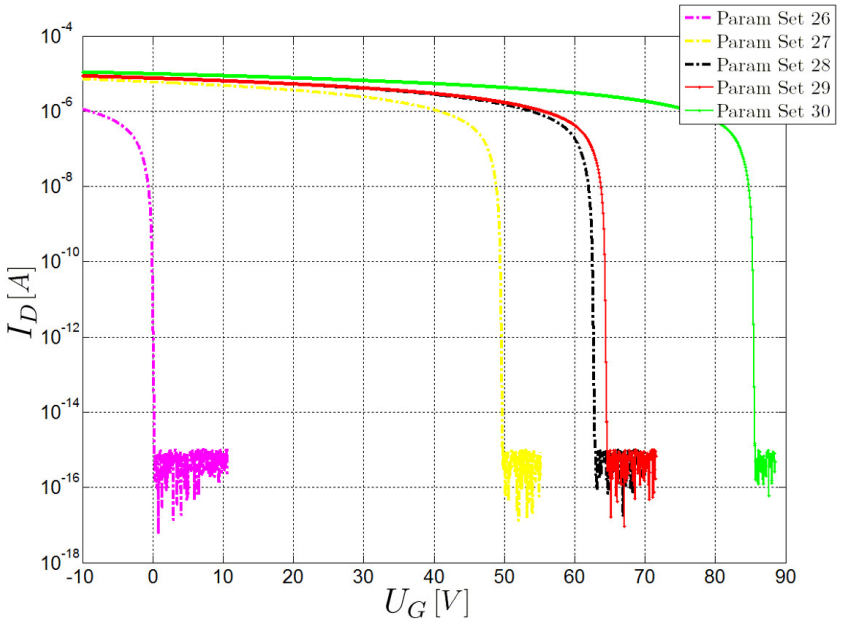

Fig. 7.31: Possible threshold voltage shift at a sulfonic acid groups density c_{SAG} of 4×10^{26} m^{-1}.

7.6.1.5 Comparison of the Shift of the Threshold Voltage for Different Oxide Thicknesses

In this subsection, the simulation model is applied to different oxide layer thicknesses. The results are compared with the available measured, values see Sec. 6.2. As shown in Fig. 7.32 the simulation model shows with increasing oxide thickness basically the same behavior as the measured results. The threshold voltage increases with increasing oxide thickness. For 245 nm oxide thickness there is a significant deviations of the simulation from the experimental result. The measured threshold voltage shift is around 30V greater than that of the simulation. This could be due to a yet unexplained dependence of the H^+ ions on the oxide thickness, but it could also be a parasitic effect caused through the different SiO_2 wafer. With measurements at only three oxide layer thicknesses, a parasitic effect cannot completely be excluded. An additional dipole of the protonated pentacene molecules could cause a further shift independence of oxide thickness. Throught such a shift, the measurement results could be reproduced, but due to the lack of different oxide layer thicknesses it is not entirely clear whether the increase of the threshold voltage is linear with increasind oxide thickness as predicted by the model, or not.

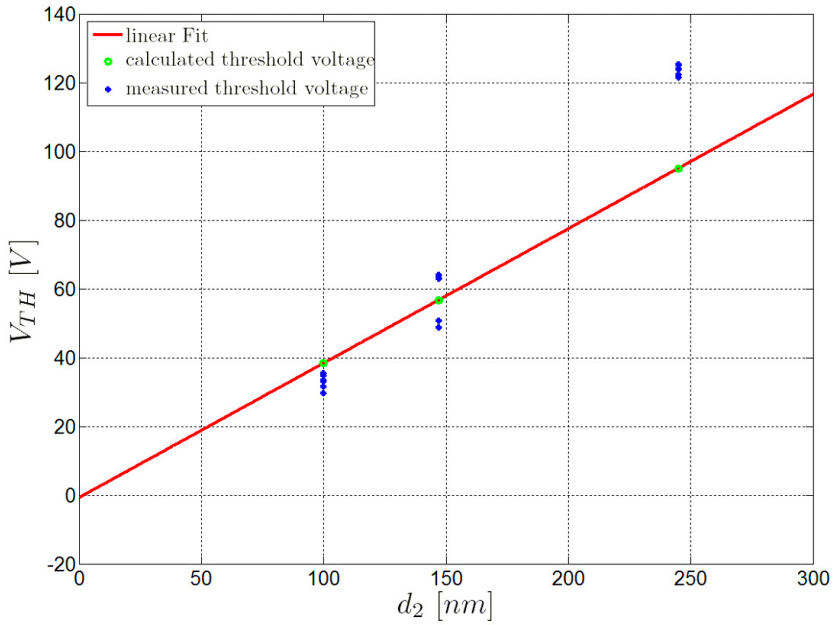

Fig. 7.32: Dependence of the threshold voltage shift on the oxide layer thickness d_2.

7.6.1.6 Evaluation of the Model

With this model it is possible to reproduce the experimental results. The problem of the previous models with the NH_3 test results could be solved, because now the chemical separation process of H^+ ions in the SAM causes the time delay. This makes it possible to adjust the pentacene trap rate k_1 to the NH_3 measurements without any adaption of the space charge layer formation. As can bee seen in Fig. 7.33, first the pentacene molecules near the interfaces become protonated. With advancing time, the protonation is more and more aligned. Finally in the steady state the protonated molecules are almost equally distributed over the entire device. Fig. 7.33 shows a cut through the channel in the y direction (see Fig. 7.9). According to the simulations, the threshold voltage shift dependence of the sulfonic acid groups density c_{SAG} is linear as shown in Fig. 7.34. The threshold voltage shift variation, due to a change of the ratio of k_1/k_2, is also linear in an range of one up to 10^4 as can be seen from Fig. 7.35. Thereafter the ionic charge go into saturation in pentacene. The ratio k_3/k_4 in contrast has not a linear behavior of the threshold voltage shift. Fig. 7.36 clearly shows a saturation for the ratio $k_3/k_4 > 10$. The maximum shift of the threshold voltage caused by changing the ratio of k_3/k_4 is 15 V as can be seen in Fig. 7.36. This is much less than the shift due to a change of the protonation-deprotonation ratio k_1/k_2. It could cause a shift variation of up to 40 V as can be seen in Fig. 7.35. We cannot say much about the quantity of the recombination coefficient k_3 with the currently available measurement results. Since the influence on the simulation is low, an exact determination is not very important.

We assumed that the H^+ ion production in the SAM is based on chemical pro-

cesses in which the activation energy must be overcome. Based on this assumption measurements with UV light could significantly accelerate the H^+ ion production rate. This would cause a change in the generation coefficient k_3 and, therefore, a change of the ratio k_3/k_4. After irradiation, the original threshold voltage shift should be reached again. With the help of these measurements it might be possible to estimated the recombination coefficient k_4. The storage of the devices in the dark would be also interesting, maybe that the H^+ ion generation and, therefore, the space charge formation is influenced. The recombination coefficient of k_2 can be estimated with the help of the NH_3 measurements. Therefore, it is necessary to expand the existing simulation model by a diffusion equation for NH_3 molecules.

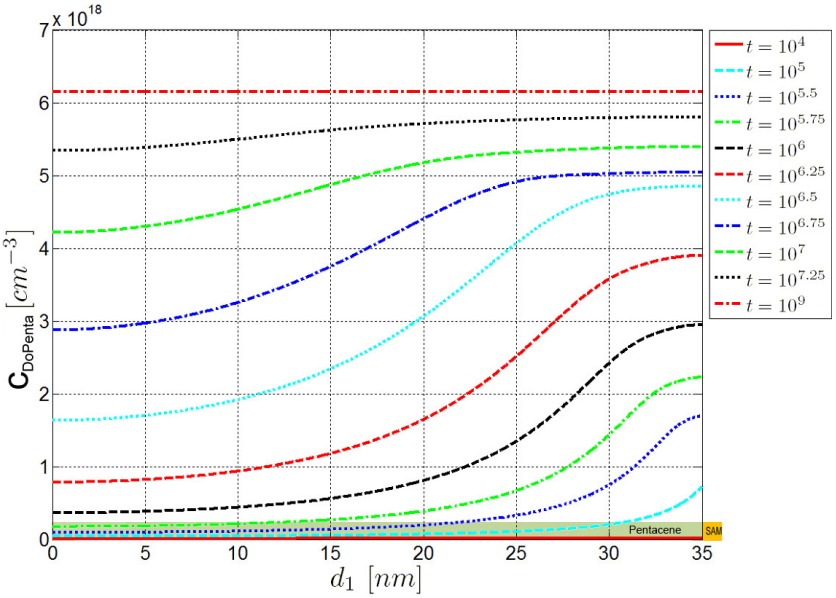

Fig. 7.33: Temporal evolution of the distribution of the protonated pentacene $c_{DoPenta}$.

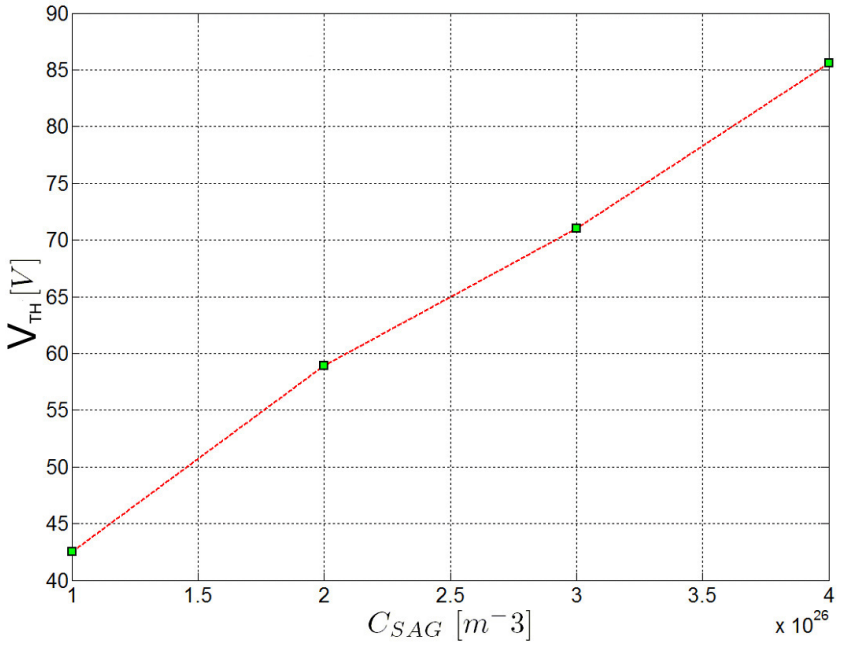

Fig. 7.34: Dependence of the threshold voltage V_{TH} from the sulfonic acid groups density c_{SAG}.

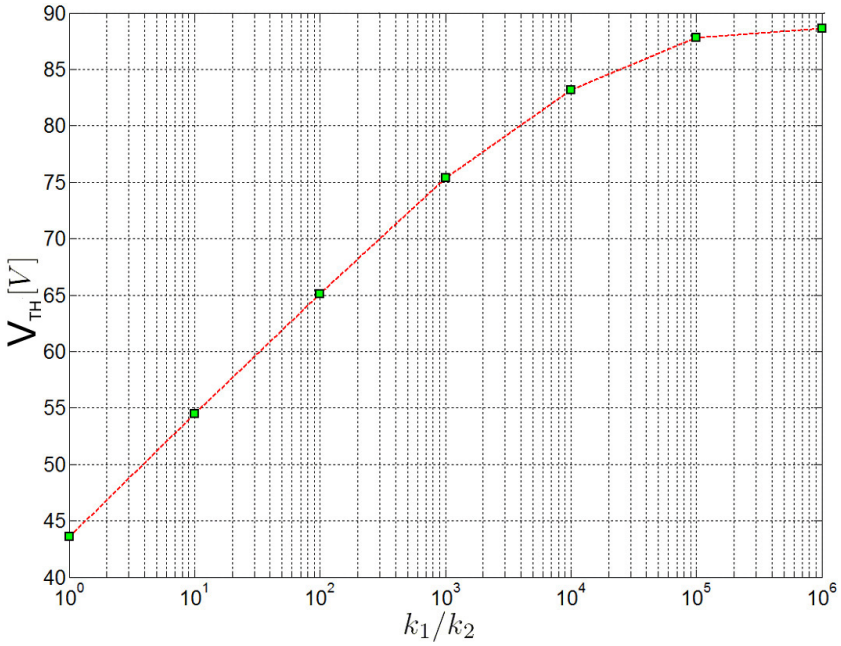

Fig. 7.35: Dependence of the threshold voltage V_{TH} from the generation recombination ratio k_1/k_2.

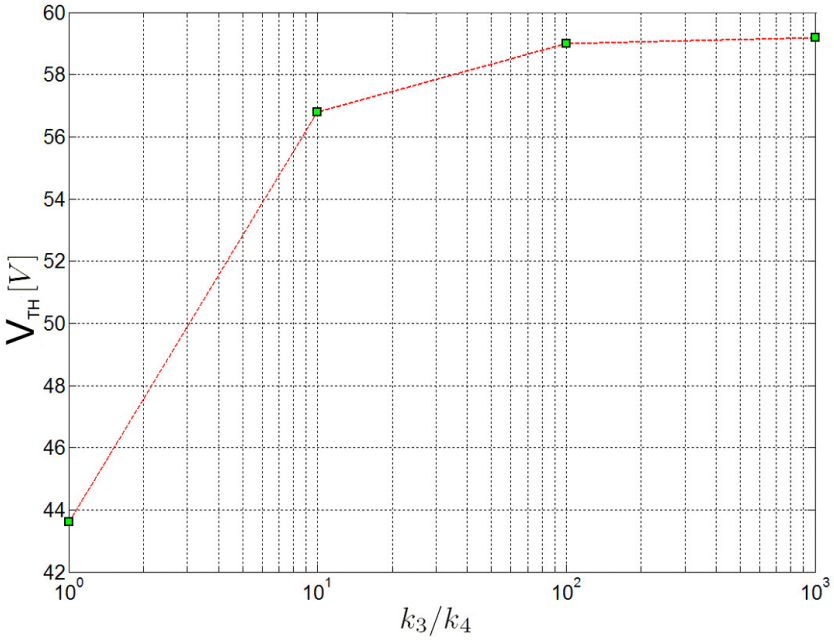

Fig. 7.36: Dependence of the threshold voltage V_{TH} from the generation recombination ratio k_3/k_4.

7.7 Model 5

The model 5 is concerned with the influence of NH_3 on the device. The first subsection, presents the description of model 5 to simulate the organic thin film transistor in an NH_3 environment. Then the boundary conditions are fixed. The simulation results are given in the third subsection. Subsection four deals with the evaluation of the simulation results.

Simulation Model: After the space charge layer formation, the device will be exposed to the NH_3 gas. To simulate this, the steady state result of Model 4 is set as the initial state. The NH_3 gas can diffuse into the pentacene through the contact surface C_a in Fig. 7.6. The NH_3 gas is electrically neutral and, therefore, does not affect the electric potential. We need only an additional diffusion equation (3.101) for the NH_3 concentration c_{NH_3} in the pentacene and SAM:

$$\frac{\partial c_{NH3}(\mathbf{r},t)}{\partial t} - \nabla(D_{NH3}\nabla c_{NH3}(\mathbf{r},t)) = \Gamma_{NH3}(\mathbf{r},t) \tag{7.25}$$

We assumed that the diffuion coefficient D_{NH3} for NH_3 molecules in pentacene and SAM is equivalent. Moreover, the NH_3 recombination term with the recombination coefficient k_5 has to be defined:

$$\Gamma_{NH3}(\mathbf{r},t) = -k_5 c_I(\mathbf{r},t) c_r(\mathbf{r},t) c_{NH3}(\mathbf{r},t) \tag{7.26}$$

In addition, an adaptation of the H^+ ion recombination term:

$$\Gamma_I(\mathbf{r},t) = k_3 c_{SAG}(\mathbf{r},t) - k_4 c_r(\mathbf{r},t) - k_5 c_I(\mathbf{r},t) c_r(\mathbf{r},t) c_{NH3}(\mathbf{r},t) \tag{7.27}$$

is necessary.

Boundary Conditions: For this simulation, the boundary conditions from Model 1 in Sec. 7.3 can be easily extended. It is assumed that the device is exposed to a uniformly distributed NH_3 concentration, therefore, for the interface air-pentacene C_a (Fig. 7.6), a Dirichlet boundary condition

$$c_{NH3}(x,y) = c_{NH3-Air} \text{ at } C_a \tag{7.28}$$

can be assumed. For the NH_3 molecules density in the air $c_{NH3-Air}$ a value of 1.2×10^{22} m^{-3} ($\approx$0.2 g/m^3) is fixed. For the NH_3 molecules the interface SAM $-$ SiO_2 provides a barrier, therefore,

$$\frac{\partial c_{NH3}(x,y)}{\partial y} = 0 \text{ at } C_h \tag{7.29}$$

holds. For the lateral boundaries C_b,C_f and C_e we adopt, as in the models before, Neumann boundary conditions

$$\frac{\partial c_{NH3}(x,y)}{\partial x} = 0 \text{ on } C_b \text{ and } C_f \ . \tag{7.30}$$

7.7.1 Simulation Results

This section presents the simulation results of Model 5. The section consists of six subsections. In the first subsection the dedoping coefficient k_2 for protonated pentacene is varied and the resulting changes are presented. Then the effects of different ammonia diffusion constants D_{NH3} in pentacene are investigated. In the subsection three the effects of different H^+ ion mobilities are studied. Afterwards, the recombination coefficient k_5 for H^+ ions in the SAM is varied in the fourth subsection. In the fifth subsection the effect of different ammonium concentrations c_{NH3} in the air are tested. In the last subsection the simulation results are compared with the results of the measurements. All the general parameters for the model 5 are listed in Tab. 7.3.

7.7.1.1 Variation of the Dedoping Coefficient k_2 for Protonated Pentacene in a NH_3 Environment

If a device with a SAM, that has already caused a threshold shift, is exposed to ammonia, the space charge layer disapears within seconds. From this information, the dedoping coefficient k_2 can be estimated. Fig. 7.37 shows how the amount of stored charge Q in pentacene is melting due to ammonia. The simulation is based on the input parameters in Tab. 7.3, and Tab. 7.16. For a dedoping coefficient k_2 smaller than 10^{-22} the temporal

evolution of the charge decay is no longer changing, because the speed of the charge decay is then limited by other process parameters, such as the H^+ ion mobility μ_I. With a dedoping coefficient k_2 close to 10^{-24} the charge decay in pentacene would be just inside the period of time based on the measurements.

Tabelle 7.16: Parameters for the simulation "Variation of the generation coefficient k_1"

Parameter	Value
μ_I / $m^2V^{-1}s^{-1}$	$1 \cdot 10^{-7}$
C_{SAG} / m^{-3}	$4 \cdot 10^{26}$
μ_h / $m^2V^{-1}s^{-1}$	$1 \cdot 10^{-9}$
$C_{DoPentaMax}$ / m^{-3}	$5 \cdot 10^{26}$
k_1 / m^3s^{-1}	$k_2 * 10^4$
k_2 / m^3s^{-1}	$1 \cdot 10^{-20} \ldots 1 \cdot 10^{-25}$
k_3 / s^{-1}	$1 \cdot 10^{-7}$
k_4 / s^{-1}	$1 \cdot 10^{-10}$
k_5 / m^6s^{-1}	$1 \cdot 10^{-42}$
D_{NH3} / m^2s^{-1}	$2.5 \cdot 10^{-10}$
$C_{NH3-Init}$ / m^{-3}	$1 \cdot 10^{22}$

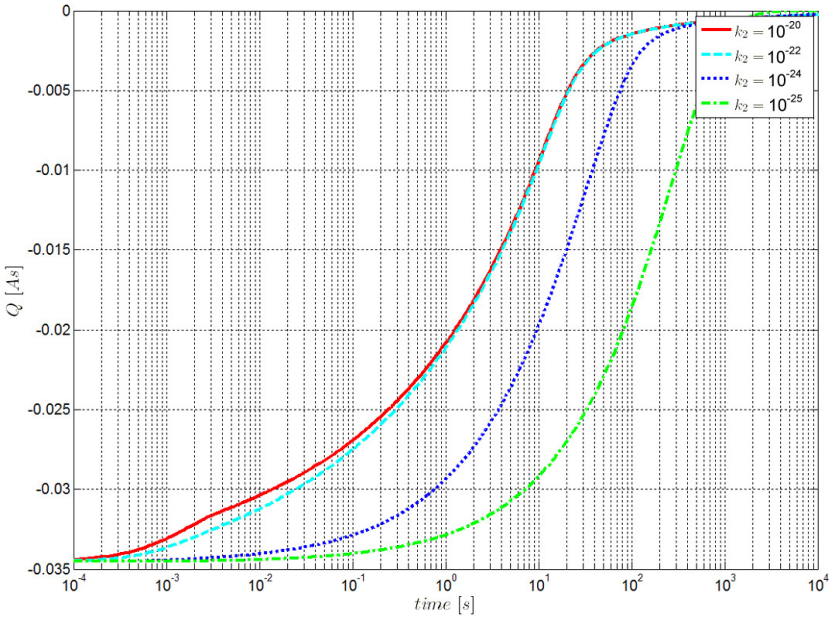

Fig. 7.37: Temporal formation of the ionic charge amount Q in pentacene for different dedoping coefficient k_2 with model 5.

7.7.1.2 Variation of the Ammonia Diffusion Coefficient

Due to different grain sizes of pentacene, the ammonia diffusion coefficient of the device may diver form device to device. For this reason, simulations are performed with different ammonia diffusion coefficients D_{NH3} to study these effects. The simulation based on the input parameters in Tab. 7.3, and Tab. 7.17. As shown in Fig. 7.38 the diffusion coefficient of ammonia has almost no effect on the charge reduction of H^+ ions in pentacene. Even with an unrealistically low diffusion coefficients the space charge layer would be removed within seconds.

Tabelle 7.17: Parameters for the simulation "Variation of ammonia mobility"

Parameter	Value
μ_I / $m^2V^{-1}s^{-1}$	$1 \cdot 10^{-7}$
C_{SAG} / m^{-3}	$4 \cdot 10^{26}$
μ_h / $m^2V^{-1}s^{-1}$	$1 \cdot 10^{-9}$
$C_{DoPentaMax}$ / m^{-3}	$5 \cdot 10^{26}$
k_1 / m^3s^{-1}	$1 \cdot 10^{-18}$
k_2 / m^3s^{-1}	$1 \cdot 10^{-22}$
k_3 / s^{-1}	$1 \cdot 10^{-7}$
k_4 / s^{-1}	$1 \cdot 10^{-10}$
k_5 / m^6s^{-1}	$1 \cdot 10^{-42}$
D_{NH3} / m^2s^{-1}	$2.5 \cdot 10^{-8} \ldots 2.5 \cdot 10^{-14}$
$C_{NH3-Init}$ / m^{-3}	$1 \cdot 10^{22}$

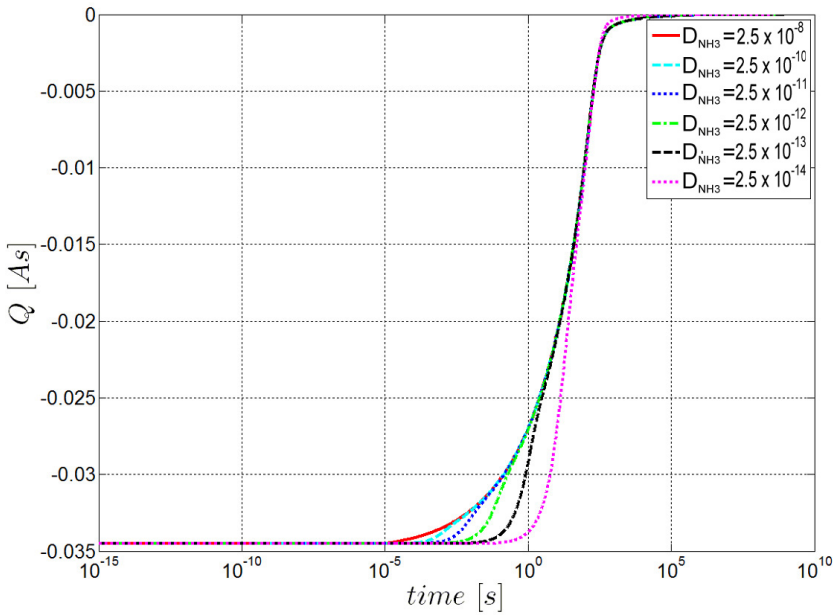

Fig. 7.38: Temporal formation of the ionic charge amount Q in pentacene for different NH_3 diffusion coefficients D_{NH3} with model 5.

7.7.1.3 Variation of H^+ Ion Mobility

The H^+ ion mobility in pentacene is varied to examine the impact on the charge reduction in pentacene. The simulation is based on the input parameters in Tab. 7.3, and Tab. 7.18. Fig. 7.39 shows the great impact of the H^+ ion mobility μ_I in pentacene on the H^+ ion charge reduction. The simulation of the H^+ ion charge reduction in combination with the measurements of the devices expose to NH_3 permits an H^+ ion mobility $\mu_I > 10^{-8}$ $m^2V^{-1}s^{-1}$ as can bee seen in Fig. 7.39. A smaller mobility would slow down the ionic charge reduction too much.

Tabelle 7.18: Parameters for the simulation "Variation of H^+ ion mobility"

Parameter	Value
μ_I / $m^2V^{-1}s^{-1}$	$1 \cdot 10^{-6} \ldots 1 \cdot 10^{-10}$
C_{SAG} / m^{-3}	$4 \cdot 10^{26}$
μ_h / $m^2V^{-1}s^{-1}$	$1 \cdot 10^{-9}$
$C_{DoPentaMax}$ / m^{-3}	$5 \cdot 10^{26}$
k_1 / m^3s^{-1}	$1 \cdot 10^{-18}$
k_2 / m^3s^{-1}	$1 \cdot 10^{-22}$
k_3 / s^{-1}	$1 \cdot 10^{-7}$
k_4 / s^{-1}	$1 \cdot 10^{-10}$
k_5 / m^6s^{-1}	$1 \cdot 10^{-42}$
D_{NH3} / m^2s^{-1}	$2.5 \cdot 10^{-10}$
$C_{NH3-Init}$ / m^{-3}	$1 \cdot 10^{22}$

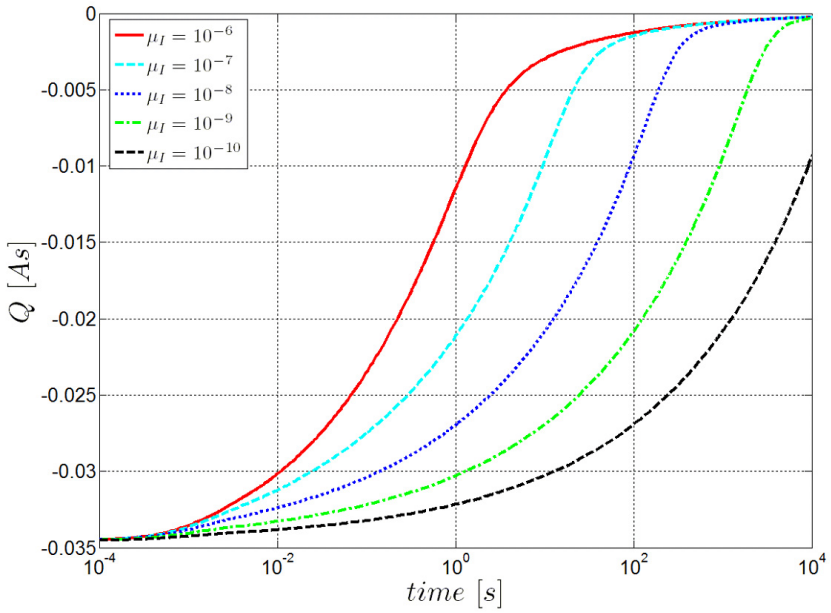

Fig. 7.39: Temporal formation of the ionic charge amount Q in pentacene for different H^+ ion mobilities with model 5.

7.7.1.4 Variation of the Recombination Coefficient k_5 for NH_3 in the SAM

Since the recombination coefficient k_5 for NH_3 in the SAM is not precisely determined, it is varied to study the impact on the time behavior of the threshold voltage shift. As can bee seen from Fig. 7.40, the variation of the recombination coefficient k_5, has an effect only in the final stage of the H^+ ion charge decay. A recombination coefficient k_5 larger than 10^{-43} m^6s^{-1} does no more evolution the ionic charge decay. Due to this the influence of the recombination coefficient k_5, should not be a time-limiting factor. To say more about the recombination coefficient k_5, additional measurements are needed.

Tabelle 7.19: Parameters for the simulation "Variation of H^+ ion mobility"

Parameter	Value
μ_I / $m^2V^{-1}s^{-1}$	$1 \cdot 10^{-8}$
C_{SAG} / m^{-3}	$4 \cdot 10^{26}$
μ_h / $m^2V^{-1}s^{-1}$	$1 \cdot 10^{-9}$
$C_{DoPentaMax}$ / m^{-3}	$5 \cdot 10^{26}$
k_1 / m^3s^{-1}	$1 \cdot 10^{-18}$
k_2 / m^3s^{-1}	$1 \cdot 10^{-22}$
k_3 / s^{-1}	$1 \cdot 10^{-7}$
k_4 / s^{-1}	$1 \cdot 10^{-10}$
k_5 / m^6s^{-1}	$1 \cdot 10^{-42} \ldots 1 \cdot 10^{-45}$
D_{NH3} / m^2s^{-1}	$2.5 \cdot 10^{-10}$
$C_{NH3-Init}$ / m^{-3}	$1 \cdot 10^{22}$

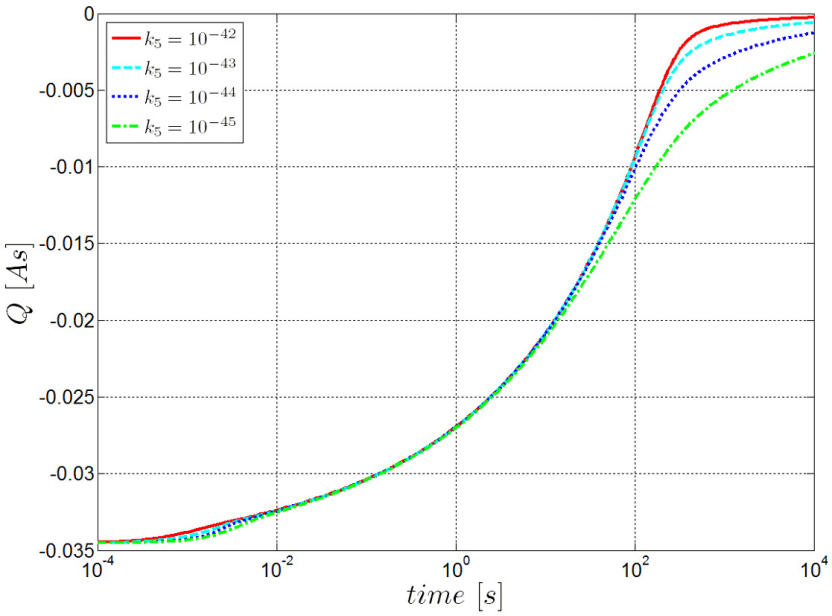

Fig. 7.40: Temporal formation of the ionic charge amount Q in pentacene for different ion recombination coefficients k_5 with model 5.

7.7.1.5 Variation of Ammonia Concentration in the Air

As the device was exposed to ammonia the concentration was not precisely determined. In this simulation the concentration of the ammonia is varied to find out if the device is sensitive to changes in the concentration of $NH3$. As can bee seen in Fig. 7.41 an concentration of NH_3 greater than 10^{20} does not lead to any significant changes in the time behavior below 100 seconds of the charge decay of H^+ ions. Only at an NH_3 density in the range of $c_{NH3-Init} = 10^{19}$ m^{-3} the charge reduction would run noticeably slower.

Tabelle 7.20: Parameters for the simulation "Variation of ammonia concentration"

Parameter	Value
μ_I / $m^2V^{-1}s^{-1}$	$1 \cdot 10^{-8}$
C_{SAG} / m^{-3}	$4 \cdot 10^{26}$
μ_h / $m^2V^{-1}s^{-1}$	$1 \cdot 10^{-9}$
$C_{DoPentaMax}$ / m^{-3}	$5 \cdot 10^{26}$
k_1 / m^3s^{-1}	$1 \cdot 10^{-18}$
k_2 / m^3s^{-1}	$1 \cdot 10^{-22}$
k_3 / s^{-1}	$1 \cdot 10^{-7}$
k_4 / s^{-1}	$1 \cdot 10^{-10}$
k_5 / m^6s^{-1}	$1 \cdot 10^{-42}$
D_{NH3} / m^2s^{-1}	$2.5 \cdot 10^{-10}$
$C_{NH3-Init}$ / m^{-3}	$1 \cdot 10^{-20} \ldots 1 \cdot 10^{-23}$

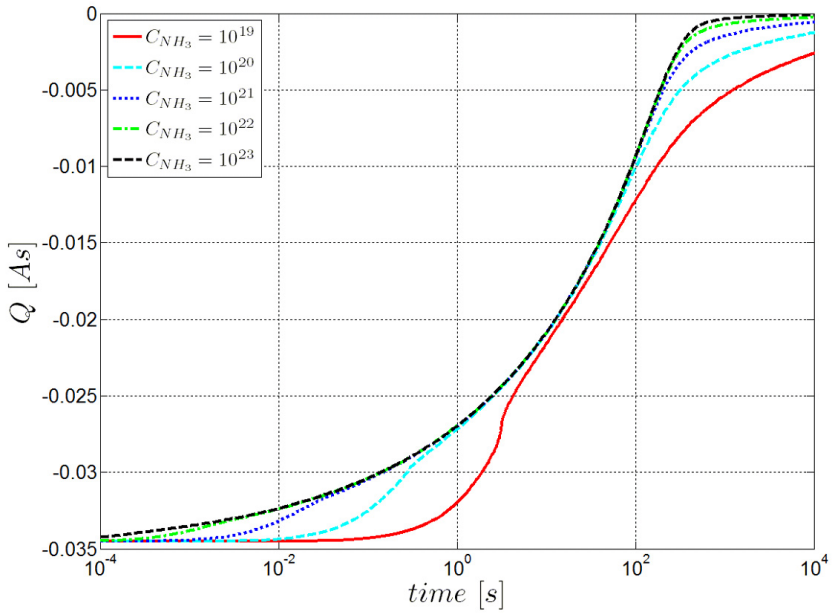

Fig. 7.41: Temporal formation of the ionic charge amount Q in pentacene for different ammonia concentration in the air with model 5.

7.7.1.6 Evaluation of the Model

All measurements can in principle be reproduced through this simulation. With the existing measurements, it is unfortunately, not possible to determine all the parameters of the simulation exactly, since different combinations of parameters are able to reproduce the measured values. The simulation results from Sec. 7.7.1.4 and Sec. 7.7.1.5, however, suggest that the devices respond even to very small amounts of ammonia. Additional measurements with different ammonia concentrations would be very interesting.

8 Conclusion

This thesis gives a brief overview of the derivation of the Boltzmann equation. Subsequently a detailed derivation of the carrier continuity equation and the drift-diffusion current equation from the Boltzmann equation is given. The Poisson equation is derived from the Gauss' and Faraday's law. Also a short overview of handling sources and sinks in drift-diffusion equations is presented. As a method to solve the resulting differential equations, the method of finite elements is presented. A detailed presentation of the resulting algebraic equations is derived.

In the second part of my thesis, I studied how a SAM made of 4-(2-(trichlorosilyl) ethyl) benzene-1-sulfonyl chloride (T-SC, 70 %) and a sulfonic acid derivate 4-(2-(trichlorosilyl)ethyl)benzenesulfonic acid (T-SA, 30 %) influences the threshold voltage of an organic thin film transistor. As active layer in the OTFT pentacene is used. Based on measurements it is assumed that such a SAM release H^+ ions into the active layer. The applied drift-diffusion model, which describes the transport of holes and the motion of H^+ ions, is solved self-consistently with the Poisson equation. In addition, rate equations are included to model chemical conversation processes. With this model it was possible to show that the H^+ ions are neutralized in the pentacene. Because of this neutralization a space charge is formed in the SAM, which cause a threshold voltage shift. Moroeover, the simulation shows that the neutralization process takes place on a time scale less than a second. As a result, the long duration of time, to reach the steady state, is based on the chemical separation process of H^+ ions in the SAM. Furthermore, simulations which an additional diffusion and rate equation for NH_3 molecules were made. Measurements have shown that an OTFT with such a SAM is responsive to the NH_3 gas. By means of simulations it was possible to show that the neutralization process of ions is reversible. In this way it was demonstrated that an OTFT with such a SAM is very sensitive to small quantities of NH_3 molecules in the air.

Bibliography

[1] M.A. Alam, A. Dodabalapur, M.R. Pinto: *A two-dimensional simulation of organic transistors.* IEEE Trans. Electron Devices, Vol. 44, No. 8, pp. 1332-1337, 1997.

[2] W. Wondmagegn, R. Pieper: *Simulation of top-contact pentacene thin film transistor.* J. Comput. Electron., Vol. 8, No. 1, pp. 19-24, 2009.

[3] L. Demeyu, S. Stafström, M. Bekele: *Monte Carlo simulation of controlled charge carriers diffusion in highly ordered iodine doped pentacene film.* Phys. Status Solidi A, Vol. 204, No. 10, pp. 3545-3555, 2007.

[4] H. Qiu, B. Wilke, H. Gobel: *Device simulation of pentacene based organic field-effect transistors.* Portable Information Devices, pp. 1-4, 2008.

[5] R. Cantrell, P. Clancy: *A computational study of surface diffusion of C60 on pentacene.* Surf. Sci., Vol. 602, No. 22, pp. 3499-3505, 2008.

[6] Y. Li: *A two-dimensional thin-film transistor simulation using adaptive computing technique.* Appl. Math. Comput., Vol. 184, No. 1, pp. 73-85, 2006.

[7] C. Ucurum, H. Siemund, H. Göbel: *Impact of electrical measurement parameters on the hysteresis behavior of pentacene-based organic thin-film transistors.* Org. Electron., Vol. 11, No. 9, pp. 1523-1528, 2010.

[8] D. Gupta, N. Jeon, S. Yoo: *Modeling the electrical characteristics of TIPS-pentacene thin-film transistors: Effect of contact barrier, field-dependent mobility, and traps.* Org. Electron., Vol. 9, No. 6, pp. 1026-1031, 2008.

[9] D. Gupta, Y. Hongb: *Understanding the effect of semiconductor thickness on device characteristics in organic thin film transistors by way of two-dimensional simulations.* Org. Electron., Vol. 11, No. 1, pp. 127-136, 2010.

[10] O.D. Jurchescu, J. Baas, T.T.M. Palstra : *Effect of impurities on the mobility of single crystal pentacene.* Appl. Phys. Lett., Vol. 84, No. 16, pp. 3061, 2004.

[11] M. Lundstrom: *Fundamentals of Carrier Transport.* Cambridge University Press, Cambridge, 2000.

[12] A. Jüngel: *Transport Equations for Semiconductors.* Springer-Verlag, Berlin, 2009.

[13] C. Weissmantel, C. Hamann: *Grundlagen der Festkörperphysik.* Springer-Verlag, Berlin, 1979.

[14] D. Schroeder: *Vektor- und Tensorpraxis.* Harri Deutsch Verlag, Frankfurt, 2009.

[15] P.A. Markowich, C.A. Ringhofer, C. Schmeiser: *Semiconductor Equations.* Springer-Verlag, New York, 1990.

[16] M. Trautz: *Das Gesetz der Reaktionsgeschwindigkeit und der Gleichgewichte in Gasen. Bestätigung der Additivität von Cv-3/2R. Neue Bestimmung der Integrationskonstanten und der Moleküldurchmesser.* Z. anorg. allg. Chem., Vol 96, No. 1, pp. 1-28, 1916.

[17] K.A. Connors: *Chemical Kinetics, the Study of Reaction Rates in Solution.* VCH Publishers, New York, 1991.

[18] C. Kittel: *Einführung in die Festkörperphysik.* Oldenbourg Wissenschaftsverlag, München, 2005.

[19] H.R. Schwarz: *Methode der Finiten Elemente.* Teubner, Stuttgart, 1991.

[20] M. Jung, U. Langer: *Methode der Finiten Elemente für Ingenieure.* Teubner Verlag, Stuttgart, 2001.

[21] R. Plato: *Numerische Mathematik kompakt: Grundlagenwissen für Studium und Praxis.* Vieweg, Wiesbaden, 2004.

[22] H. Lakshmininarayana: *Finite Elements Analysis: Procedures in Engineering.* Universities Press, Hyderabad, 2004.

[23] V.I. Krylov: *Approximate Calculation of Integrals.* MacMillan, New York, 1962.

[24] K.J. Bathe: *Finite-Elemente-Methoden.* Springer-Verlag, Berlin, 2007.

[25] A.H. Stroud: *Approximate Calculation of Multiple Integrals.* Prentice-Hall, Englewood Cliffs, 1971.

[26] A.H. Stroud, D. Secrest : *Gaussian Quadrature Formulas.* Prentice-Hall, Englewood Cliffs, 1966.

[27] M. Abramowitz, I.A. Stegun: *Handbook of Mathematical Functions.* Dover Pubn Inc, Dover, 1970.

[28] J. Argyris, H.P. Mlejnek: *Die Methode der Finiten Elemente.* Bd 1-3, Friedr. Vieweg und Sohn, Braunschweig, 1988.

[29] E. Stiefel: *Einführung in die numerische Mathematik.* 5. Aufl., Teubner, Stuttgart, 1976.

[30] M. R. Hestenes, E. Stiefel: *Methods of Conjugate Gradients for Solving Linear Systems.* J. Res. Nat. Bur. Stand., Vol. 49, No. 6, pp. 409-436, 1952.

[31] M. Ohtomo, T. Shimada, K. Saiki T. Hasegawa: *Metal-induced Urbach tail at the gold-pentacene interface of top-contact organic field effect transistors.* J. Appl. Phys., Vol. 102, No. 6, pp. 064510, 2007.

[32] D. Gupta, N. Jeon, S. Yoo: *Modeling the electrical characteristics of TIPS-pentacene thin-film transistors.* Org. Electron., Vol. 9, No. 6, pp. 1026-1031, 2008.

[33] H. Li, Y. Duan, V. Coropceanu J.L. Bredas: *Electronic structure of the pentacene-gold interface: A density-functional theory study.* Org. Electron., Vol. 10, No. 8, pp. 1571-1578, 2009.

[34] F. Amy, C. Chan, A. Kahn: *Polarization at the gold/pentacene interface.* Org. Electron., Vol. 6, No. 2, pp. 85-91, 2005.

[35] Y. Hong, F. Yan, P. Migliorato, S.H. Han, J. Jang: *Injection-limited contact in bottom-contact pentacene organic thin-film transistors.* Thin Solid Films, Vol. 515, No. 7-8, pp. 4032-4035, 2007.

[36] I. Kyuwook, K. Bongsoo, K.T. Hee K.K. Jeong J.M. Ho K.T. Hyeong Y.S. Soo C. Sukmin: *Molecular orientation dependence of hole-injection barrier in pentacene.* Appl. Phys. Lett., Vol. 89, No. 3, pp. 33504-33504-3, 2006.

[37] K. Hong, J.W. Lee, S.Y. Yang K. Shin H. Jeon S.H. Kim C. Yang C.E. Park: *Lower hole-injection barrier between pentacene and a 1-hexadecanethiol-modified gold substrate with a lowered work function.* Org. Electron., Vol. 9, No. 1, pp. 21-29, 2008.

[38] M.D.N. Bussac, L. Zuppiroli, A. Mühlenen,F. Nüesch, M. Schaer,M. Brinkmann, M.N. Bussac: *Ultrathin organic transistors on oxide surfaces.* New J. Phys., Vol. 7, 133, 2005.

[39] S. J. Ausserlechner: *private communications.* TU Graz Institute of Solid State Physics.

[40] P. Lancaster, K. Salkauskas: *Curve and Surface Fitting An Introduction.* Academic Press, London, 1986.

[41] P. Pacher, A. Lex, V. Proschek, H. Etschmaier, E. Tchernychova, M. Sezen, U. Scherf, W. Grogger, G. Trimmel, C. Slugovc, E. Zojer: *Chemical Control of Local Doping in Organic Thin-Film Transistors: From Depletion to Enhancement.* Adv. Mater., Vol. 20, No. 16, pp. 3143-3148, 2008.

[42] G. Gu, M.G. Kane, J.E. Doty, A.H. Firester: *Electron traps and hysteresis in pentacene-based organic thin-film transistors.* Appl. Phys. Lett., Vol. 87, No. 24, pp. 243512(1-3), 2005.

[43] S. J. Ausserlechner,M. Gruber,R. Hetzel,H.-G. Flesch,L. Ladinig,L. Hauser,A Haase,M. Buchner,R. Resel,F. Schürrer,B. Stadlober,G. Trimmel,K. Zojer,E. Zojer: *Mechanism of surface proton transfer doping in pentacene based organic thin-film transistors.*